Connectomics across development: towards mapping brain structure from birth to childhood

THÈSE N^{O} 6754 (2015)

PRÉSENTÉE LE 9 OCTOBRE 2015
À LA FACULTÉ DES SCIENCES ET TECHNIQUES DE L'INGÉNIEUR
LABORATOIRE DE TRAITEMENT DES SIGNAUX 5
PROGRAMME DOCTORAL EN GÉNIE ÉLECTRIQUE

ÉCOLE POLYTECHNIQUE FÉDÉRALE DE LAUSANNE

POUR L'OBTENTION DU GRADE DE DOCTEUR ÈS SCIENCES

PAR

Elda FISCHI GOMEZ

acceptée sur proposition du jury:

Dr J.-M. Vesin, président du jury
Prof. J.-Ph. Thiran, directeur de thèse
Prof. P. Hüppi, rapporteuse
Prof. L. Zöllei, rapporteuse
Prof. D. Van De Ville, rapporteur

ÉCOLE POLYTECHNIQUE
FÉDÉRALE DE LAUSANNE

Suisse
2015

“Si el mundo se te ha quedado pequeño,
abre tus alas, y echa a volar.”

Abstract

The brain is probably the most complex system of the human body, composed of numerous neural units interconnected at different scales. This highly structured architecture provides the ability to communicate, synthesize information and perform the analytical tasks of human beings. Its development starts during the transition between the embryonic and fetal periods, from a simple tubular to a highly complex folded structure. It is globally organized as early as birth.

This developing process is highly vulnerable to antenatal adverse conditions. Indeed, extreme prematurity and intra uterine growth restriction are major risk factors for long-term morbidities, including developmental ailments such as cerebral palsy, mental retardation and a wide spectrum of learning disabilities and behavior disorders. In this context, the characterization of the brain's normative wiring pattern is crucial for our understanding of its architecture and workings, as the origin of many neurological and neurobehavioral disorders is found in early structural brain development.

Diffusion magnetic resonance imaging (dMRI) allows the *in vivo* assessment of biological tissues at the microstructural level. It has emerged as a powerful tool to study brain connectivity and analyse the underlying substrate of the human brain, comprising its structurally integrated and functionally specialized architecture. dMRI has been widely used in adult studies. Nevertheless, due to technical constraints, this mapping at earlier stages of development has not yet been accomplished. Yet, this time period is of extreme importance to comprehend the structural and functional integrity of the brain. This thesis is motivated by this shortfall, and intends to fill the gap between the clinical and neuroscience demands and the methodological developments needed to fulfill them.

In our work, we comprehensibly study the brain structural connectivity of children born extremely prematurely and/or with additional prenatal restriction at school-age. We provide evidence that brain systems that mature early in development are the most vulnerable to antenatal insults. Interestingly, the alterations highlighted in these systems correlate with the neurobehavioral and cognitive impairments seen in these children at school-age. The overall brain organization appear also altered after preterm birth and prenatal restriction. Indeed, these children show different brain network modular topology, with a reduction in the overall network capacity.

What remains unclear is whether the alterations seen at school age are already present at birth and, if yes, to what extent. In this thesis we set the technical basis to enable the connectome analysis as early as at birth. This task is challenging when dealing with neonatal data. Indeed, most of the assumptions used in adult data processing methods do not hold, due to the inverted image contrast and other MRI artefacts such as motion, partial volume and intensity inhomogeneities. Here, we propose a novel technique for surface reconstruction, and provide a fully-automatic procedure to delineate the newborn cortical surface, opening the way to establish the newborn connectome.

Keyworkds: *diffusion MRI, brain connectivity, connectome, graph theory, extreme prematurity, intra uterine growth restriction, growth connectomics, newborn cortical parcellation, surface reconstruction, surface restoration, spherical surface registration*

Résumé

Le cerveau est probablement le système le plus complexe du corps humain, composé de multiples unités neuronales interconnectées à différentes échelles. Cette architecture hautement structurée fournit la capacité de communiquer, de synthétiser des informations et d'effectuer des tâches d'analyse typiques des êtres humains. Son développement commence au cours de la transition entre les périodes embryonnaires et fœtales. Il se développe à partir d'une simple structure tubulaire jusqu'à devenire une structure repliée extrêmement complexe. Il est globalement organisé dès la naissance.

Pourtant, ce processus de développement est très vulnérable aux conditions prénatales défavorables. En effet , la grande prématurité et la restriction de croissance intra utérine sont les principaux facteurs de risque de morbidité à long terme, y compris les problèmes de développement tels que la paralysie cérébrale, le retard mental et un large éventail de troubles d'apprentissage et de comportement. Dans ce contexte, la caractérisation du schéma de câblage du cerveau est essentielle pour notre compréhension de son architecture et de son fonctionnement, étant donné que l'origine de nombreux troubles neurologiques et neuro-comportementaux se trouve dans les premiere etapes du développement du cerveau.

L'IRM de diffusion permet l'examen *in vivo* des tissus biologiques au niveau de la microstructure. Depuis quelques années, cette technique a émergé comme un outil puissant pour étudier la mise en place de la connectivité du cerveau et pour analyser le substrat sous-jacent du cerveau humain, incluant une architecture structurellement intégrée et fonctionnellement spécialisée. L' IRM de diffusion a été largement utilisée dans les études à l'âge adulte. Néanmoins, en raison des contraintes techniques, à des stades précoces de développement cette analyse n'est pas possible. Cependant, cette période est d'extrême importance pour comprendre l'intégrité structurelle et fonctionnelle du cerveau. Cette thèse est motivée par ce manque, et vise à combler le fossé existant entre les besoins cliniques et de la neuroscience et les développements méthodologiques nécessaires pour les remplir.

Premièrement, nous avons étudié la connectivité structurelle à l'âge scolaire des enfants nés extrême prématurés et/ou avec de la restriction de croissance prénatale. Nous apportons la preuve que les systèmes du cerveau qui mûrissent tôt dans le développement sont les plus vulnérables aux défaillances prénatales. Fait intéressant, les modifications au niveau de la connectivité mises en évidence par notre analyse dans ces systèmes sont en corrélation avec le comportement neurologique et les troubles cognitifs observés dans chez ces enfants à l'âge scolaire. L'organisation globale du cerveau est également modifiée après une naissance prématurée ou avec de la restriction de croissance. En effet, ces enfants montrent aussi des différences de topologie modulaire de leur réseau cérébral, avec une réduction de la capacité globale.

Il reste à déterminer si ces altérations observées à l'âge scolaire sont déjà présentes à la naissance. En d'autres termes, il serait intéressant de savoir si le cerveau est capable de venir à bout de ces limitations pendant son développement. Pour répondre à cette question, dans cette thèse nous avons développé des outils permettant la construction du connectome dès la naissance. Néamoins, cette procédure est difficile lorsqu'il s'agit de travailler sur des données néonatales.

En effet, la plupart des hypothèses utilisées sur les méthodes appliquées chez l'adulte ne sont pas applicables, en raison de la différence de contraste de l'image et d'autres artefacts propres à l'acquisition IRM tels que le mouvement, le volume partiel et les inhomogénéités d'intensité. Ici, nous proposons une nouvelle technique pour la restauration et la reconstruction des surfaces corticales. De plus, nous développons une procédure entièrement automatique pour délimiter des régions d'intêret sur cette même surface, ce qui permettra, à terme, la construction du connectome chez le nouveau-né.

Mots clefs : *IRM de diffusion, connectivité cérébrale, connectome, théorie des graphes, extrême prématurité, retard de croissance intra-utérin, connectome du nouveau-né, parcellisation corticale chez le nouveau-né, restauration de surfaces, recalage de surfaces sphériques.*

Acknowledgements

The acknowledgement section: the most difficult section to write but, with no doubt, the most soul-stirring. This thesis marks the end of 5 years of an intense period of learning and work, whose completion would have not been possible without the help, supervision, guidance and friendship of many great people around me.

First and foremost, I would like to thank my supervisor, Prof. Jean-Philippe Thiran, for giving me the possibility of working at the LTS5, and for make me feel part of one of the best scientific environments I would ever met. Jean-Philippe, thank you for your unconditional support during these 5 years of PhD and all my years at the EPFL. Thank you for your advices, your positiveness and your ability to make me see thinks under a different perspective, which helped me to keep on trying even when the results were not as good as I expected. I am sure that my work would have never been possible without it. My warmest thanks to Prof. Petra Hüppi, for creating such an interdisciplinary network, for your passion, for the helpful discussions and more importantly, for always trying to bridge the gap between complementary fields of research. Thank you for your trust, for your guidance in the neurosicence field (that I did not know much at the beginning) and for always pushing me toward new research questions and interesting new ideas. And above all, thanks to both of you for your comprehension and essential help in the crucial moments of my PhD, specially with the birth of Cléo. Your unfailing support, care and insights helped me through the hardest times of research and decision making. I'm concious and very grateful for all the opportunities you both offered me.

With respect to my dissertation work, I would like to thank the members of my jury who read through my manuscript and leaded a fruitful discussion during my PhD exam. Thanks all of you for your time, your insightful questions and comments.

I would like to acknowledge all the exchange of ideas and interactions with collaborators, fundamental to complete this work. I owe a tremendous amount of gratitude to Dr. Virginia Estellers for her inputs and constructive comments. Her research expertise and enthusiasm greatly helped me, and our joint projects enhance my knowledge about numerous theoretical topics. I would also like to sincerely thank all the scientists, doctors, technicians and students of the Geneva pole of the Centre d'Imagèrie Biomédicale (CIBM) with whom I had the chance to collaborate and discuss. I have learnt a lot of these discussions!. In particular many thanks to Prof. François Lazeyras, Dr. Nicolas Kunz, Dr. Laura Gui, Dr. Jean-Nöel Hyacinthe, Dr. Bénédicte Delattre and Dr. Lindsey Crowe.

A sincere thanks goes to the people of the Departement de Développement et Croissance at the Geneva University Hospitals (HUG), with whom I profitably collaborate from the beginning of my PhD. A special thanks goes to Dr. Lana Vasung. During all these years you fed my curiosity for neuroscience and developmental neuroanatomy and you generously share your knowledge with me... Thanks! My gratitude goes also to Cristina, Alexandra, Lara, Frédéric and all the people from the "Lausanne side", all the doctors and scientists from the Neonatology Department at the the Centre Hospitalier Universitaire Vaudois (CHUV).

I owe a tremendous amount of gratitude to the unofficial thesis readers: Yann Prudat, Alessandra Griffa, Meri Bach, Leila Mirmohamadsadeghi, Guillaume Bonnier. Given all the time pressure that I had before finishing my dissertation, their input and constructive comments were invaluable when I was finishing.

Besides working on the final document, I got a great amount of support of my friends and colleagues form the LTS5 and all SP labs. Undoubtedly, my warmest thanks go to the past and present members of the LTS5, LTS2, LTS4, ASPG and MMSPG labs, who made the everyday life in Lausanne so much more fun. I would first like to thank my office mates, Alessandra and Meri, for the time we spent together in a quite tiny but super-nice office, that we manage to fill up with plants and still have place for us. Thanks for the laughs, gossips, coffee breaks and your unconditional support in the good, but specially in the bad moments. I definitely know that I would have not been able to do that without you, my girls. Three other office-mate deserves to be added here: Andrea Buttu, Alia Lemkaddem and Leila Mirmohamadsadeghi . Thank your Andrea, you have always been there to share a laugh, a beer and whatever I need. Thank you Alia, for all the years we have spent together, for everything. And Leila, thank for you sweetness and comprehension, for your endless smiles and optimism. A great hug goes to Anil, Martin, Eleni, Anna, Laura, the ASPG members, Sybille, Adrian and Sasan, and all the others in the lab, for all the cheerful breaks and for helping me in many senses. My sincere thanks also to the "old" members of this great family: Ashkan, Aline, Florian, Jerôme, Laurent, Benoit. Their humour, optimism and unconditional support have contributed to endless happy moments.A special thanks goes to Rosie, for her extremely good organization, administrative help and little moments around a coffee.

My life in Lausanne would have not been complete without the my little "family". In Lausanne, outside the small world of my office and my lab, I was extremely lucky to befriend a set of other great pals: Remi, Francesca, Cedric, Renata, Anna, Lluis, Mathieu, Delphine, AnneSy et Julian. Been far away from my family would have been tougher if you were not around. I am greatly delighted that I met many of you right after my arrival at the EPFL and I hope to be in touch with you all for very long time.

Yann, you come apart. I can say that you have been my greatest support for all these years. You were the first person I met when I came to the EPFL, and since then, you have always been there, for the good and the bad. We have shared incredible moments of joy and laugh but, most importantly, you have always been there when I needed. Thanks a million! I would not be the same person as I am now without you. Another person deserves my warmest appreciation for his unfailing car, love and support throughout my stay at the EPFL: merci Jean Marc, merci pour tout.

Thanks to my friends, all over the world. Specially Gemma, in Barcelona. Half of my degree is your fault. Thanks for being there always, with a glass of wine or with a handkerchief. Thanks for 'kicking my face' to make me keep going and for hug me when my strength was not enough. I've had used yours, so thanks for that.

Je voudrais aussi parler de Guillaume, qui j'ai rencontré il y a déjà quelques années a l'EPFL. Merci Guillaume, pout ton amour, pour toute la confiance et encouragement que j'ai reçu pendant toutes ces années et celles qui vont venir. Merci d'être là, merci d'être toi. Merci de me supporter (et tu sais bien que c'est parfois pas évident). Merci pour me comprendre et pour m'encourager a suivre mes rêves, et m'épauler dans mes choix et mes décisions. Et surtout pour notre petite merveille, Cléo.

And the warmest thanks to the rest of my family...big and nice. From so many miles away, their encouraging words never failed to reach me and their readiness to help and console were a rock-solid pillar throughout all these years. Thanks all of us and a special loving memory to the ones that are no longer there. Never forget.

Last, but unquestionable not least, I would like to acknowledge the eternal support and love that I received from my parents and my brother and sister. Mum and Dad, this is because of you. Thanks for everything, for living and for being there always, in every case and without conditions. Thanks for show me how to fight for my dreams. There are no words...nothing that I can say at this point could show exactly how much have you both done for me. Os quiero un mundo ... Oscar, thanks for being the big brother, in all senses. For having always a word of support...and also some regrets . You're right. You have always been right with your advices, even if I hadn't follow all of them (I should have done it more often). And thanks for my to nephews, Bruno and Arnau. I wish I had been closer to them these last years. Erika (nina, ya sabes). My sister, my love, my complement. No words. Useless. Thanks, thanks for being you and me at the same time. Thanks for tell me, when I was in the train coming here, "just enjoy, no panic...just live". Thanks, for the late calls at night, for the smiles, for the travel...for your "Elda come on"... And thanks Gabriel, for loving her and making her happy. And for making me always feel at home and for always having a smile in the face even if I know it is not easy to deal with a couple of twins. Esto es vuestro, por todo lo que me habéis dado todos estos años, y por lo que nos queda por vivir juntos.

My most sincere thanks to everyone, even the ones I've had forgotten when writing this. This work is also yours.

Elda

Contents

Abstract **v**

1 Preface **1**
1.1 Context 1
1.2 Motivations 3
1.3 Contributions of the thesis and organization of the manuscript 3
1.3.1 Main contributions of the thesis 3
1.3.2 Organization of the manuscript 4

I Part 1 **7**

Overview **9**

2 Structural connectivity in school-age preterm infants **13**
2.1 Context and background 13
2.2 Material and methods 13
2.2.1 Subjects 13
2.2.2 Connectivity estimation 14
2.2.3 Statistical analysis 16
2.3 Results 16
2.3.1 Global connectivity 16
2.3.2 Local connectivity changes in FA-weighted structural connectivity 17
2.3.2.1 Changes in FAw-SC after extreme prematurity (EP vs. Controls) 17
2.3.2.2 Changes in FAw-SC after IUGR (IUGR vs. Controls) 17
2.3.2.3 Differences in FAw-SC between EP and IUGR 17
2.3.2.4 Social and higher order cognitive evaluation 20
2.3.2.5 Correlation of altered FAw-SC with socio-cognitive scores . . 20
2.4 Discussion 21
2.4.1 Global connectivity analysis 21
2.4.2 Local Connectivity Analysis 24
2.4.2.1 Connections with weaker FAw-SC 24
2.4.2.2 Connections with stronger FAw-SC 26
2.4.3 Implications for understanding cognition and behavior 26
2.5 Limitations 27
2.6 Conclusions 27

3 Mapping brain topology at school age **29**
3.1 Context and background 29
3.2 Material and methods 30
3.2.1 Subjects 30
3.2.2 Neurodevelopmental assessment 31
3.2.3 Brain network construction 31
3.2.4 Network features 32
3.2.4.1 Organizational measures 32
3.2.4.2 Integration and segregation measures 33
3.2.5 Statistical analysis 34
3.3 Results 34
3.3.1 Cognitive group differences 34
3.3.2 Network features: group differences 34
3.3.2.1 Organizational measures 34
3.3.2.2 Integration and segregation measures 37
3.4 Discussion 40
3.5 Conclusions 43

II Part 2 **45**

Overview **47**

4 Surface reconstruction **51**
4.1 Introduction and background 51
4.1.1 Geometry of cortical manifolds 51
4.1.2 On curvature 52
4.1.3 Surface extraction and reconstruction 55
4.1.4 Surface smoothing 56
4.1.5 Curvature estimation 57
4.2 Context and motivations 59
4.2.1 Motivations 59
4.3 Material and Methods 60
4.3.1 Newborn data 60
4.3.2 Proposed scheme for cortical surface restoration 61
4.4 Results 69
4.4.1 Parameter choices 74
4.5 Potential improvement of the algorithm 76
4.6 Discussion and conclusions 76

5 Surface parcellation **79**
5.1 Context and Motivations 80
5.1.1 On Registration 81
5.1.2 Motivations 83
5.2 Material and Methods 84
5.2.1 MR brain data 84
5.2.2 Surface inflation, flatting and projection onto a sphere 84
5.2.3 Registration scheme 85
5.2.4 Classification 86
5.2.4.1 Building the cortical labels maps 86
5.2.4.2 Bayesian classification approach 88

5.2.4.3 MAP estimate 89
5.3 Results 89
5.4 Discussion and Conclusions 96

III Final conclusions 101

6 Discussion and Conclusions 103
6.1 Summary and contributions 103
6.2 Perspectives 105

Appendices 109

A Appendix A
Computing the connectivity matrix 111
A.1 Computing connectivity matrix 111
A.1.1 MRI acquisition 111
A.1.2 Building the connectivity matrix 111
A.2 Modeling SC 112

B Appendix B
Statistical analysis of connectomes 113
B.1 Statistical analysis 113
B.1.1 Global analysis of ADC-weighted and FA-weighted connectomes 113
B.1.2 Local analysis of FA-weighted connectomes. Pairwise FAw structural connectivity 113

C Appendix C
Extreme prematurity and intra-uterine growth restriction 115
C.1 Definitions 115
C.2 Causes, incidence and outcomes of extreme prematurity and IUGR. 116
C.2.1 Extreme prematurity 116
C.2.2 Intra-uterine growth restriction 116

D Appendix D
Cognitive assessment 119

E Appendix E
Modularity and consensus clustering 121
E.1 Estimation and comparison of clustering structures 121
E.1.1 Algorithms for community detection 121
E.1.2 Information theory metrics for clustering comparison 123

Bibliography 127

Curriculum Vitæ 141

Publications 143

List of Acronyms

χ	Euler characteristic of a surface
ρ	Radius ratio of a surface
g	surface genus
N_i	first ring neighbourhood
ADC	apparent diffusion coefficient
ADCw-SC	apparent diffusion coefficient weighted structural connectivity
AIC	akaike information criterion
APGAR	appearance, pulse, grimace, activity, and respiration
B	$B = H \cup K$ curvature
BIC	bayesian information criterion
BW	birth weight
CBTCL	cortico-basal ganglia-thalamo-cortical loop
CC	consensus clustering partition
CD	connection density
CE	connection efficacy
CSF	cerebro spinal fluid
CTRL	healthy subjects control group
dMRI	diffusion magnetic resonance imaging
DSI	diffusion spectrum imaging
DTI	diffusion tensor imaging
DWI	diffusion weighted imaging
EP	extreme prematurity
FA	fractional anisotropy
FAw-SC	fractional anisotropy weighted structural connectivity

FDR	false discovery rate
FS	FreeSurfer software
FWER	family wise error rate
GA	gestational age
gCD	group connection density
GLM	generalized linear model
GM	grey matter
H	gaussian curvature
HARDI	high angular resolution diffusion imaging
HD	Hausdorff distance
ICM	iterated conditional modes
IE	IUGR + EP subjects
IO	IUGR only subjects
IUGR	intrauterine growth restriction
IVH	intra ventricular haemorrhage
K	intrinsic curvature
K-ABC	Kaufmann assessment battery for children
M	surface mesh
MI	mutual information index
MIn	normalized mutual information index
MPRAGE	magnetization prepared rapid acquisition gradient echo
MR	magnetic resonance
MRI	magnetic resonance imaging
PCW	post conceptional weeks
PD	proton density
PVP	periventricular fiber pathways
Q	modularity index
ROI	region of interest
SC	structural connectivity
SDD	smooth signed distance surface reconstruction method
SDQ	strength and difficulties questionnaire

SES	socio-economic status
SRT	social resolution task
T1w	T1 weighted acquisition
T2w	T2 weighted acquisition
TA	acquisition time
TE	echo time
TEA	term equivalent age
TI	inversion time
TP	time point
TPM	transition probability matrix
TR	repetition time
U	$B = H \cap K$ curvature
VI	variation of information index
VIn	normalized variation of information index
WM	white matter
WRS	Wilcoxon rank-sum statistical test
WSR	Wilcoxon signed-rank statistical test

List of Tables

2.1 Sample characteristics of the study participants according to gestational age (GA) and presence of intrauterine growth restriction (IUGR) at 6 years old 15

3.1 Sample characteristics of the study participants according to gestational age (GA) and presence of intrauterine growth restriction (IUGR) 31
3.2 Neurocognitive scores 34
3.3 Number of modules and modularity index Q from subject-wise brain network modular decomposition 35
3.4 Intra-group MIn and VIn values for intra-group comparison 36
3.5 Inter-group MIn and VIn values for case-control comparison 36
3.6 Inter-group MIn and VIn values for case-case comparison 37
3.7 List of abbreviation for cortical and subcortical regions 39
3.8 Differences in network integration and segregation measures for case-control comparison 39
3.9 Differences in network integration and segregation measures for case-case comparison 40
3.10 In each column, predictors used in the linear regression 40

4.1 Topology information for the original and reconstructed meshes 70
4.2 Mesh elements quality metrics of the original and reconstructed meshes 70
4.3 Hausdorff Distance between the original and the reconstructed surface 74

5.1 Automated parcellation for the same subject for each of the parcellating scheme presented compared to the 6 years-old counterpart obtained using FS standard procedure 91
5.2 Same parcellation results as in table 5.1, presented on the the inflated surfaces . . 92
5.3 Automated parcellation for the worst case subject (subject #3) for the pairwise parcellating scheme presented compared to the 6 year-old's counterpart obtained using the FS standard procedure 94

A.1 Scanning parameters 111

D.1 Cognitive sample characteristics of the study participants according to gestational age (GA) and presence of intrauterine growth restriction (IUGR) at 6 years old 120
D.2 Linear regression model testing the effects of gestational age (GA) and intra uterine growth restriction (IUGR) on children's performance in cognitive workload tasks 120

List of Figures

1.1 Schematic timetable of the development of axonal pathways in the human brain . 11

2.1 Connections altered in EP children at school age 18
2.2 Pearson's correlation strength between FAw-SC of altered connections and socio cognitive outcome for EP children 18
2.3 Connections altered in IUGR children at school age 19
2.4 Pearson's correlation strength between FAw-SC of altered connections and socio cognitive outcome for EP children 19
2.5 Altered connections between IUGR and EP children at school age 20
2.6 Schematic drawing of altered connections in EP subjects whose FAw-SC strength correlates with socio-cognitive outcome 22
2.7 Schematic drawing of altered connections in IUGR subjects whose FAw-SC strength correlates with socio-cognitive outcome. 23

3.1 Normalized MI and VI indices between each pair of subject's optimal modular decompositions 36
3.2 Group CC representative partitions 38
3.3 Main processing steps to delineate cortical structures 48

4.1 Gyrification process 52
4.2 MRI scan for the same extreme premature subject at two different time points: birth and term equivalent age 53
4.3 Three-dimensional reconstruction of the basal ganglia and ganglionic eminence, ventricle and whole brain of a fetus from 13 weeks post-gestational age to 21 weeks 53
4.4 Main processing steps to restore and reconstruct the cortical surfaces 60
4.5 Coronal view of the detection of cortical an subcortical gray matter, myelinated and unmyelinated white matter and CSF for a for one of our four subjects' MR scan 61
4.6 Intersection of tessellated WM (green line) and GM (yellow line) surfaces with the MRI volume for newborn data 62
4.7 Original tesselated surface 64
4.8 Same surface after 10 iteration of the Taubin smoothing 64
4.9 Sharp peak located in the central part of the right cortical surface 65
4.10 Sharp peak located in the central part of the right cortical surface with its corresponding face normals 65
4.11 Sharp peak located in the central part of the right cortical surface with curvature information 66
4.12 Best original cortical surface 71
4.13 Final reconstructed surface 71
4.14 Zoom to peak 72

4.15 Zoom to a peak before and after removal 72
4.16 Worst original cortical surface 73
4.17 Final reconstructed surface 73
4.18 Quality measures evolution with ring size 75
4.19 Distance growth 77
4.20 Distance histograms 77

5.1 Manual parcellation scheme in the Buckner cerebral cortex dataset 87
5.2 Original surface extracted from the segmentation 95
5.3 Mean curvature pattern for the inflated surface of subject #3 at TEA (left) and at 6 year-old (right) 95
5.4 Medial view of the white surface of the right hemisphere of subject #2 96
5.5 Sulcal profiles for the same subject's surfaces a two different time point 97
5.6 Sulcal profile of the Freesurfer's a sample subject 98

C.1 Fetal weight percentiles throughout gestation. 116

E.1 Schematic representation of the Louvain algorithm 122
E.2 Mutual and variation of information logical representation 125

Preface

1

1.1 Context

The brain is probably the most complex organ of the human body, counting a trillion of interconnected nerve cells highly organized over multiple spatial scales. Such highly structured architecture supports the whole set of brain mechanisms, from basic sensorimotor processing to high-level cognitive and executive functions. Understanding its structure and how different components interact to lead to human cognition and behavior, can open the way understanding neurological dysfunction, neurocognitive and behavioral alterations and neural degeneration.

In 2005, Patric Hagmann (Hagmann, 2005) and Olaf Sporns (Sporns *et al.*, 2005) first – and simultaneously – introduced the study of brain connectivity in adults by means of connectivity matrices, the *connectome*. Since then, *connectomics* has emerged as a powerful framework to study the underlying substrate of the human brain and its structurally integrated and functionally specialized structure, with the final goal of understanding brain organization and function. This new paradigm that considers the brain as an integrative complex system modelled by a network (equivalently, a graph) makes it possible to quantify rates of brain structural variability and to associate alterations in structural substrate with brain functional deficits and psychiatric diseases. Since it has become clearer that nervous systems generally have non-random topological properties similar to many other complex systems (Vértes & Bullmore, 2014), connectomics analyses have been widely used in a broad spectrum of brain disorders such as epilepsy (Lemkaddem *et al.*, 2014), schizophrenia (Griffa *et al.*, 2015), Alzheimer's disease (AD) (Lo *et al.*, 2010), mild cognitive impairment (MCI) and remitted geriatric depression (RGD) (Bai *et al.*, 2012) (see (Griffa *et al.*, 2013) for a review).

Characterizing the normative wiring pattern of the human brain is crucial for our understanding of the architecture and workings of the human connectome, from its early stages through adolescence and adulthood (Collin & van den Heuvel, 2013). Connectomics studies in adult populations show increasing evidence that many neurocognitive and psychiatric disorders have their roots in early brain development. In this context, recent innovations in medical imaging and quantitative image analysis open new perspectives in the study of newborn data. Indeed, mapping the structural and functional core of the human brain both in disease normal development, is one of the new challenge in neuroscience.

The development of cortical axonal pathways in the human brain takes place in a series of sequential events, that begin during the transition between the embryonic and fetal period. The concatenation of these complex and intermingled mechanisms leads to the establishment of major long fiber trajectories by the neonatal period. During the fetal phase of gestation, the long-fiber expansion is first accomplished by passing the critical morphogenetic points at the diencephalic-telencephalic border and the corticostriatal junctions, to finally change its growth trajectory direction passing through the periventricular crossroads (Vasung *et al.*, 2010). This gestational phase is known to be the most important for the growth of long projections and the associative and commissural pathways in the human cerebrum. These three fiber systems (projectional, commissural and associative) have an evident different pattern of development than the neocortical fiber pathways and the limbic fiber system. Indeed, during the *gestational phase*, afferent fibers[1] "wait" in the subplate zone. It is only in the *early preterm phase* where the thalamocortical afferent fibers accumulate within the superficial subplate and grow into the cortical plate, developing synapses. In the late preterm phase (between the 33 and 35 weeks of gestation), the resolution of the subplate and the final fiber growth into the cortical plate occurs with gyration (Kostovic & Jovanov-Milosevic, 2006). The last fibers to mature are the short cortico-cortical connections, whose ontogenesis lasts even a few month after term birth.

Thus, as early as birth the baby's brain is already globally organized. However, its structure is still immature. At birth, most of the human brain cells are non-specific or dormant, waiting to be stimulated into action. The environmental stimulation that, from the moment of birth, constantly bombards the brain through the five senses, starts the ball rolling. Initiated by this sensory input, the brain begins to develop, and the baby starts to learn new skills. Then the constant practice and repetition of these skills further enhances brain growth. The first two years of life are the most dynamic of human postnatal brain development. From birth to early childhood newborn brains undergo significant modifications, with neuronal loss, dendritic proliferation and axonal growth, followed by reductions in synaptic plasticity, axonal pruning and myelination. During this developmental period, and thanks to this rapid brain structural development, the modular assignment for brain regions changes dramatically, reflecting the development of anatomical segregation and integration properties of brain networks.

The brain developmental process is highly vulnerable to perinatal insults that generally lead to widespread changes in cortical thickness, white matter structure, white matter development, myelination, de-myelination and other mechanisms. These brain injuries may translate into changes in the underlying connectivity. However, it is still unclear whether, for example, the loss of a specific tract could represent a selective degeneration of the tracts that once formed normally or could be due to inadequate pathologic development (Huang *et al.*, 2006). Recently, some studies linked apparent disruption on white matter pathways to "disconnection" syndromes with cognitive/behavioral manifestations. Indeed, it is nowadays commonly accepted that many psychiatric and neurodevelopmental disorders have their origins in alterations during the early stages of development (Collin & van den Heuvel, 2013). The question is whether subtle variations in cognitive and behavioral traits, observed during typical development or in patients with psychiatric disorders, are associated with subtle variations in structural properties of long-distance connections, that is, with variations of white matter structure development (Paus, 2010).

---

[1] Afferent neurons (otherwise known as sensory, receptor neurons, and afferent axons), carry nerve impulses from receptors or sense organs toward the central nervous system.

1.2 Motivations

Developmental connectome analyses have been used to describe quantitative differences in global connectivity in young infants. In (Batalle *et al.*, 2012), Batalle and colleagues studied the effects of *intra uterine growth restriction* (IUGR) in brain connectivity in one-year-old children, and associated these effects with impairments in later (two years of age) neurodevelopmental outcome. Long-term brain organization, and its relation with higher order cognitive skills and social cognition has been further assessed by means of connectomics in a cohort or prematurely born children evaluated at six years of age (Fischi-Gómez *et al.*, 2014). Other studies have linked white matter alterations in early development to short- and long-term neurodevelopmental and cognitive dysfunction (Baschat, 2011; Levine *et al.*, 2015). However, there is still a lack of longitudinal studies mapping the axonal developmental processes starting at birth and continuing through childhood and adolescence. Longitudinal studies are of great potential in the study of brain development and the detection of possible alterations due to disease or neurodegeneration. Understanding the changes brain structures undergo during brain development, together with brain's organization and variability, can offer insight into the developmental origin of childhood and adult brain disorders.

1.3 Contributions of the thesis and organization of the manuscript

The main goal of this thesis is to study brain development from its early stages to childhood, and propose approaches to detect alterations due to antenatal adverse conditions such as extreme prematurity and IUGR. Based on a longitudinal dataset, we have (1) studied the brain anatomical substrate of children in early childhood and related connectivity alterations due to extreme prematurity and intra uterine growth restriction to cognitive and behavioral impairments and (2) set the technical basis needed to enable a fully-automated connectome analysis in newborn data, in order to facilitate the same analysis in newborns.

1.3.1 Main contributions of the thesis

This thesis dissertation is divided in two parts and its main contributions can be classified in two categories: clinical neuroscience and technical development. The contributions of this thesis include, for the first part:

- The formulation of a **new measure of brain structural connectivity** including two terms: a term related to the large-scale brain connectivity which reflects the ”normative grid of connections" among cortical regions, and a second term reflecting the intrinsic local configuration of the fiber bundles as well as some indication of white matter maturation and myelination (to a certain extent). This new measure allowed the analysis of the effects of extreme prematurity and IUGR in the brain anatomical substrate of children at school age.

- We provide evidence that the long-range connections, mainly the ones corresponding to the **fronto-striatal circuits**, are the **most vulnerable to antenatal insults**. This system, known to mature earlier in development, plays an important role for high order cognitive and behavioral skills, generally impaired in prematurely born children.

- In both cases, we find positive **correlations** between the **structural alterations** found with our approach and **neurocognitive and behavioral** scores at school age. These first three contributions have been published in (Fischi-Gómez *et al.*, 2014)

- We define for these children **brain modular fingerprints**, showing different brain network global structures. These results may indicate different brain reorganization to overcome the deficits induced in brain structures by premature birth or prenatal restriction. These results are included in two publications in preparation.

In the second part, mainly focused on technical developments to construct the *newborn connectome*, we present:

- A **new method to reconstruct cortical surfaces** automatically extracted from newborn data. This method detects and restores geometrical inconsistencies in the surface representing the newborn cortical surface.
- We introduce a **fully automatic pipeline** to delineate anatomically meaningful cortical structures that will enable the construction of the newborn connectome in a non-supervised fashion.

1.3.2 Organization of the manuscript

The core of this dissertation is organized into two main parts: In Part I we characterize both the brain structural substrate and the topological organization of brain networks of young children born extremely premature and/or with additional prenatal growth restriction. In Part II we propose a new fully automated pipeline to parcellate the newborn cortex based on a set of longitudinal magnetic resonance images (MRI). We intend to provide the sufficient tools to perform the same analysis in a newborn dataset. Indeed, the analysis of earlier developmental time-points may shed light on the origins of the neurodevelopmental disabilities and on the overall brain reorganization seen through early childhood and adolescence. Both parts start with an *overview* section where the relevant state-of-the-art findings are reviewed.

Part I is mainly focused on brain structure and network topological characterization of children born after extreme prematurity and IUGR at school-age. It is composed of two chapters. In Chapter 2, we first compare the structural integrity of neural circuits between moderate prematurely born control subjects and children born extremely premature with (or without) additional IUGR at school age. The structural connectivity is then correlated with a battery of neurocognitive and behavioral tests described in appendix D.

In Chapter 3, we study the topology of these brain networks together with their overall organization. From the structural connectivity matrices computed in Chapter 2, we first derive the corresponding brain networks and analyse and compare them among groups. The analysis of these brain networks is done in terms of modular topology and network organizational features, together with measures of global and local integration and segregation.

Part II is entirely devoted to the technical basis needed to enable a fully-automated connectome analysis of newborn data, from surface reconstruction, to surface registration and parcellation. We address some of the technical issues which generally arise from the adaptation of algorithm designed for adults to newborn data. In Chapter 4 we present a fully automated technique that converts a geometrically inconsistent input mesh into an output mesh that is guaranteed to be topologically correct and geometrically consistent.

From the surfaces obtained in Chapters 4, in Chapter 5 we align the surfaces from same subject acquired at two different time-points: (1) at newborn age and (2) at 6 years of age. Our hypothesis is that these two surfaces are intrinsically the same, and they only differ on a scaling factor. As we assume that the localization of the main sulci and gyri is stable across the whole lifespan, a registration procedure based on sulcal landmarks is possible. In this Chapter 5 we also present anatomically coherent cortical delineations for these surfaces, that will enable the construction of the connectome during the neonatal period.

Finally, the main conclusions and contributions of this thesis together with some suggestions for future research are summarized and discussed in Chapter 6. The appendix contain some complementary information about the dataset used, additional clinical information and some methodological clarifications.

Part I

Effects of extreme prematurity and intra-uterine growth restriction in brain connectivity at school age

Overview

Every year, both in the United States of America and in Europe approx. 60,000 children (around the 10% of all births) are born extremely preterm or with intrauterine growth restriction (IUGR). Despite the increasing survival rate of these infants due to improvement in perinatal care (World Health Organisation, 2012), their long-term neurodevelopmental impairments have been recognized as a global burden to society (World Health Organisation, 2012).

Extremely premature birth is defined as babies born alive before 28 weeks of pregnancy are completed. The most widely used definition of IUGR is a fetus whose estimated weight is below the $10th$ percentile for its gestational age and whose abdominal circumference is below the $2.5th$ percentile. These two conditions are, by themselves, major risk factors for long term morbidities, including developmental disabilities such as cerebral palsy, mental retardation and a wide spectrum of learning disabilities and behavior disorders. Several studies report an increasing number of children with impaired physical health, impaired cognitive capacities and emotional and behavioral deficits (Anderson, 2004; Bhutta, 2002). Higher rates in externalizing and internalizing behaviors often lead to lower social competence (Ross *et al.*, 1990). Emotional regulation problems with emotional outbursts lead to school- and peer-relation problems. Preterm infants also have 3 times higher odds of meeting criteria for psychiatric diagnoses (Treyvaud *et al.*, 2013). Quality-of-life assessments in preterm adolescents reveal rates of poor socialization skills due to difficulties in learning and non-verbal communication. Therefore, the identification of neuroimaging biomarkers in these children at school age is crucial for understanding their cognitive and behavioral impairments (Ment *et al.*, 2009).

Regardless of the growing number of epidemiological studies linking gestational age at birth (GA) and birth weight (BW) with deficits in long-term outcome, relatively little is known about the neurostructural bases of these complex brain structural and functional abnormalities. It is now commonly accepted that risk factors such as early exposure to extra-utero environment or antenatal adverse conditions such as IUGR affects brain structure. Indeed, extreme prematurity (EP) and IUGR have both been associated with alterations in the cerebellum (Limperopoulos *et al.*, 2005), the hippocampus (Lodygensky *et al.*, 2008), in gray matter (GM) and white matter (WM) volumes (Ball *et al.*, 2012; Padilla *et al.*, 2011) as well as in cortical volume (Indeer & Hüppi, 1999; Tolsa *et al.*, 2004) and complexity (Dubois *et al.*, 2008), proving the high susceptibility of the human brain to altered fetal nutrition and/or premature birth. The question is how, and to which extent, these alterations relate (if at all) to cognitive and behavioral impairment.

Recent literature suggests that early brain developmental alterations in extremely preterms and growth restricted preterms are associated with abnormal behavior and cognition in childhood (Borradori-Tolsa *et al.*, 2005; Dubois *et al.*, 2008; Inder *et al.*, 2005). Follow-up studies have proven that adolescent children, born very preterm, show executive function impairments in tasks involving response inhibition, visual-perceptual tasks and mental flexibility (Wolke *et al.*, 2008)). Jaekel et al. write :"very preterm children score lower on overall cognitive performance, have more often multiple cognitive problems and more often specific deficits in mathematics tasks than full term children" (Jaekel & Wolke, 2013). More precisely, regional white matter abnormalities in the frontal lobe have been associated with impaired neurocognitive function in children born prematurely (Duerden *et al.*, 2013). The question then, is what are the structural changes that lead to this different impairment, which seem to be clearly dependent on the moment of fetal development where the "insult" takes place. Since the development of functional connections is clearly dependent on the establishment of cerebral fiber pathways, their maturation and myelination (Smyser *et al.*, 2010; Supekar & Others, 2010), assessing the development of WM fibers underlying the complex brain connectivity becomes key understanding the developmental origin of childhood and adult brain disorders.

As mentioned in the preface, the normal development of cortical axonal pathways happens in a series of sequential events leading to the establishment of the major trajectories as early as the neonatal period (Vasung *et al.*, 2010). In the fetal phase of development (9-15 post-conceptional weeks, PCW), growing afferent fibers wait within the subplate zone whilst during the time corresponding to early preterm phase (24-36 PCW), the thalamocortical and cortico-cortical afferents accumulate within the superficial subplate and grow into the cortical plate (Kostovic & Jovanov-Milosevic, 2006; Vasung *et al.*, 2010). This path selection, axonal waiting in the subplate zone and axonal ingrowth into the cortical plate happens in parallel with the ongoing synaptogenesis. Kanold and Shatz (Kanold & Shatz, 2006) showed that the subplate neurons, during the prenatal and early postnatal period, provide the major input to the developing cortex. These projections of transient subplate neurons and the formation of transient circuitry are highly dependent on the sensory input (Rakic, 1988, 1991; Rakic *et al.*, 1991). The experience-dependent circuitry formation (Sur & Rubenstein, 2005) and the plasticity of the cerebral cortex during this crucial period are considered as one of the major determinants shaping the adult cortical columns and fiber pathways. Thus, we can expect that early exposure to environmental factors affects the synaptogenesis, the cortical activity as well as the axonal fiber ingrowth and outgrowth (Sur & Rubenstein, 2005).

In parallel with the ongoing microstructural events, the maturation of the major fiber systems also happens in a sequential order. The maturation of limbic and projectional fibres (thalamo-cortical fibres and striatal systems) is followed by the maturation of the long and short associational corticocortical fibers (see figure 1.1). The short cortico-cortical associational connections are known to mature last, even a few months after term birth (Kostovic & Rakic, 1990). This protracted postnatal reorganization of the cortical/white matter interface (a sight of growing short cortico-cortical connections), has been described by combined MRI in vivo, in vitro and histology approach in human tissue (Kostovic *et al.*, 2007).

Considering that the developmental process is highly vulnerable to perinatal insults that generally lead to widespread changes in cortical thickness, white matter structure and development, myelination and de-myelination and other pathologies, one might expect that these brain injuries may, at their turn, translate to changes in the underlying connectivity of the developing brain. The question will be whether the subtle variations seen in cognitive and behavioral traits observed during typical development are associated to subtle variations in the structural properties of long-distance connections. In other words, if the variation in white matter structures during development due to perinatal factors may in part account for the high prevalence of cognitive and behavioral problems in preterm infants.

Diffusion MRI (dMRI) enables studying white matter tracts in-vivo and non-invasively, mapping WM cortico-cortical and cortico-subcortical connections at high spatial resolution (Hagmann *et al.*, 2010a, 2008, 2010b). Connectomes enable quantifying rates of brain structural vari-

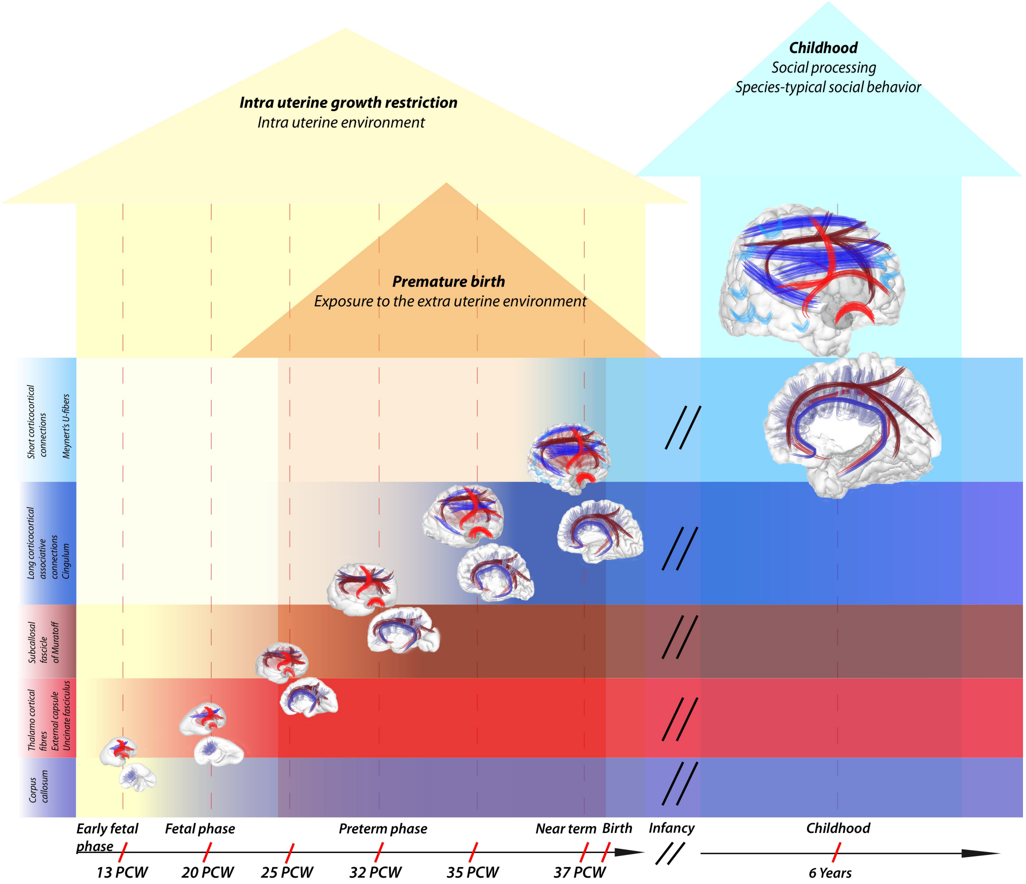

Figure 1.1: Schematic timetable of the development of axonal pathways in the human brain. Blue fibers: associational (light blue; short cortico-cortical Meynert's U fibres, sea blue; fronto-occipital fascicle, cingulum bundle, superior, medial and inferior longitudinal fascicle with its components). Red fibers: projectional (red; uncinate fascicle, capsula externa, dark red; subcallosal fascicle of Muratoff, light red; thalamocortical axons). Purple fibers: commisural. X-axis; phase of development (upper row) and age in post-conceptual weeks (lower row). Red intersections; time points at scan. Y-axis; specific fiber bundles along the x-axis. CBTCL: abbreviation for the cortico-basal ganglia-thalamo-cortical loop composed out of the cortico-striatal (Muratoff fascicle), corticoputaminal (external capsule), cortico-thalamic and uncinate fascicle. Changes in color intensity represents the intensity of histogenetic events responsible for ingrowth, path selection, outgrowth, "waiting", retraction, maturation and myelinisation of axonal pathways during the development. Changes in intrauterine environment (IUGR; yellow arrowhead), early exposure to the extra-uterine environment (premature birth; orange arrowhead) or overlap of both events suggest that the early alteration of the fiber development, due to the changes in environment, might provide altered pattern of axonal connectivity. Adapted from (Kostovic & Jovanov-Milosevic, 2006; Vasung *et al.*, 2010)

ability, and to associate defined alterations in structural substrate with brain functional deficits and psychiatric disorders. Connectomics (or the study of brain connectivity based on the connectomes), has been used in a broad spectrum of brain disorders such as epilepsy (Lemkaddem *et al.*, 2014), schizophrenia (Griffa *et al.*, 2015), Alzheimer's disease (AD) (Lo *et al.*, 2010), mild cognitive impairment (MCI) and remitted geriatric depression (RGD) (Bai *et al.*, 2012) (see (Griffa *et al.*, 2013) for a review).

Part I of this thesis dissertation is devoted to the analysis and comparison of brain connectivity patterns in school-age children born extremely preterm and/or with additional prenatal growth restriction. The main goal of the following chapters is to determine whether eventual alterations in children's brain structure underlie their poorer social and higher order cognitive functioning when reaching school age. Chapter 2 presents a whole-brain structural connectivity analysis and relates long-range and short-rage cortico-cortical and subcortico-cortical connections to behavioral and cognitive alterations. Chapter 3 characterizes the structural brain networks of children born extreme premature (with or without additional prenatal growth restrictions) and children born moderately preterm with prenatal growth restriction by means of network organizational features and measures of network integration and segregation.

Elements of the present Part I have been published in (Fischi-Gómez *et al.*, 2014).

Structural connectivity in 6 years-old preterm infants

2

2.1 Context and background

Extreme prematurity and pregnancy conditions leading to intrauterine growth restriction (IUGR) affect thousands of newborns every year and increase their risk for poor higher order cognitive and social skills at school age. However, little is known about the brain structural basis of these disabilities. To compare the structural integrity of neural circuits between prematurely born controls and children born extremely preterm (EP) or with IUGR at school age, long-range and short-range connections were noninvasively mapped across cortical hemispheres by computing connection matrices derived from diffusion weighted images (DWI). Brain connectivity was modelled along fiber bundles connecting 83 brain regions by a weighted characterization of structural connectivity (SC). EP and IUGR subjects, when compared with controls, had decreased SC in the cortico-basal ganglia-thalamo-cortical loop connections while cortico-cortical association connections showed both decreased and increased SC. The strength of these altered connections was associated with poorer socio-cognitive performance in both EP and IUGR children.

2.2 Material and methods

In the upcoming chapters we define the methods used for our analysis, and the inclusion criteria in each group of our subjects. The dataset, composed of a set of MR scans performed longitudinally at three different time-points, from birth to childhood, is described in appendix C. For the analysis presented in this first part of the thesis (Chapters 2 and 3) we used the latest time-point acquisitions. Children were scanned at 6 years of age.

2.2.1 Subjects

Sixty prematurely born children were recruited from the Child Development Units of the Centre Hospitalier Universitaire Vaudois (CHUV), Lausanne, and the Hôpitaux Universitaires de Genève (HUG), Switzerland. Infant growth parameters (i.e., weight and head circumference measures) and perinatal data, including birth weight (BW), gestational age (GA), gender, APGAR score, and the presence of perinatal morbidities was prospectively recorder for all subjects (Table 2.1). The recruitment of the children started in 2002 and last until 2010. Children were scanned a 3 different time-points: (i) at birth, provided that newborn infants did not need any clinical support such as artificial ventilation, (ii) at term equivalent age, i.e. 40 weeks of corrected gestational age and (ii) at 6 years-old.

None of the children had any sign of prematurity-associated brain lesions on MRI at term equivalent age, as assessed by preterm brain injury scores(Woodward *et al.*, 2006). Furthermore, at 6 years, their MRI scans were read as normal by experienced neuroradiologists. All of the recruited children were free from medication and from psychiatric or neurological disease (Table 2.1). All studies were performed with informed parental and child consent after approval by the medical ethical board. After preprocessing and quality evaluation of the MRI images, 52 subjects were finally included in the analysis (Table 2.1).

Children under study were classified as (1) moderately premature controls, (2) extremely premature (EP), or (3) moderately premature with IUGR (see appendix C, table 2.1). Extreme prematurity was defined by GA at birth of <28 weeks. IUGR was defined as BW below the 10th percentile (adjusted for GA and gender) and on criteria of placental insufficiency according to intrauterine growth assessment, prenatal ultrasound, and Doppler measurement within the umbilical artery. Infants considered to be controls were born with a BW appropriate for their GA without extreme prematurity. Our definition of control subjects was based on the fact that moderately premature infants with normal growth generally compare with children born full term in their structural brain development (Zacharia *et al.*, 2006).

2.2.2 Connectivity estimation

For each subject, the whole brain structural connectivity was determined by tissue segmentation and streamline tractography (see Appendix A). This processing yielded 52 weighted structural matrices, each one composed of $n = 83$ nodes (each node being a cortical and subcortical region, according to the parcellation described in (Cammoun *et al.*, 2012)), and with edge weights $w(i, j)$ representing the streamline connectivity density (Hagmann *et al.*, 2008) between regions (i, j).

Following (Hagmann *et al.*, 2010a,b), the structural connectivity (SC) between cortical regions was defined as the product of 2 components (see AppendixA). The first component is the group connection density (gCD), computed as the following: the individual CD matrices are normalized 1) by the size of the cortical regions and 2) by the length of the fiber bundle connecting 2 regions. The group CD matrices (gCD), are then computed as the mean of all normalized connection matrices in a given group. Since the mean is non-null if at least one of the elements is non-null, these group average connectivity matrices consist of support of the connectivity in each group and represent the maximum grid for each group. No statistically significant differences in average strength and network density were observed, comparing these support gCD matrices. This fact was expected due to the absence of gross brain pathology. The second component is the connection efficacy, considered to be subject-dependent. It was computed as the mean fractional anisotropy (FA) value of the bundle connecting 2 regions (in the FA-weighted analysis) and as the mean of the inverse apparent diffusion coefficient (ADC) in the ADC-weighted analysis. As we do not consider connections for which the connectivity is 0 for one group and > 0 for the other group in the second-level connection-wise analysis, we can say that, in this situation, we are using the minimum grid as support for this specific analysis. The FA scalar was chosen as it is though to reflect fiber density, axonal diameter and myelination in white matter. On the other hand, the ADC measure was chosen as t is considered to be an indicator of white matter maturation and myelination.

Perinatal Data	EP	IUGR	Control
	(< 28 w GA)	(IUGR)	(> 28w GA no IUGR)
n subjects	23	21	8
Child sex (male/female)	8/15	10/11	4/4
GA	26.75(1.03)	29.84(3.12)	32.02(2.47)
BW	960.87(193.50)	931.90(335.60)	1652.50(402.45)
BW z-score	0.26(1.03)	−1.76(0.63)	−0.30(0.81)
APGAR score 1	52.17	28.57	0
APGAR score 2	4.34	9.52	0
APGAR score 3	4.34	4.76	0
Ventilation (yes)	82.60	52.38 25	
Asphyxia (yes)	43.47	28.57	0
IVH none	91.32	85.72	0
IVH grade I	4.34	4.76	0
IVH grade II	4.34	9.52	0
Infection none	91.32	85.72	0
Infection suspicion	39.14	42.85	37.5
Infection proven	30.43	28.57	0
Neurological exam at 6 years (normal)	100	100	100
Family SES low	21.73	9.52	12.5
Family SES medium	65.21	28.57	25
Family SES high	13.06	61.91	62.5

Table 2.1: Sample characteristics of the study participants according to gestational age (GA) and presence of intrauterine growth restriction (IUGR) at 6 years old. Cases with severe neurological impairment are not included in the study. APGAR scores: Percentage of children showing an APGAR score below 7 for each APGAR test. APGAR test: Performed one minute (score 1), five minutes (score 2) after birth and each 5 minutes until score > 7 (score 3) (max. 20 minutes). Scores 7 and above are generally normal, 4 to 6 fairly low, and 3 and below are generally regarded as critically low. IVH: Intra-ventricular haemorrhage. 3 SES: Socio-economic status. Data is presented as mean (standard deviation) for continuous variables and percentage for categorical variables.

2.2.3 Statistical analysis

The resulting connectomes were compared globally and locally using the Mann–Whitney nonparametric test, and the resulting p-values were corrected for multiple comparisons. This later step was performed using a two-step methodology specially designed for connectomes (Meskaldji *et al.*, 2011, 2013) (see Appendix B for more information). This new statistical correction exploits the information data structure and positive dependence of the data to increase the power of testing and is based on grouping tests into subsets in which tests are supposed to be positively dependent. In our analysis, tests were grouped in meaningful disjoint anatomical groups of ROIs based on a recent study (Chen *et al.*, 2012). In their work, Chen et al. grouped the cortical areas that share similar genetic patterns. In short, they first measured relative areal surface expansion using the cortical surface reconstruction and spherical atlas mapping developed by (**?**). They then estimate genetic correlations between different points of the cortical surface, to finally cluster the regions using an unsupervised pattern recognition method. This parcellation system reflects shared genetic influence in regional differentiation in humans, demonstrating a biologically sensible organization of the structure of the human cortex.

We define subsets of connections by either the intraconnectivity or the interconnectivity between the groups of ROIs defined by the Chen decomposition. In each of the subsets, a screening of the data using a summary statistic (in our analysis, the averaged SC was used) at a predefined threshold of $\alpha = 0.05$. This first step was followed by a local investigation of the statistically significant subsets in such a way that the global family-wise error rate (FWER) was controlled at a significance level $\frac{\alpha}{M}$, being M the number of subsets (Fischi-Gómez *et al.*, 2014; Meskaldji *et al.*, 2011, 2013)(see A). FA-weighted (FAw) and ADC-weighted (ADCw) global mean connectivity was calculated for: (1) whole brain (mean FA-weighted SC [FAw-SC] and mean ADC-weighted SC [ADCw-SC] of all edges in all subjects in each group), (2) intrahemispheric left and right (mean FAw-SC and mean ADCw-SC of all intrahemispheric edges in all subjects in each group), and (3) interhemispheric connections (mean FAw-SC and mean ADCw-SC of all interhemispheric edges in all subjects in each group) and compared between groups using the Mann–Whitney test and Bonferroni correction. Finally, in order to relate the differences found in brain's biological substrate with the complex changes in cognition and behavior, connections that show significantly altered FAw-SC were correlated with socio-cognitive scores (KABC, SDQ an SRT) using Pearson's correlation. The resulting with p-values were corrected using a false discovery rate (FDR) control.

2.3 Results

2.3.1 Global connectivity

When compared to control subjects, both EP and IUGR subjects showed changes in FAw-SC in terms of mean connectivity in the whole brain, left, and right intrahemispheric connections and interhemispheric connections. The global ADCw-SC analysis showed significant differences between EPs and controls in the interhemispheric mean connectivity while IUGR subjects, when compared to controls, showed differences in whole-brain mean connectivity as well as intrahemispheric mean connectivity (both right and left).

2.3.2 Local connectivity changes in FA-weighted structural connectivity

2.3.2.1 Changes in FAw-SC after extreme prematurity (EP vs. Controls)

The local analysis revealed pairwise FAw-SC alterations in both interhemispheric and intrahemispheric connections in EP children (see Fig. 2.1). The majority of these altered connections showed weaker FAw-SC (Fig. 2.1; red-, yellow-, and orange-coloured connections), in particular in the callosal connections belonging to precuneus and isthmus of cingulate gyrus (Fig. 2.1; yellow-coloured connections)and in the cortico-basal ganglia-thalamo cortical loop connections (CBTCL Fig. 2.1; red-coloured connections). These connections were mostly fronto-subcortical connections between superior frontal gyrus and subcortical gray matter (thalamus, globus pallidus, putamen, and caudate nucleus) (Fig. 2.1; red-coloured connections). Connections of the orbital and medial networks (between the lateral and medial orbital cortex, basal ganglia, prefrontal cortex, and gyrus cinguli) were significantly weaker in EP children. Differences in the subthalamic and brainstem connections were also found (Fig.2.1); yellow-coloured connections. Furthermore, short connections between neighbouring cortical regions were also found weaker in EP (Fig. 2.1; orange-coloured connections). These connections were short cortico-cortical connections in the prefrontal cortex (middle frontal gyrus and inferior frontal gyrus), cingulate gyrus (posterior part and isthmus), precuneus, and between neighbouring parietal and temporal cortices (supramarginal gyrus, superior temporal gyrus, transverse temporal gyrus, inferior parietal lobule). While all of the altered connections showing increased FAw-SC were short cortico-cortical connections (Fig. 2.1; blue-coloured connections), the majority of them were connections between neighbouring regions of the temporal cortex (fusiform, superior, middle and inferior temporal and lingual gyrus).

2.3.2.2 Changes in FAw-SC after IUGR (IUGR vs. Controls)

Comparing IUGR children to control subjects also revealed altered interhemispheric and intrahemispheric connections (Fig. 2.3). Similar to EP, the majority of altered connections in IUGR showed weaker FAw-SC (Fig. 2.3; yellow-, orange-, and red-coloured connections). Interhemispheric callosal connections belonging to the superior frontal gyrus, precuneus, and cingulate gyrus were found significantly weaker in IUGR children (Fig. 2.3; yellow-coloured connections). Intrahemispherically IUGR subjects also showed altered fronto-subcortical connections, mostly between teh middle frontal gyrus and the subcortical gray structures (putamen, globus pallidus, thalamus) (Fig. 2.3; red-coloured connections). In addition, many of the altered connections belonging to the CBTCL were short connections between subcortical gray matter structures (globus pallidus, thalamus, nucleus caudatus, and nucleus accumbens, Fig.2.3; red-coloured connections). Connections of the orbital and medial networks were significantly weaker in IUGR children as well as some of the subthalamic and brainstem connections (Fig.2.3; yellow-coloured connections). Although short cortico-cortical connections between neighboring cortical regions were also weaker in IUGR children, these connections were widespread through the telencephalon (Fig. 2.3; orange-coloured connections). Increased FAw-SC was found only in short cortico-cortical connections of temporal (middle temporal gyrus) and inferior frontal gyrus (pars opercularis) (see Fig. 2.3; blue-coloured connections).

2.3.2.3 Differences in FAw-SC between EP and IUGR

As summarized in Figure 2.5, comparing IUGR children to EP subjects directly revealed only intrahemispheric FAw-SC alterations. When compared with the EP group, reduced connectivity in the IUGR group was found again in the CBTCL (Fig. 2.5); red-colored connections. However, these alterations appeared only in the right hemisphere, in connections between parietal cortex (supramarginal gyrus and inferior parietal lobule) and subcortical gray matter (putamen, globus

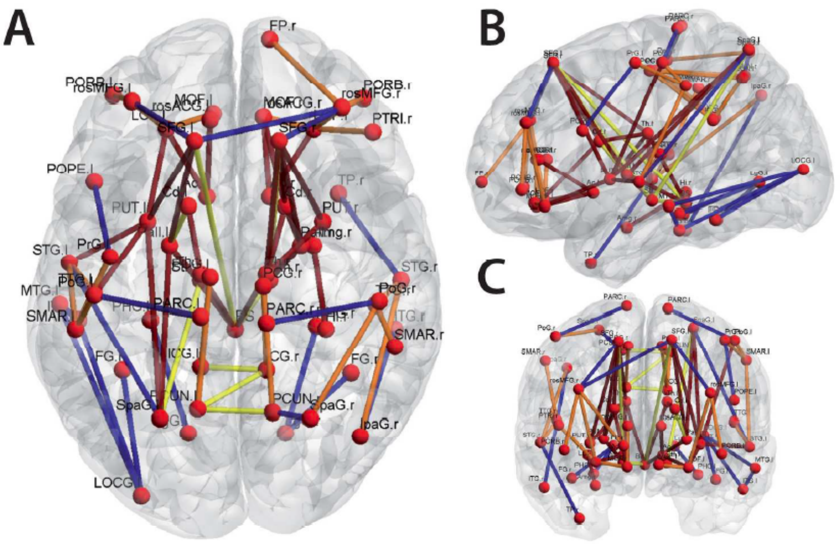

Figure 2.1: Connections altered in EP children at school age (A-C). 2D-projection to axial (A), sagittal (B) and coronal planes (C) of all connections showing statistically significant FAw-SC decrease (EP < controls (red, orange and yellow-coloured connections)) or increase (EP > controls (blue-coloured connections)) when compared to controls. ($p - value < 0.05$, corrected). 2D projections were reconstructed using the BrainNet Viewer software (Xia *et al.*, 2013).

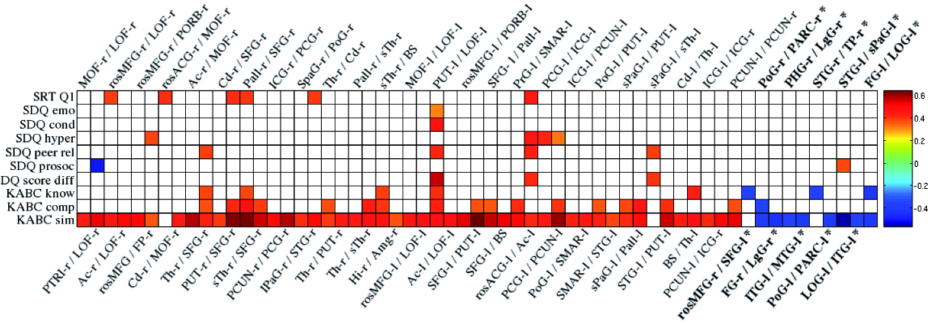

Figure 2.2: Correlation between altered connections and socio-cognitive outcome $p - value < 0.05$, FDR corrected). Each coloured box indicates the Pearson's correlation coefficient, r (color bar on the right). Correlations that did not show statistical significance were not inserted. Abbreviations; *, stronger connections in EP. For the assessment of social skills, the SRT (SRT Q1=Judgment score, SRT Q2=Identification score), SDQ prosocial and SDQ peer relation questionnaire were administered. For assessment of higher cognitive skills KABC and SDQ were administered. Higher KABC scores indicate higher cognitive performance. SDQ emotion, conduct, hyperactivity, difficulties and peer relation scores use an inverse scale relative to performance (higher performance, lower score). Therefore, for illustration purposes they were inverted in the table.

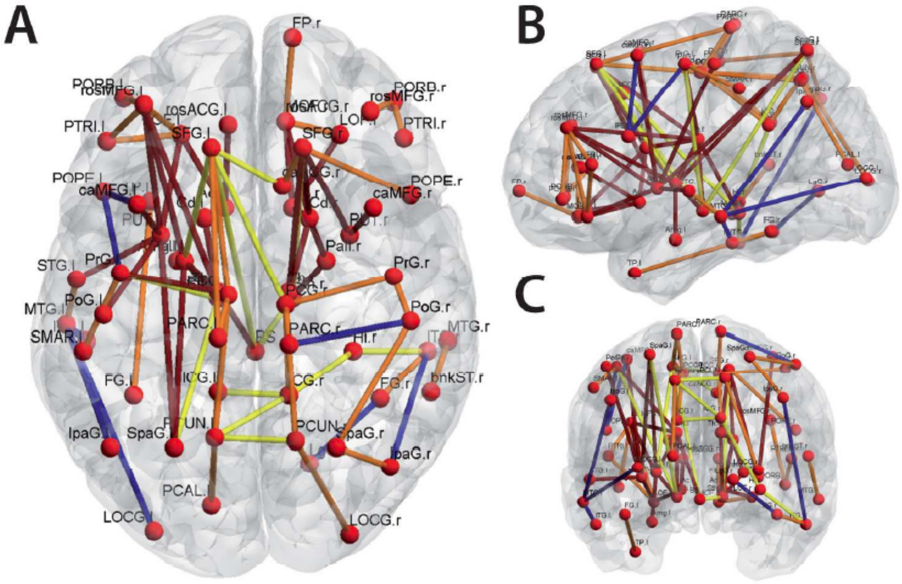

Figure 2.3: Connections altered in IUGR children at school age (A-C). 2D-projection to axial (A), sagittal (B) and coronal planes (C) of all connections showing statistically significant FAw-SC decrease (IUGR < controls (red, orange and yellow-coloured connections)) or increase (IUGR > controls (blue-coloured connections)) when compared to controls ($p - value < 0.05$, corrected). 2D projections were reconstructed using the BrainNet Viewer software (Xia *et al.*, 2013).

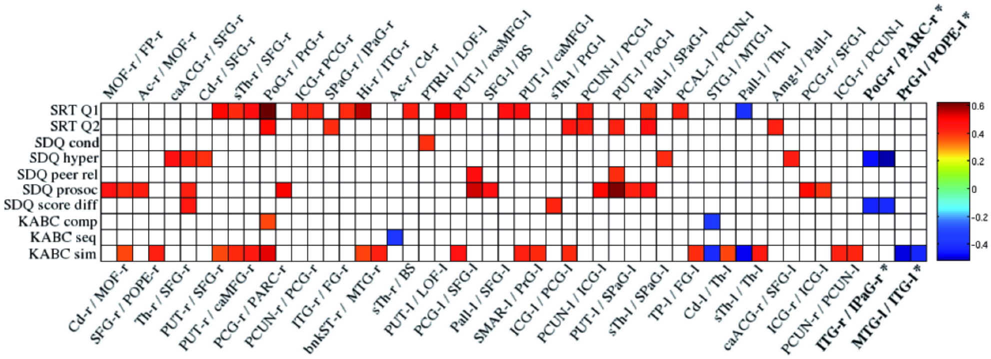

Figure 2.4: Correlation between altered connections and socio-cognitive outcome $p - value < 0.05$, FDR corrected). Each coloured box indicates the Pearson's correlation coefficient, r (color bar on the right). Correlations that did not show statistical significance were not inserted. Abbreviations; *, stronger connections in IUGR. For the assessment of social skills, the SRT (SRT Q1=Judgment score, SRT Q2=Identification score), SDQ prosocial and SDQ peer relation questionnaire were administered. For assessment of higher cognitive skills KABC and SDQ were administered. Higher KABC scores indicate higher cognitive performance. SDQ emotion, conduct, hyperactivity, difficulties and peer relation scores use an inverse scale relative to performance (higher performance, lower score). Therefore, for illustration purposes they were inverted in the table.

pallidus, amygdala, and thalamus) (see Fig.2.5; red-coloured connections). EP showed decreased connectivity, compared to IUGR, only in cortico-cortical connections of the left hemisphere; long cortico-cortical connections (between the temporal (superior temporal) and prefrontal cortex (middle and inferior frontal gyrus)) and short cortico-cortical connections (between the inferior and middle frontal gyri) (Fig. 2.5; blue-colored connections).

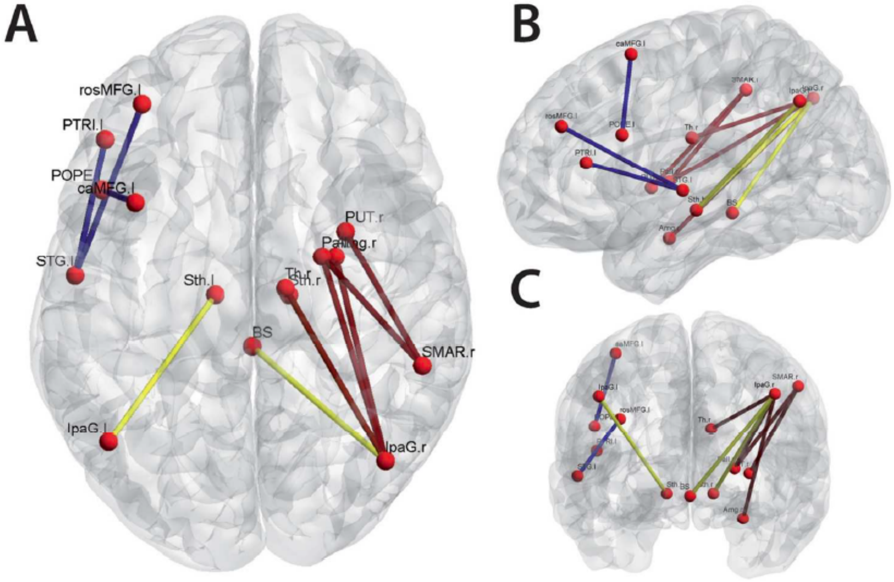

Figure 2.5: Altered connections between IUGR and EP children at school age. 2D-projection to axial (A), sagital (B), and coronal planes (C) of connections showing statistically significant FAw-SC decrease in IUGR ($IUGR < EP$; in red-the cortico-basal ganglia-thalamo-cortical loop connections; in yellow-brainstem, subthalamic, and callosal connections) or decrease in EP (EP<IUGR; in blue-intrahemispheric cortico-cortical connections) when comparing the 2 groups. 2D projections were reconstructed using the BrainNet Viewer software (Xia *et al.*, 2013).

2.3.2.4 Social and higher order cognitive evaluation

Exploratory regression analysis revealed a significant association between lower GA and poorer achievement on KABC simultaneous processing subscales (appendix D, table D.2 $p <$ 0.05 5, uncorrected, after adjustment for sex, SES, and IUGR). IUGR also showed significant association with lower KABC simultaneous processing scores (appendix D, table D.2, $p < 0.05$, uncorrected, adjusted for GA, sex, and SES). Furthermore, IUGR when tested for social skills and adjusted for GA, sex, and SES showed significant association with lower scores, poorer social skills (on average 1.3 points with a standard error 0.56), on the SDQ prosocial behavior questionnaire and SRT (SRT Q1 (Judgment score) (appendix D, table D.2, $p < 0.05$, uncorrected, adjusted for GA, sex, and SES).

2.3.2.5 Correlation of altered FAw-SC with socio-cognitive scores

The FAw-SC of the majority of connections, identified as weaker in EP, correlated positively (i.e., decreased connectivity led to decreased score) with the KABC simultaneous score (see

Fig. 2.2). The FAw-SC of certain connections (connections of the superior frontal gyrus and the lateral orbitofrontal cortex), also identified as weaker in EP, positively correlated with the SRT judgement score (Fig. 2.2). Additionally, in EP, SDQ hyperactivity scores were negatively correlated with FAw-SC of anterior cingulate CBTCL connections (connections between anterior cingulate gyrus and nucleus accumbens) and short cortico-cortical connections (connections between posterior cingulate and isthmus gyri, precuneu,s middle frontal gyrus and frontal pole) of the left hemisphere. As SDQ hyperactivity uses an inverse scale relative to performance (lower scores, better performance) the lower FAw-SC of these connections was associated with higher hyperactivity (poorer outcome). Inversely, FAw-SC of cortico-cortical connections, identified as stronger in EP, still correlated negatively with the KABC simultaneous score (higher strength of connectivity indicated lower KABC score, see connections marked with ($*$) in Fig. 2.2).

For the IUGR subjects, the correlations between FAw-SC and socio-cognitive scores appeared less homogenous than in the EP group. The FAw-SC of the connections identified as weaker in IUGR correlated positively with SRT Q1 in most cases. These connections were mainly the ones belonging to the fronto-subcortical and parieto-subcortical circuits. Some of the connections altered in IUGR subjects correlated positively with the SRT Q2, the SDQ prosocial (connections between the medial orbito-frontal, prefrontal and parietal cortices and the basal ganglia), the SDQ hyperactivity (fronto-subcortical and parieto-subcortical connections) and the KABC simultaneous scores (fronto-subcortical, callosal, and short cortico-cortical connections of temporal lobe), Fig. 2.4. FAw-SC of short cortico-cortical connections, identified as stronger in IUGR, correlated negatively with the behavior and KABC simultaneous scores (Fig. 2.4; connections marked with ($*$)).

These findings are summarized in 2 schematic drawings (Figs. 2.6 and 2.7) for a better anatomical illustration. Both figures show only the altered connections in EP (Fig. 2.6) and IUGR (Fig. 2.7), whose FAw-SC significantly correlates with socio-cognitive performance (bold lines and dotted lines represent positive and negative correlations, respectively). Note that the majority of altered connections whose strength is associated with socio-cognitive performance belong to prefronto-subcortical circuits.

2.4 Discussion

Extremely premature birth and/or poor intrauterine growth affect social and higher order cognitive functions in school-age children (Larroque *et al.*, 2008). In this context, the study presented in this thesis chapter delineates, using a whole-brain connectome approach, global and regional brain structural connectivity alterations and relates this brain connectivity and network changes with social and higher order cognitive functions in EP and IUGR school-age children.

2.4.1 Global connectivity analysis

The mean ADCw-SC (considered as an indicator of WM maturation and myelination) was reduced in the interhemispheric WM pathways in EP, whereas, in IUGR children, it was reduced in intrahemispheric WM pathways . It is known that the forebrain commissures are unmyelinated at birth and that the process of myelination of axonal fibers, especially in the corpus callosum, continues into adolescence (Keshavan *et al.*, 2002). Thus, our results suggest that reduced mean ADCw-SC of the interhemispheric connections in EP reflect changes in the maturation of callosal fibers. These results are in agreement with previously reported DWI studies showing microstructural WM changes of major WM fiber tracts associated with premature birth (for review see

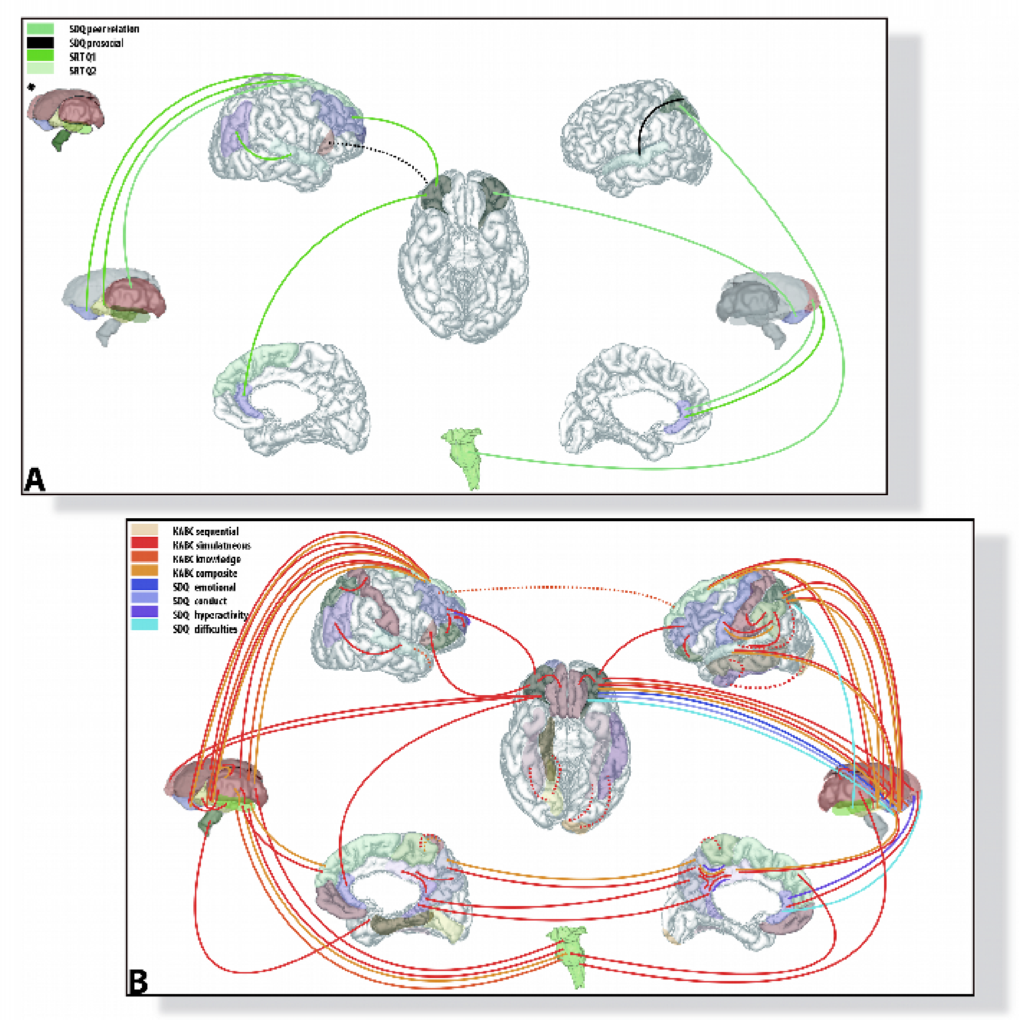

Figure 2.6: Schematic drawing of altered connections in EP subjects whose FAw-SC strength correlates with socio-cognitive outcome. Drawn altered connections are connections from Figure 1D. Social reasoning skills, peer problems and prosocial behavior are shown in (A) Higher cognitive skills are shown in (B). Dotted lines: negative correlation. Continuous lines: positive correlation. For assessment of social skills SRT (SRT Q1=Judgment score, SRT Q2=Identification score), SDQ prosocial and SDQ peer relation questionnaire were administered. For assessment of higher cognitive skills, KABC and SDQ were administered. Higher KABC scores indicate higher cognitive performance. SDQ emotion, conduct, hyperactivity, difficulties, and peer relation scores use an inverse scale relative to performance (higher performance, lower score). Therefore, for illustration purposes, they were inverted in the figure. Basal ganglia reconstruction; nucleus accumbens (light red), nucleus caudatus (brown), thalamus (red), putamen (purple), globus pallidus (yellow), subthalamus (light green), and amygdala (dark green). 3D cortical surfaces were reconstructed using the CIVET software developed bythe ACE lab (http://www.bic.mni.mcgill.ca/ServicesSoftware/CIVET (MacDonald *et al.*, 2000))

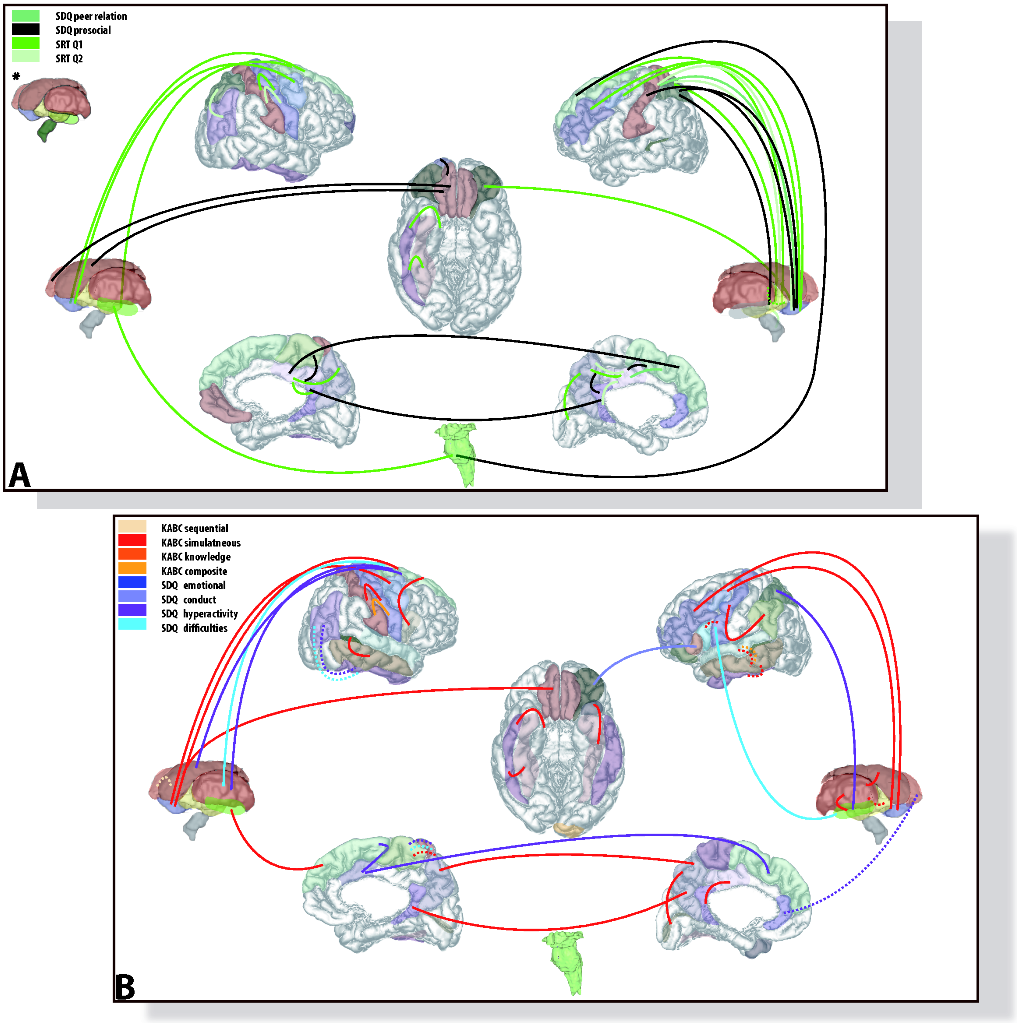

Figure 2.7: Schematic drawing of altered connections in IUGR subjects whose FAw-SC strength correlates with socio-cognitive outcome. Drawn altered connections are connections from Figure 2D. Social reasoning skills, peer problems, and prosocial behavior are shown in (A) Higher cognitive skills are shown in (B). Dotted lines: negative correlation. Continuous line: positive correlation. For assessment of social skills, SRT (SRT Q1=Judgment score, SRT Q2=Identification score), SDQ prosocial and SDQ peer relation questionnaire were administered. For assessment of higher cognitive skills, KABC and SDQ were administered. Higher KABC scores indicate higher cognitive performance. SDQ emotion, conduct, hyperactivity, difficulties, and peer relation scores use an inverse scale relative to performance (higher performance, lower score). Therefore, for illustration purposes, they were inverted in the figure. $*3D$ basal ganglia reconstruction; nucleus accumbens (light red), nucleus caudatus (brown), thalamus (red), putamen (purple), globus pallidus (yellow), subthalamus (light green) and amygdala (dark green). 3D cortical surfaces were reconstructed using the CIVET software developed by the ACE lab (http://www.bic.mni. mcgill.ca/ServicesSoftware/CIVET (MacDonald *et al.*, 2000))

(Ment *et al.*, 2009)).

The global mean FA was significantly altered for interhemispheric as well as for intrahemispheric SC in both groups (EP and IUGR). This provides new evidence that alterations in WM maturation which are associated to premature birth are present not only, as previously demonstrated, at birth and term equivalent age (Hüppi & Dubois, 2006; Hüppi *et al.*, 1998), but also persist upon reaching school age. Furthermore, our results show that poor fetal conditions leading to IUGR provoke structural abnormalities similar to ones seen in EP, with high impact on their socio-cognitive potential.

2.4.2 Local Connectivity Analysis

During development, major WM fiber systems display specific spatio-temporal maturation (Vasung *et al.*, 2010). The maturation of thalamo-cortical fibers and striatal fibers of the CBTCL is followed by the maturation of the associational long (intrahemispheric and interhemispheric) and short cortico-cortical fibers (Kostovic & Jovanov-Milosevic, 2006; Vasung *et al.*, 2010). Our results indicate that early maturing fiber systems (e.g.,thalamo-cortical fibers, striatal fibers) have decreased FAw-SC at school age in EP and IUGR children (Figs 2.1 and 2.3). In contrast, late maturing fiber systems (mostly the associational cortico-cortical fibers) have both decreased (Figs 2.1 and 2.3; orange-coloured connections) and increased FAw-SC (Figs. 2.1 and 2.3; blue-coloured connections). Such differences in FAw-SC strength suggest different vulnerability and developmental trajectories of the aforementioned fiber systems.

2.4.2.1 Connections with weaker FAw-SC

Cortico-Basal Ganglia-Thalamo-Cortical Loop (CBTCL)

The CBTCL is a model of the functional and anatomical organization of cortico-basal ganglia-thalamo-cortical pathways (Cummings, 1993) that play an important role in human behavior. In this study,connectivity alterations in the CBTCL connections were common in both groups (EP and IUGR) when compared with controls (see Figs 2.1 and 2.3; red-coloured connections) and were linked with the level of their socio-cognitive performance (Figs 2.6 and 2.7). The relationship between the cortex, the basal ganglia, and the thalamus in terms of information processing is complex and has been an area of scientific debate for years (Goldman-Rakic & Selemon, 1990). The basal ganglia receive inputs from the majority of cortical areas. This flux of information is then transferred to the thalamus that serves as a relay for the basal ganglia projections back to the cortex (Alexander *et al.*, 1986; Cummings, 1993, 1995; Mega & Cummings, 1994; Parent & Hazrati, 1995; Takada *et al.*, 1998). Recent imaging data using probabilistic tractography demonstrated the structural basis of the CBTCL at the global level (Draganski *et al.*, 2008). The parallel organization of cortico-striatal circuits belonging to the CBTCL allows simultaneous processing of cognitive, sensorimotor, and motivational information (Groenewegen *et al.*, 2009). Our results suggest that weaker connections within this circuit might be a biological blueprint of less efficient simultaneous information processing seen in EP and IUGR children (Figs 2.2, 2.4, 2.6 and 2.7). In addition, the connectivity alterations that we found in EP and IUGR suggest that the most vulnerable part of this loop consists of the components belonging to the prefronto-subcortical and limbic circuits (Figs 2.1 and 2.3; red-coloured connections). The prefronto-subcortical circuits are referred to as major mediators of the executive, social, and motivated human behavior (Cummings, 1993, 1995; Parent & Hazrati, 1995), shown to be affected by premature birth (Nosarti *et al.*, 2010). Moreover, these circuits have also been implicated in psychiatric disorders (Mega & Cummings, 1994) which are known to occur with higher prevalence in prematurely born children (Nosarti *et al.*, 2010) and individuals with low BW.

Orbitofrontal circuits of the CBTCL

Different connections belonging to orbital and medial network circuitry were found to be weaker in EP and IUGR children (Figs 2.1 and 2.3; red-coloured connections). The orbital network serves as a system for sensory integration while the medial prefrontal network plays an important role in reward-related learning, extinction, and reality check and fantasies, or in keeping thought and behavior in phase with reality (Ongur & Price, 2000; Schnider, 2008). A neuroimaging study in adolescents associated the alteration of orbitofrontal sulcal depth with prematurity (Gimenez *et al.*, 2006), suggesting altered maturation of orbitofrontal cortex after premature birth. In recent years, alterations of the orbitofrontal cortex have further been associated with impaired social behavior, poor reward-based decision making and disturbances in emotional processing. Our results support these findings since in EP and IUGR children weaker strength of connections belonging to medial and orbital networks (Figs 2.1 and 2.3) correlated with deficits in recognition of social context, social recognition abilities, simultaneous processing, and hyperactivity (Figs 2.6 and 2.7). Therefore, the results presented here suggest that these networks might be responsible for lower social competences seen in prematurely born children, as already assessed in (Ross *et al.*, 1990).

CBTCL alteration in relation to injury

Primary lesions from acquired insults that are associated with premature birth were extensively studied, for review see (Volpe, 2009). The predilection sights of these lesions are periventricular regions. *Periventricular crossroad areas*, situated in periventricular regions, have been recently described as being crucial for proper navigation and growth of axonal pathways during human brain development (Judas *et al.*, 2005). During fetal development, an abundant periventricular fiber pathway (PVP) (Vasung *et al.*, 2011) is situated within these areas. Since the PVP is made of the fronto-occipital fascicle, the corpus callosum, the fronto-pontine pathway, and the Muratoff fascicle (major route for cortico-striatal fibers (Schmahmann & Pandya, 2006; Vasung *et al.*, 2011), we suspect that discrete injury in these *periventricular crossroad areas* might lead to altered callosal, brainstem, and cortico-striatal connectivity (CBTC).

Additionally, (Pierson & Others, 2007) reported that primary injury of the WM does not happen in isolation, but it is associated with significant neuronal loss and/or gliosis within the basal ganglia and thalamus. Neuroimaging studies have recently shown decreased volumes of thalamus and weaker thalamo-cortical connections in prematurely born infants (Ball *et al.*, 2012). Therefore, discrete injury of periventricular regions affecting the major route for cortico-striatal fibres (the Murratoff fascicle) and neuronal loss within basal ganglia could partially explain the weaker connectivity within the CBTCL that we found in EP and IUGR preterm children (Figs 2.1 and 2.3; red-coloured connections).

Short associational cortico-cortical connections

Language associated areas

Comparing IUGR to EP revealed that EP children display weaker FAw-SC in connections belonging to regions associated with language processing, namely pars opercularis and pars triangularis of inferior frontal gyrus (Fig. 2.5; blue-coloured connections). It has been shown that low BW and extreme prematurity are associated with poorer language skills at almost all levels, from expressive to receptive language, phonological awareness, discourse, semantics, and pragmatics (Barre & Others, 2011; Foster-Cohen *et al.*, 2007; Marston *et al.*, 2007; Ramon-Casas *et al.*, 2012; Wolke *et al.*, 2008). Furthermore, recent imaging findings, showing connectivity alterations of similar areas as in the current study, suggest that these children recruit alternate cortical regions for language processing (Gozzo *et al.*, 2009). Our results provide further evidence of altered (decreased) SC between cortical areas relevant for language processing (Figs 2.1 and 2.3; orange-coloured connections).

Precuneus

One of the most striking alterations was found in cortico-cortical connections between the precuneus and neighboring regions (Figs 2.1 and 2.3; orange-coloured connections). The precuneus has been reported to have a major role in a broad spectrum of complex cognitive tasks, including visuo-spatial imagery, episodic memory retrieval, and self-processing.

However, during the resting state of the brain, the precuneus and the posterior regions of the medio-sagital cortex show synchronous activity patterns and have been referred to as being part of the *default mode network* (DMN) functionally linked to self-consciousness (Cavanna & Trimble, 2006). DMN is known to appear later in development of preterm infants (Smyser *et al.*, 2010). Our results showing reduced connectivity between these 2 major hubs of the DMN (posterior cingulate gyrus and posterior precuneus) at 6 years of age, suggest that the alteration of this basic structural and functional network is important for functional integration of information processing (Hagmann *et al.*, 2008, 2007). Significant correlation with the cognitive outcome provided evidence that weaker strength of connections belonging to these circuits might contribute to their less efficient simultaneous information processing, poor recognition of social context, and poor prosocial behavior (Figs 2.2, 2.4, 2.6, and 2.7).

2.4.2.2 Connections with stronger FAw-SC

Short associational cortico-cortical connections

Although the human brain develops in distinct stages of genetic activity (Pletikos *et al.*, 2014), experience-dependent structural changes are generally described within the GM. These changes, associated with synaptogenesis and dendritic arborization (Petanjek & Kostovic, 2012), contribute to functional plasticity (Turner & Greenough, 1985; Volkmar & Greenough, 1972). Training and rehabilitation are further known to affect the cortico-cortical rewiring, and recent DWI data show that training induces changes in the WM architecture (Scholz et al. 2009). In our study, all connections with significantly increased FAw-SC in EP and IUGR were short cortico-cortical connections (Figs 2.1 and 2.3; blue-coloured connections). Nevertheless, none of these connections were associated with improved measures of the socio-cognitive outcome. On the contrary, they were associated with less efficient simultaneous processing and higher rates of hyperactivity (Figs 2.2, 2.4, 2.6, and 2.7). Thus, our results indicate that this increase in connectivity strength does not necessarily mean a better socio-cognitive performance but might occur in order to compensate for weaker parts of network circuitry.

2.4.3 Implications for understanding cognition and behavior

When reaching school age, EP children show deficits in motor, sensory and executive functioning (Marlow *et al.*, 2007). Moreover, they display problems in processing complex information that needs logical reasoning and spatial orientation abilities (Larroque *et al.*, 2008). As these cognitive deficits have a similar incidence in EP and IUGR preterm infants (born between 29 and 32 weeks) (Guellec *et al.*, 2011), similar connectivity alterations found in the EP and IUGR subjects speaks in favour of their similar neural substrate. The current analysis suggests that the alterations in the CBTCL and the short cortico-cortical connections following preterm birth and IUGR might contribute to poorer prosocial behavior, recognition of social context, and simultaneous information processing (Figs 2.6, and 2.7).

2.5 Strengths and limitations of the study

Some limitations of the current study need to be taken into consideration. First, the small cohort of subjects, the high variability between individuals, and the large number of comparisons were overcome using a new two-step methodology that exploits the data structure and information of positive dependence to increase the power of our testing. Second, DTI was chosen instead of other dMRI acquisition schemes (HARDI or DSI) because subjects were young children requiring shorter acquisition time. Third, DTI reconstruction and tractography are sensitive to motion artefacts and both present limitations for reconstruction of complex fiber configurations, like crossing-fibers or kissing-fibers. A threshold on the density values of each bundle (the mean FA value) was used to minimize possible artefacts due to the acquisition and tractography noise. In that way, we reduced the number of residual connection values. Validation of the tractography method and the construction of connectomes are not discussed here as both aspects are extensively discussed elsewhere (Cammoun *et al.*, 2012; Hagmann *et al.*, 2007). Given the relatively small local cohort of extreme premature infants, the linear regression model testing the link between clinical risk factors and cognitive and behavioral measures has the inherent risk of *Type I* and *Type II* errors. Nevertheless, our results concur with published data from larger cohorts. Although connectomics still present technical challenges, they remain an ideal complementary tool to assess structural co-variance between brain regions on a global brain network scale (Alexander-Bloch *et al.*, 2013).

2.6 Conclusions

The whole-brain connectome analysis presented here allowed us to comprehensively study both long-ranging and short-ranging connectivity in preterm school-age children. The results suggest that EP and IUGR have altered SC of CBTCL connections that start their maturation early in development. SC alterations of the orbitofrontal cortex circuitry (responsible for reward learning, reality check, and socio-emotional processing) were evidenced by the whole-brain connectome approach. Specific short associational cortico-cortical connections, developing later and most likely influenced by environmental sensory inputs, showed both diminished and increased strength of connectivity between areas known to play an important role in language, problem solving, and social behavior. The strength of altered connections was associated with their socio-cognitive performance. In conclusion, the whole-brain connectivity analysis provides a link between early life events (extreme prematurity and IUGR), circuitry development, and specific socio-cognitive disabilities.

Nevertheless, and although a clear evidence of the existence of structural alterations, the resulting brain organization is far from presenting a complete random organization. Brain plasticity seems to play an important role in reorganizing brain systems while functionally overcoming some of these "deviations" from normal development. For a better understanding of such mechanisms, in the next chapter we characterize the topological role of the main brain cores and evaluate how their impairment may impact the overall brain system.

3

Brain network characterization of high-risk preterm-born school-age children

3.1 Context and background

In the previous chapter, Chapter 2, we have identified how extreme prematurity and prenatal growth restriction affects structural connectivity, especially in the cortico-cortical-basal-thalamocortical stream. The correlation of these alterations with some neurodevelopmental impairment seen at school-age proves that, although preterm's brain seems to reorganize to overcome some of the structural deficits, some of those remain in early childhood. The question that arise is whether this *brain reorganization* differs from the normal brain development or if the brain remains intrinsically the same, albeit some structural alteration. In other words, are the organizational principles of brain networks altered after EP and IUGR?

Brain connectomes can be seen as a network (equivalently, a graph), representing pairwise relations between interregional ensembles of neuronal elements (nodes), where the links represent anatomical connections formed by white-matter axonal paths (Bullmore & Bassett, 2011; Meskaldji *et al.*, 2013). This network model allows looking at the brain as an integrative complex system. From this point of view, the human brain network can be considered to be small-world. It is organized according to a hierarchical modular architecture, composed by communities of nodes highly interconnected between them, but sparsely connected with other modules (Bullmore & Sporns, 2009). This modular structure of brain networks is thought to be a crucial characteristic in terms of brain evolution and development (Meunier *et al.*, 2009) . Under this network prespective, network-based studies have found decreased global efficiency and nodal strength in IUGR and EP children, associated with abnormal scores in neurodevelopmental and socio-cognitive performance (Ball *et al.*, 2014).

In this context, connectomics has been used in pediatric populations to study brain development beginning at its early stages and continuing through adolescence (Pannek *et al.*, 2014; Tymofiyeva *et al.*, 2014). Batallé and colleagues (Batalle *et al.*, 2012) used diffusion-MR based network analysis to describe quantitative differences in global brain connectivity in IUGR one-year-old children and associated these differences with impairments in neurodevelopmental outcome at two years of age. Long-term brain organization following EP and IUGR, and its relation with higher cognitive skills and social cognition at 6 years of age has been further assessed by means of connectomics (Fischi-Gómez *et al.*, 2014).

A recent study demonstrates that even early in development, the human brain already exhibits an adult-like structural organization, showing both small-world characteristics (Ratnarajah *et al.*, 2013) and rich-club organization (Ball *et al.*, 2012). At school age, longer gestational age has been associated with improved topological organization (Kim *et al.*, 2014). Indeed, newborns demonstrate already a modular brain network architecture, even though such an organization is subject to substantial changes across development. Particularly, during development brain communities' topology would move from local subnetworks partially overlapping with brain lobes, to more spatially distributed circuits (Duerden *et al.*, 2013). A decrease in modularity and an increase in the number of modules during development from birth to pre-adolescence age have as well been highlighted (Stam *et al.*, 2013). These processes might be associated with pruning of short-range (intra-modular) connections, and strengthening of long-range associative tracts (inter-modular links) during development. One might expect that the combination of both EP and IUGR represent a double risk, and children born preterm with additional IUGR will show the combination of both factors in their neurodevelopmental outcome and brain structures. Nevertheless, little is know about the brain structural alterations and neurological outcome of children born very preterm with additional IUGR, though some studies conclude that the effect of extreme prematurity seem to prevail over the effect of fetal growth restriction (Marlow *et al.*, 2007). However, the effect of IUGR in brain structures and neurological outcome is visible in children born at GA > 28 weeks (Guellec *et al.*, 2011). The question that arises is, then, what are the structural changes that lead to this different impairment, which seems to be clearly dependent on the timing of the "insult". Since the development of functional connections is clearly dependent on the establishment of cerebral fiber pathways, their maturation and myelination (Smyser *et al.*, 2010; Supekar & Others, 2010), assessing the development of WM fibers underlying the complex brain connectivity becomes a key point to understand the developmental origin of childhood and adult brain disorders. Indeed, characterizing brain communities *fingerprint* (i.e. a normative pattern of brain network structure) in normal brain development, and finding alterations due to risk factors such as extreme prematurity and/or intrauterine growth restriction, can offer insight into the developmental origin of childhood and adult brain disorders.

In this chapter, network analysis is used to characterize the structural brain networks of children born extreme premature (with or without additional growth restriction) and children born moderate preterm with IUGR, relating brain connectivity alterations with cognitive and behavioral performance at school age. First, the modular topology of structural brain networks of these high-risk children is assessed and the similarity of their brain communities' structure is compared using information theory derived metrics. Their brain network substrate is then analysed by means of network organizational features and measures of network integration and segregation.

3.2 Material and Methods

3.2.1 Subjects

In this chapter, 50 prematurely born children at 6 years of age were considered (extracted from the dataset in 2.2.1). In order to study the effects of GA and BW separately and to determine if the combination of both birth conditions implies the addition of brain alteration due to EP and prenatal growth restriction, children were pooled in 4 different groups: (i) children born moderately preterm with normal growth (controls), (ii), children born at GA < 28 weeks (extreme premature, EP), (iii) children born moderately preterm with additional IUGR (IUGR only, IO) and (iv) children born at GA < 28 weeks with additional IUGR (IE) (see table 3.1).

Sample characteristics	CTL n=8	EP n=22	IUGR only (IO) n=11	IUGR + EP (IE) n=7
Gender (male/female)	3/5	9/13	5/6	7/0
GA (weeks)	32(2.5)	26.7(1)	32.5(1.5)	26.7(0.8)
BW (g)	1652.5(402.4)	960.9(193.5)	1181.8(260.5)	657(117.3)
BW z-score	−0.3(0.8)	0.3(1)	−2.1(0.4)	−1.5(0.7)

Table 3.1: Sample characteristics of the study participants according to gestational age (GA) and presence of intrauterine growth restriction (IUGR). Values are presented as $mean \pm std$. Cases with severe neurological impairment were not included in the study.

None of the children had any sign of prematurity-associated brain lesions on MRI at term equivalent age, as assessed by preterm brain injury scores (Woodward *et al.*, 2006). At 6 years of age, their MRI scans were read as normal by experiences neuroradiologists. All of the recruited children were free from medication and from psychiatric ir neurological disease. Parental socio-economic status (SES) and maternal education was also recorded and assessed using the Largo scale (Largo *et al.*, 1989).

3.2.2 Neurodevelopmental assessment

Children's cognitive assessment was carried out using the French version of the Kauffman Assessment Battery for Children (KABC) (Kaufmann & Kaufmann, 1983). More specifically, children were mainly tested for the overall cognitive outcome using the sequential and simultaneous KABC score and the composite KABC score. The sequential processing scale primarily measures short-term memory and consists of subsets that measure problem-solving skills where the emphasis is on following a sequence order. The simultaneous processing scale examines problem-solving skills that involve several processes at once. The sequential and simultaneous scales are combined to comprise the composite score. This composite measures intelligence on the KABC and concentrates on the child's ability to solve unfamiliar problems simultaneously and sequentially. The simultaneous processing scale has a greater impact on the mental processing composite score than do the sequential processing scales. The mental processing composite score is considered the global estimate of a child's level of intellectual functioning (Sattler, 1992) (see Appendix D for further information about the cognitive scores).

3.2.3 Brain network construction: Defining node and edges weights

Brain networks can help to understand the large-scale structural topology of brain connectivity (Bullmore & Sporns, 2009). They can be analyzed using graph theory measures, characterizing network structure (topology) and function, and measuring changes related to the refinement in specific metrics of networks topology. Global description of the network includes measures of topological organization, integration and segregation.

As in Chapter 2, the extraction of the whole brain structural connectivity matrices (connectomes) for each subject was performed using the Connectome Mapping Toolkit, (www.cmtk.org, (Daducci *et al.*, 2012)) (see Appendix A). For each subject, the brain network nodes were directly defined as the cortical ROI centroids. Edge weights were characterized as the structural connectivity (SC) between each pair of cortical regions, again as in the previous chapter.

3.2.4 Network features

3.2.4.1 Organizational measures

Small-world and rich-club attributes

The main organizational principles of the brain proved to be small-world (i.e. characterized by the presence of abundant clustering of connections combined with short average distances between neuronal elements. It is organized according to a hierarchical modular architecture, composed by communities of nodes highly interconnected between them (forming a "rich-club" (Ball *et al.*, 2014)), but sparsely connected with other modules (Bullmore & Sporns, 2009)). This modular structure of the brain networks is thought to be a crucial characteristic in terms of brain evolution and development (Meunier *et al.*, 2009). In this study, we computed the normalized rich-club coefficients $\phi_{norm}(k)$ for several degree values k as in (van den Heuvel & Sporns, 2011). These coefficients describe the exceeding level of connectedness between high degree nodes compared to a randomized reference network. Small-world indices were computed with respect to a random equivalent network with the same degree distribution of each subject (see (Bullmore & Bassett, 2011) for a comprehensive description of these measures).

Brain network modular structure

In order to disentangle the existence of a network communities structure, for each brain network we computed its optimal modular decomposition, defined as the complete subdivision of the network into non-overlapping modules. Since it has become clearer that complex systems share non-random topological properties (Vértes & Bullmore, 2014), a large variety of approaches for community detection in graphs has been proposed, such as divisive or agglomerative algorithms, optimization strategies or methods based on graph dynamical processes. However, in te context of brain network analysis, the modularity index is Q is the preferred choice, as it is an effective of network decomposability yielding high quality partitions.

The modularity index, Q was originally introduce by Newman (Newman, 2006) and it has as been extensively used to compare the quality of different partitioning algorithms. It is defined as the number of edges connecting nodes belonging to the same community, minus the expected value of interconnecting edges in absence of any community structure, i.e. in an equivalent random graph. Formally, Q cab be expressed as:

$$Q = \frac{1}{2m} \sum_{ij} (A_{ij} - P_{ij}) \delta(C_i, C_j) \tag{3.1}$$

with A the binary or weighted adjacency matrix of network G (A_{ij} being an element of the A), m the total number of edges in the graph, and the δ function expressing the co-occurrence of two nodes (i, j) in the same cluster, i.e.,

$$P_{ij} = \frac{k_i k_j}{2m} \delta(C_i, C_j) = 1 iff C_i \equiv C_j \tag{3.2}$$

P_{ij} expresses the expected number of edges between nodes i and j in an equivalent random network [1]. This probability of connection between two nodes is proportional to the product of their

---

[1] A random equivalent network is a random network equal to our non random graph G in degree sequence.

degree k:

Thus, the modularity can be written as:

$$Q = \frac{1}{2m}\sum_{ij}(A_{ij} - \frac{k_i k_j}{2m})\delta(C_i, C_j) \tag{3.3}$$

Optimal modular decomposition of brain networks

In this work, the optimal modular decomposition was determined by using the Brain Connectivity Toolbox (BCT) https://sites.google.com/site/bctnet/) by selecting the partition with higher modularity index (Q) from 100 runs of the Louvain algorithm (Blondel *et al.*, 2008). Besides its computation efficiency, the choice of the Louvain algorithm was done considering that it incorporates a notion of modular hierarchical structure that is well suited to brain analysis questions. The algorithm is composed of two steps iteratively repeated until convergence to a modularity maximum. First, each node is placed in a separate module, and all possible node moves between modules are evaluated in terms of modularity gain, i.e. an increasing of the modularity index Q (step 1). When no individual move can further improve the Q value, nodes belonging to the same community are agglomerated (step 2) in order to form new 'super-nodes'. Step one (moves evaluation) is repeated on the new 'super-nodes' network. The two steps are repeated until convergence.

Following (Rubinov & Sporns, 2010a), the partitions obtained using the Louvain algorithm were compared using the variation of information index (VI) and the mutual information index (MI). The normalized variation of information *VIn* (Meilă, 2007) was used as a metric of distance between partitions C^i in the clustering space. The normalized mutual information *MIn* (Danon *et al.*, 2005) was used to measure the amount of information shared by different partitions C^i. $VIn = 0$ and $MIn = 1$ express perfect agreement between partitions. *VIn* and *MIn* quantified the intra-subject and inter-subject variability of the modular decomposition obtained with the Louvain algorithm, when compared to the rest of the cohort. In other words, as we can assume that a partition effectively represents a groups if the MIn values are high and, as the same time, VIn values are small, these two measures were used to quantify the consistency of the modular brain architecture for the subjects belonging to the same group, and to study the variability of the brain modular decomposition of EP, IO and IE subjects when compared to the rest of the cohort.

Group-wise representative brain network modular decomposition

Finally, in order to represent the modular decomposition of each group, the "representative" brain network partition, or *modular fingerprint*, for each group by means of *consensus clustering*, *CC* (Lancichinetti & Fortunato, 2012). We set the threshold value of the consensus clustering matrix to $\tau = 0.3$ and use $n = 100$ iterations. The consensus clustering algorithm is an approach that delivers an agreement partition across multiple runs of a given clustering algorithm. We used the Brain Connectivity Toolbox (Rubinov & Sporns, 2010b) for the Louvain community detection and for the partitions' distance computation (Appendix E give a comprehensive explanation of community detections and metrics. It has been extracted from the PhD dissertation of Alessandra Griffa (Griffa, 2015) with personal permission).

3.2.4.2 Integration and segregation measures

The overall networks connectivity and topology was examined by commonly used integration and segregation measures. From the structural connectomes, we computed 3 global (average shortest path length, global efficiency and transitivity), and 6 average nodal (average node degree, efficiency, strength, clustering coefficient (clustering index), betweenness centrality and eccentricity) network measures. The final goal was to characterize network structure and function by measuring changes related to the refinement in specific metrics of networks topology (see (Rubinov & Sporns, 2011b) for definitions and detailed information of the network measures).

3.2.5 Statistical analysis

Statistical case-control and case-case comparisons between groups were performed for (i) cognitive scores and (ii) network measures using a two-sided t-test.

The optimal modular decomposition of each individual brain network was compared to the rest of the cohort in terms of MI and VI indices. We tested three different settings: (i) intra-group comparison, where each subject's modular decomposition was compared to the rest of the subjects belonging to the same group, (ii) case-control comparisons, where each of the EP, IO and IE subjects were compared to the control subjects, and (iii) case-case comparison, were EP, IO and IE subjects were compared between them.

3.3 Results

3.3.1 Cognitive group differences

Table 3.2 shows the mean KABC scores for all groups, together with their standard deviation. In all KABC scales, higher scores are related to higher cognitive skills. Whilst the mental processing composite score, considered as the globale stimate of child's level of intellectual functioning, did not show any significant diference for any case compared to controls, all case groups (EP, IO and IE) showed significantly reduced KAC-simultaneous score, with $p = 0.0051$ (EP), $p = 0.03$ (IO) and $p = 0.0337$ (IE). No other differences were found. No significant differences were found for the case-case comparisons (EP vs. IO, EP vs. IE and IO vs. IE).

Cognitive scores	CTRL	EP	IO	IE
KABC-sequential	99.37 ± 9.59	94.5 ± 15.63	100.81 ± 16.43	95.18 ± 13.21
KABC-simultaneous	109 ± 7.25	96.90 ± 9.99(∗)	101.45 ± 8.86(∗)	95.54 ± 15.87(∗)
KABC-composite	0.69 ± 0.01	0.70 ± 0.01	0.70 ± 0.02	0.70 ± 0.01

Table 3.2: Average and standard deviation (mean ± std) for the neurocognitive score for all groups under analysis

3.3.2 Network features: group differences

3.3.2.1 Organizational measures

Small-world and rich-club attributes

For all groups, small-world characteristics of the networks were detected, with no significant differences. In the same line, for all subjects the presence of a rich-club of interconnected hubs cortical hubs was found. Again, the comparison of rich club coefficients did not show conclusive differences among groups.

Brain network modular structure

All subjects presented a modular architecture in their brain network, with overall comparable mena number of modules (or clusters) and mean modularity index (Q). Interestingly, although he comparison showed no significance, EP children also presented, in average, the smallest number of brain network modules (see Table 3.3).

Network attributes	CTRL	EP	IO	IE
Number of modules	10.12 ± 0.64	9.35 ± 0.71	10.82 ± 0.75	9.7 ± 0.67495
Modularity index (Q)	0.69 ± 0.01	0.70 ± 0.01	0.70 ± 0.02	0.70 ± 0.01

Table 3.3: Average and standard deviation of the number of modules and modularity index Q (mean ± std) from subject-wise brain network modular decomposition, for the four groups

The resulting network decompositions were compared between subjects using the MIn and VIn indices. Figure 3.1 reports these for the comparison between each pair of subject decompositions. Each row of the matrix represents the MIn (resp. VIn) values of one subject's network decomposition with respect to the rest of the cohort. For visualization purposes, each matrix is divided in different block by white lines. The diagonal blocks represent the resulting MIn and VIn indices within the same group of subjects (intra-group comparison), while the off-diagonal blocks characterize these values for the inter-group comparison. High MIn values together with low VIn values in the diagonal blocks indicate similar levels of modular topology for subjects belonging to the same group. In this case, no statistical differences were found (repeated two-sample Wilcoxon ranksum test). On the contrary, MIn and VIn distributions for subjects belonging to different groups (off-diagonal blocks) appeared significantly different in all cases ($p - value < 0.05$, FDR corrected), talking in favour of a group-specific different modular brain network structure. It bears noting that EP and IE subjects showed a relatively high similarity, which reflects a close modular structure.

Tables 3.4, 3.5 and 3.6 report the MIn and VIn mean and standard deviation values for both intra-group and inter-group comparison. Statistically significant differences are marked with ($*$). When comparing subjects within the same group, the relatively high MIn values together with the low VIn values prove the similar overall network structure of subjects beloging to the same group, with no significant differences (see Table 3.4).

As seen in Table 3.5, the modular structure of the brain network for EP, IO and IE children appeared significantly different when compared to controls.

Table 3.6 evidences how EP and IE subjects have a close brain network modular structure. Even if in all cases the resulting network decomposition was significantly different, the higher MIn values together with the lower VIn values talk in favor of a relatively similar modular structure for these two group of subjects.

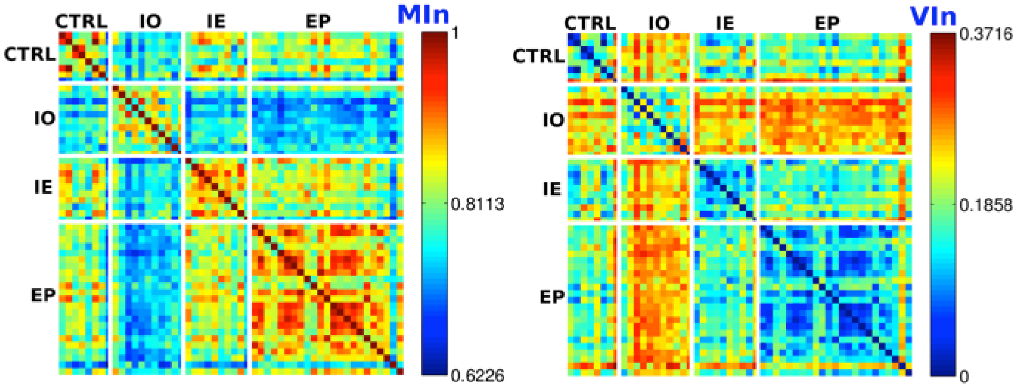

Figure 3.1: Matrices representing respectively the normalized (a) $MI(Min)$ and (b) $VI(Vin)$ values between each pair of subject optimal modular decompositions. White lines highlight the different intra-group (diagonal) and inter-group (off diagonal) blocks.

Groups	MIn (mean ± std)	VIn (mean ± std)
CTRL	0.81613 ± 0.081501	0.18418 ± 0.081337
EP	0.86198 ± 0.056419	0.13186 ± 0.054544
IO	0.82578 ± 0.050917	0.1818 ± 0.052754
IE	0.85195 ± 0.049577	0.14386 ± 0.047798

Table 3.4: Average and standard deviation intra-group and inter-group MIn and VIn values for the intra-group optimal modular decomposition comparison. For each subject, its modular brain network decomposition was compared to the rest of the subjects in the same group by means of MIn and VIn indices. These indices were compared statistically using a Wilcoxon ranksum test. No differences were found.

Groups	MIn (mean ± std)	VIn (mean ± std)
CTL vs EP	0.79988 ± 0.056778(∗)	0.1955 ± 0.055527(∗)
CTL vs IO	0.76813 ± 0.04112(∗)	0.23726 ± 0.042292(∗)
CTL vs IE	0.81224 ± 0.061895(∗)	0.1955 ± 0.055527(∗)

Table 3.5: Average and standard deviation intra-group and inter-group MIn and VIn values for the case-control optimal brain decomposition comparison. For each EP, IO and IE subject, its modular brain network decomposition was compared to the control subjects by means of MIn and VIn indices. These indices were compared statistically using a Wilcoxon ranksum test. Both indices were statistically different in this cases.

Groups	MIn (mean ± std)	VIn (mean ± std)
EP vs IO	0.74954 ± 0.038688	0.2502 ± 0.038781
EP vs IE	0.81904 ± 0.048115	0.17442 ± 0.047043
IO vs IE	0.76368 ± 0.04176	0.23821 ± 0.040862

Table 3.6: Average and standard deviation intra-group and inter-group MIn and VIn values for the case-control optimal brain decomposition comparison. For each EP, IO and IE subject, its modular brain network decomposition was compared to the rest of subjects subjects by means of MIn and VIn indices. These indices were compared statistically using a Wilcoxon ranksum test. Both indices were statistically different in this cases.

Group-wise representative brain network modular decomposition

Group-wise representative partitions are shown in figure 3.2. The four consensus clustering (CC) partitions counted 11 clusters for CTRL and IO subjects, 9 for EP and 10 cluster for IE subjects. This figure displays how nodes cluster together for each group representative partition after running the consensus clustering algorithm. The visual inspection of the CC configurations corroborates the numerical results, and indicates that the main differences in modular structure among groups are found in the frontal regions. Indeed, while the temporal, parietal and occipital regions nodes tend to cluster in a similar way, the frontal region shows the higher dissimilarities between groups. More specifically, for control and IO subjects the anterior cingulate regions cluster together with the orbito-frontal regions, while the basal ganglia structures are roughly grouped together in a different module. On the contrary, for the EP and IE cases, both the anterior cingulate regions and the basal ganglia structures cluster with the frontal and central regions in a single module.

These results allows us to hypothesize that IE subjects are closer in modular brain structure to EP subjects, while IO subjects appear to have the most different with on average a higher number of modules.

3.3.2.2 Integration and segregation measures

Case-control differences

As seen in Table 3.8, when compared to controls, EP children showed increased network averaged path length ($p = 0.0025$), and decreased global network efficiency ($p = 0.00079$) and averaged node strength ($p = 0.0051$). For IO subjects, significant decreased global network efficiency ($p = 0.0089$) and reduced averaged node strength ($p = 0.017$) was found. IE children showed, as EP children, increased network averaged path length ($p = 0.034$), and decreased global network efficiency ($p = 0.0033$) and averaged node strength ($p = 0.015$).

Case-case differences

IO showed smaller averaged node strength ($p = 0.056$) when compared to EP, while IE children show (compared to EP) a statistically significant decrease in global network efficiency ($p = 032$), global network transitivity ($p = 0.007$), and averaged node strength ($p = 0.01$), efficiency ($p = 0.0043$) and clustering index ($p = 0.014$). When comparing IO and IE subjects,

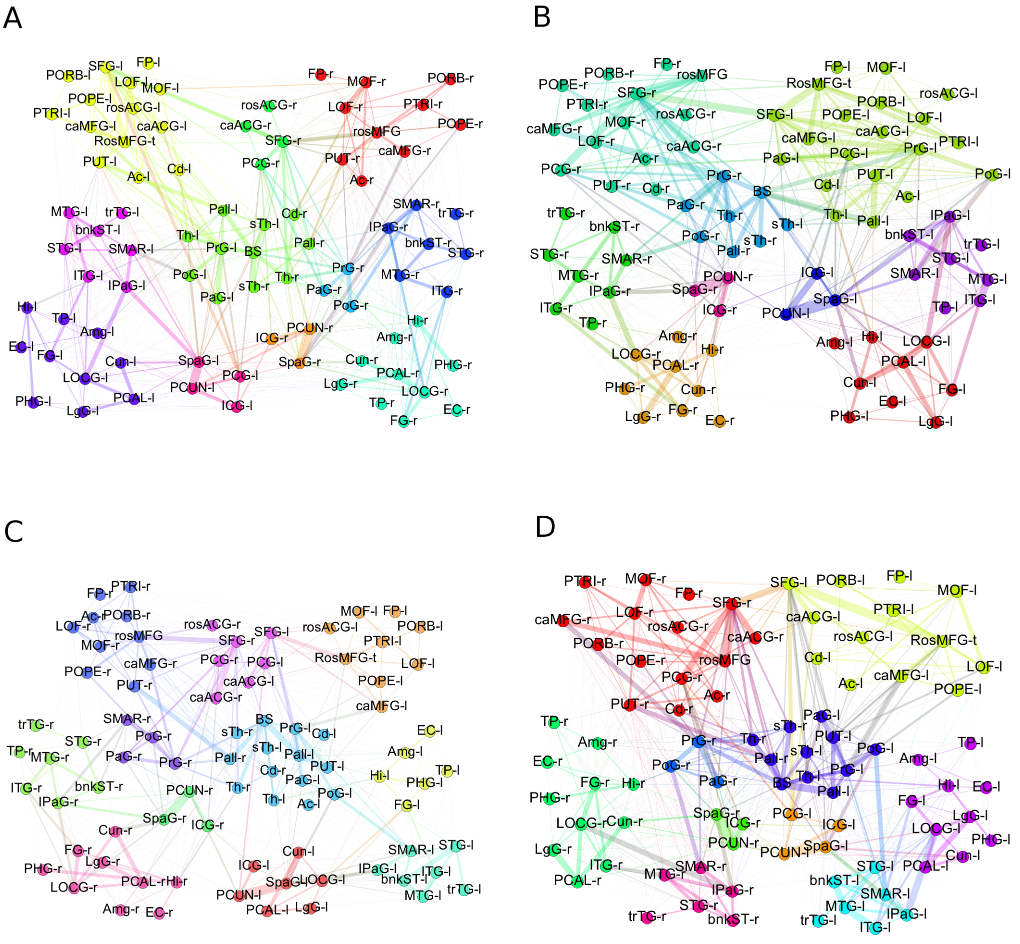

Figure 3.2: Modules for the representative brain network partitions for each group of subjects obtained using the consensus cluster algorithm. (A) CTRL, (B) EP,)C) IO and (D) IE. Nodes belonging to the same cluster are colored with the same color. The main differences among groups are located in the frontal regions, with the anterior cingulate regions clustering together with the frontal and orbito-frontal regions EP and IE subjects and clustering in an different module for the CTRL and IO subjects. Node lsit of abbreviations are found in Table 3.7. r- stands for right hemisphere and l- stands for left hemisphere.

Label	Anatomical region	Label	Anatomical region
LOF	Lateral orbito frontal gyrus	PCAL	Pericalcarine cortex
PORB	Pars orbitalis, orbital part of the inferior frontal gyrus	LOCG	Lateral occipital gyrus
FP	Frontal pole	LgG	Lingual gyrus
MOF	Medial orbito frontal gyrus	FG	Fusiform gyrus
PTRI	Pars triangularis, triangular part of the inferior frontal gyrus	PHG	Parahippocampal gyrus
POPE	Pars opercularis, inferior part of the inferior frontal gyrus	EC	Enthornial cortex
rosMFG	Middle frontal gyrus, rostral	TP	Temporal pole
SFG	Superior frontal gyrus	ITG	Inferior temporal gyrus
caMFG	Middle frontal gyrus, caudal	MTG	Middle temporal gyrus
PrG	Precental gyrus	bnkST	Superior temporal sulcus, banks region
PaG	Paracentral lobule	STG	Superior temporal gyrus
rosACG	Anterior cingulate gyrus, rostral	trTG	Transverse temporal gyrus
caACG	Anterior cingulate gyrus, caudal	Th	Thalamus
PCG	Posterior cingulate gyrus	Cd	Caudate
ICG	isthmus cingulate gyrus	PUT	Putamen
PoG	Postcentral gyrus	Pall	Pallidum
SMAR	Supramarginal gyurs, inferior part of the parietal lobule	Ac	Accumbens
SpaG	Superior parietal gyrus	sTh	Sub-thalamus
IPaG	Inferior parietal gyrus	Hi	Hippocampus
PCUN	Precuneus	Amg	Amigdala
Cun	Cuneus	BS	Brain stem

Table 3.7: List of abbreviation for cortical and subcortical regions of interest (rom freesurfer parcellation.

Groups	$geff$	$trans$	$lambda$	$neff$	$nstr$	CI
EP vs CTRL	$\downarrow$ ($p = 0.00079$)		$\uparrow$ ($p = 0.0025$)		$\downarrow$ ($p = 0.0051$)	
IO vs CTRL	$\downarrow$ ($p = 0.0089$)				$\downarrow$ ($p = 0.017$)	
IE vs CTRL	$\downarrow$ ($p = 0.0033$)		$\uparrow$ ($p = 0.034$)		$\downarrow$ ($p = 0.015$)	

Table 3.8: Network segregation and integration measures differences in the case-control comparison for all subjects under study: $geff$, global efficiency; $trans$: transitivity; $lambda$: averaged shortest path length; $neff$: averaged nodal efficiency; $nstr$: averaged nodal strength; CI: clustering index; Arrows indicate the sense of the difference ($\downarrow$ indicates decreased values and $\uparrow$ increased). The p-value of the comparison in shown in parentheses. EP and IO and EP subjects have similar network changes when compared to controls , except for the averaged path length that is increased in EP subjects. This is not the case for IO subjects.

differences were found in global network efficiency (decreased for IE subjects (p = 0.046)) and in averaged node strength, increased in IE children (p = 0.018). These results are summarized in Table 3.9.

Groups	$geff$	$trans$	$lambda$	$neff$	$nstr$	CI
IO vs EP					↓ (p = 0.056)	
IE vs EP	↓ (p = 0.032)	↓ (p = 0.007)		↓ (p = 0.0043)	↓ (p = 0.01)	↓ (p = 0.014)
IE vs IO	↓ (p = 0.046)				↓ (p = 0.018)	

Table 3.9: Network segregation and integration measures differences in the case-control comparison for all subjects under study: $geff$, global efficiency; $trans$: transitivity; $lambda$: averaged shortest path length; $neff$: averaged nodal efficiency; $nstr$: averaged nodal strength; CI: clustering index; Arrows indicate the sense of the difference (↓ indicates decreased values and ↑ increased). The p-value of the comparison in shown in parentheses.

In the analysis, the cognitive and neurobehavioral scores that mainly predict GA were SRT-Q1, SDQ-hyperactivity and KABC -SP, -SIP and -MCP scores though without significance. Similar results were found when modelling BW with the clinical scores, though this time they show significance. Here, the selected model was build using SRT-Q1 (p = 0.00722), SDQ-hyperactivity (p = 0.0438) and KABC -SIP (p = 0.00159) and -MCP scores (no significance was found for MCP).

On the contrary, several network features showed correlation with GA and BW. The regression model for GA was composed by the global network efficiency ($p = 8.610^{-11}$), global network transitivity ($p > 0.05$) and averaged node strength ($p = 6.410^{-10}$), efficiency (p = 0.0061) and clustering index (p = 0.0036). BW was mainly predicted by network global efficiency ($p = 4.2610^{-5}$), network global transitivity (p = 0.0224) and averaged node strength (p = 0.00423) (see table 3.10).

Scores	G_{eff}	$Trans$	n_{eff}	n_{str}	CI
GA	$8.6410^{-11}*$	$p > 0.05$	0.0061$*$	$6.410^{-10}*$	0.0036$*$
BW	$4.2610^{-5}*$	0.0225$*$		0.0043$*$	

Table 3.10: In each column, predictors used in the linear regression. In each row, GA and BW. Selected stepwise regression predictors for each score, with the corresponding $p - value$ (marked with $*$ when significant). Global network features: G_{eff}: global network efficiency; $Trans$: global network transitivity. Local network features: n_{eff}: averaged node efficiency; n_{str}: averaged node strength and CI: clustering index.

3.4 Discussion

This study complements prior studies on preterm children at school age in terms of brain network organization, integration and segregation. It detects alterations in brain topology and organization after early exposure to extra-uterine enviroonment or antenatal adverse conditions such as IUGR. It provides evidence for specific developmental period-linked vulnerability of brain network formation.

Lacichinetti et al. write: “networks system typically display a modular organization, reflecting the existence of special affinities among vertices in the same module, which may be a consequence of their having similar features or the same roles in the network” (Lancichinetti & Fortunato, 2012). In this study, the decomposition of each individual brain networks in consistent modules enabled the comparison between groups using several measures of clustering similarity. As we can assume that one subject’s partition is similar to another if the mutual information index (MI) index between partitions is high and the variation of information index (VI) is small, our results suggest that the consensus clustering partitons presented here effectively represent the modular topology of each group. On the other hand, the significant differences found in both case-control and case-case comparisons (with lower MI indices and higher VI indices) show a group-specific different modular brain network structure. Despite having very similar modularity index, distances between partitions among groups remained substantial (Tables 3.5 and 3.6), talking in favour of a different global brain network organization. The visual inspection of group representative consensus clustering partitions (Figure 3.2), corroborates the analytical results, and allows to hypothesize that IE subjects are closer in brain modular structure to EP subjects. The most striking difference among groups is located in the frontal pole, in concordance with a recent study (Duerden *et al.*, 2013) where alterations in frontal lobe pathways were found for young children born preterm and negatively correlated with measures of intelligence. These results support also our prior study (Fischi-Gómez *et al.*, 2014), in which microstructural alterations in the prefrontal cortico-basal-thalomo-cortical loop (CBTCL) were present in EP and IUGR children.

Ball et al. demonstrated that a rich-club network of densely connected cortical hubs is established before the time of normal birth (Ball *et al.*, 2014)). In this context, all subjects under analysis showed an evident rich-club organization of their brain networks with no significant differences between groups. Nevertheless, our results provide evidence that structural connectivity and network topology appear altered after premature birth and/or IUGR, suggesting that altered fetal environment and nutrition and/or premature birth has an impact in the development of brain connectivity with a reduction in global network capacity. Although global brain organization remains intact, we show a significant reduction in global brain network efficiency and in averaged node strength, suggesting that both EP and IUGR are, by themselves, risk factors for structural connectivity development, which lead to limited communication efficiency between brain network nodes.

In (Fischi-Gómez *et al.*, 2014) the structural connectivity alterations after EP and IUGR were already assessed, showing that the regional microstructural alteration is similar in both cases with reduced connectivity in the prefrontal cortico-basal ganglia-thalamo-cortical loop. One could therefore hypothesize that the combination of IUGR and EP would result in an additive alteration of their brain network structural connectivity. Nevertheless, no clear evidence was found in that sense. Again, albeit IE subjects showed a different global community structure compared to IO, particularly in the frontal pole (see Figure 3.2), their representative network partition looks similar to the EP subjects one. These results may indicate that IE structural connectivity appears mainly affected by the effect of extreme prematurity. This outcome is in concordance with previous studies that conclude that the effect of extreme prematurity prevails over the effect of fetal growth restriction (Yanney & Marlow, 2004). On the other hand both, the microstructural alterations and the changes in global network characteristics are similarly affected in EP, IE and IO children when comparing to control children, which infers that there is a specific developmental window of vulnerability between 28 and 34 wks which leads to brain network abnormalities both by intrauterine insults (as in IUGR) as well as postnatal insults (as in EP). This would explain why the neurofunctional outcome is similarly affected in groups of babies born below 28 wks and IUGR children born above 28 weeks (Guellec *et al.*, 2011), so in the absence of EP.

Preterm birth and adverse fetal conditions are associated not only with altered brain development but also with cognitive and behavioral deficits. Although the direct link between connectivity disruptions and neurocognitive impairment is far from having a clinical consensus, there is increasing evidence that regional connectivity abnormalities relate to specific neurocognitive deficits (Batalle *et al.*, 2012; Fischi-Gómez *et al.*, 2014). For instance, the fronto-partietal connectivity is known as being heavily implicated in effective network communication and function (Ball *et al.*, 2014), and alterations in the frontal networks have been directly correlated with cognitive impairment (Fischi-Gómez *et al.*, 2014)).

Our earlier data combined with the new global network efficiency measures suggest that alterations in the structural brain substrate due to EP and IUGR are important factors that may affect neurobehavioral and cognitive performance. Functional integration is considered as the ability of the brain to rapidly combine specialized information from distributed brain regions. Higher values of global efficiency are thought to contribute to a better ability to transfer information between brain regions. Segregation in the brain is seen as the ability for specialized processing to occur within densely interconnected groups of brain regions. Thus, taking all together, our results suggest that, while cognitive tasks impairments relate to alteration in brain network integration, behavior and hyperactivity are linked not only on how rapidly information from different regions is combined, but also how the information is processed simultaneously in specialized regions.

DTI networks gradually mature from local, proximity-based connectivity patterns designed to support primary functions to a more distributed, integrative topology thought to be favourable for supporting higher cognitive functioning (Vértes & Bullmore, 2014). Particularly, during development brain communities' topology would move from local sub-networks partially overlapping with brain lobes, to more spatially distribute circuits (Collin & van den Heuvel, 2013). In a normal basis, the macro-structural network architecture required for normal brain function is already present at birth, which is not apparently if this global network development is disrupted by external factors. Indeed, from (Ball *et al.*, 2014) we know that “during the third trimester, the number of connections between rich-club regions and the rest of the cortex increases significantly".

The remodelling of anatomical networks over the course of postnatal development is thought to predominantly reflect the fact that myelination and maturation occur asynchronously across various axonal tracts (Vértes & Bullmore, 2014). From birth to pre-adolescence age the brain networks organization shows a decrease of the modularity index and an increase of the mean number of modules. These processes are suggested to be associated with pruning of short-range (intra-modular) connections, and strengthening of long-range associative tracts (inter-modular links) during development.

Both EP and IO subjects though show decreased average node degree and node strength, with IO having the most pronounced node strength reduction compared to controls. In other words, both groups show similar altered network integration and segregation patterns. This would indicate that network integration might be particularly vulnerable to insults occurring between 26 and 32 to 34 weeks independently from intra-uterine (IUGR) or extra-uterine conditions (EP) and would confer with the similar risk in cognitive deficits in EP and moderately preterm IUGR infants (Guellec *et al.*, 2011).

3.5 Conclusions

The study presented in this chapter was intended to complement the results obtained in Chapter 2. As seen there, extreme prematurity and prenatal growth restriction affects structural connectivity mainly in the sub-networks related to high cognitive skills and executive functions. Yet, it is not clear if in such cases preterm brains reorganize to overcome some of the structural deficits and if they do, to what extent. Indeed, the final goal of this analysis was to characterize network structure and function by measuring changes related to the refinement in specific metrics of networks topology (see (Rubinov & Sporns, 2011b) for definitions and detailed information of the network measures).

The results presented in this chapter show that, as for the case of the structural connectivity, the brain network topology appears to be altered after premature birth and/or IUGR, suggesting that altered fetal nutrition and/or premature birth has an impact in the macrostructural development of brain connectivity with a reduction in network capacity. Yet, the overall network measures show correlation with cognitive and behavioral skills that may explain long-term difficulties in learning and social behavior of these children. It bears noting though, that the combination of both factors do not lead to a worse outcome than considering the two risk factors independently. Our findings are in concordance with the findings of Yanney and Marlow (Yanney & Marlow, 2004) and Guellec et al. (Guellec *et al.*, 2011), where prenatal growth restriction added to extreme prematurity did not increase the risk of neurological outcome as the effects of prematurity seem to prevail over IUGR.

In conclusion we suggest that this analysis might be valuable in defining the structural correlates of the cognitive outcome following the premature birth with or without IUGR, paving the path to define quantitative and qualitative non-invasive MRI biomarkers related to cognitive outcome, seen as a result of underlying changes in prenatal histogenesis. Indeed, the identification of (possible) imaging biomarkers of the outcome in the developing brain becomes an interesting perspective for the study of long-term effects of prematurity.

The question that arises now is whether these alterations are already present at the moment of birth, and if they do, to which extent. Indeed, are they more important at birth than they are at childhood? Does the brain fully reorganize during early childhood so the alterations seen at age 6 are only a part of these earlier ones? From this perspective, being able to perform a similar analysis at an earlier time-point is certainly of great interest. Part II of this thesis dissertation is intended to set the technical bases needed to enable the fully automated analysis of brain connectivity in the newborn brain.

Part II

Mapping the newborn brain

Overview

In recent years an increasing number of connectivity studies in pediatric cohorts have intended to find structural correlates between the neurocognitive or behavioral impairments seen later in life in preterm born children (Dubois *et al.*, 2014; Kwon *et al.*, 2014; Pandit *et al.*, 2014; Pannek *et al.*, 2014). In such cases, at-risk populations – such as extremely premature infants or children born after placental insufficiency leading to prenatal growth restriction – are generally considered (Ball *et al.*, 2012, 2014; Batalle *et al.*, 2012; Fischi-Gómez *et al.*, 2014). Indeed, there is increasing evidence that deviations from normal connectome development are linked to neurodegenerative disorders. The moment in development when this "deviation" takes place has been associated with the pathophysiology of specific brain disorders, such as autism, schizophrenia and Alzheimer's disease (Collin & van den Heuvel, 2013). For that reason the so-called *growth connectomics* field has become very active in the recent years; specifically since the innovations in medical imaging and image analysis allowed to determine interregional brain connectome even in newborn populations. Nevertheless, the construction of the connectomes for newborn data is not free of challenges and generally raises a non-negligible number of problems and pitfalls that might alter the final results.

As seen in Part I of this manuscript, the pipeline for assembling the brain network is composed of several steps: cortical surface extraction, surface parcellation, identification of white matter tracts connecting individual parcellated nodes and connectivity estimation. For adult MR images, these procedures are mostly straightforward and included in several freely available packages, fully automatized (Cook *et al.*, 2006; Daducci *et al.*, 2012). Nevertheless, in case of newborn MR images we cannot directly apply those automatized methods. Moreover, each one of these individual steps represents a real challenge.

The major issue in adapting "adult procedures" to newborn data sets is that almost all processing algorithms (for segmentation/registration/cortical parcellation) are based on adult atlas and templates that differ from neonate brain structures. And even in the case where the processing algorithms do not rely on atlases, the poor image contrast of neonatal MR makes their uses limited. Thus, in order to map brain neuronal paths and to compare them between individuals, we first need a reliable *registration* between subjects and an accurate *cortical surface extraction* and *parcellation*. These steps implicitly mean that we first need an accurate brain tissue *segmentation* tool, especially for the cortical surface extraction.

Automatic tissue segmentation on neonatal brain MR images remains challenging because of the insufficient image quality due to the properties of developing tissues (Mewes *et al.*, 2006; Peterson *et al.*, 2000). In newborn infants, white matter undergoes myelination while the fibers are covered by myelin sheets. At birth, the brain stem and posterior limbs of the internal capsule are myelinated and have white-to-gray matter contrast similar to adults (white matter is brighter than gray matter in adult T1-weighted MR images). However, other regions such as the centrum semi-ovale are not myelinated and their image contrast is therefore inverted. As the child ages from birth to one year, myelination progresses through the anterior limbs of the internal capsule, the occipital radiations and, finally, to the frontal gray matter. Therefore, the MR relaxation times of these regions change with the newly myelinated fibers, changing the MR signal. By the age of 1.5 years, the MR image contrast is almost adult-like. This ongoing myelination process makes the appearance of developing brain hugely different from the homogeneous adult's tissue types (Bach-Cuadra *et al.*, 2009).

Manual segmentation of newborn brain images is tedious, time consuming and lacks reproducibility. This fact makes it highly desirable to have an automated procedure, especially when dealing with multiple subjects, as for clinical studies. Nevertheless, as Pastrawa et al. assessed in (Pastrawa *et al.*, 2005), automated segmentation methods valid for healthy adults fail in segmenting all the different structures apparent in newborn brain, particularly the unmyelinated white matter. Methods for newborn image segmentation can barely take advantage of templates or probability maps or atlases coming from adults. They will not match the newborn cerebral structure. In fact, for achieving good segmentation performance, the atlas should have similar anatomical structures with the to-be-segmented images (Aljabar *et al.*, 2009). On top of that, the use of pediatric atlases unavoidably introduces a bias of the results towards the population that was used to derive the atlases (Gui *et al.*, 2012).

Tissue segmentation is the first step to delineate the cortical regions of interest that will serve as nodes for the connectome. Yet, as we can see in Fig. 3.3, the process of parcellating the cortical surfaces comprises distinct tasks.

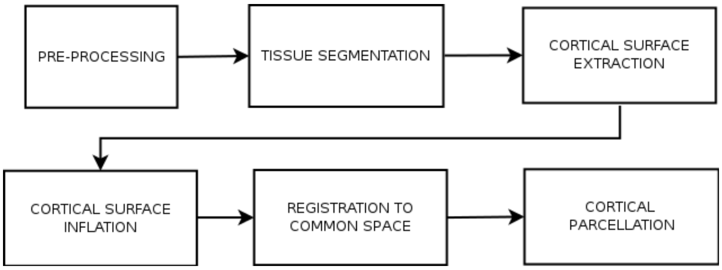

Figure 3.3: Block diagram showing the main processing steps to delineate cortical structures

It is clear that the resulting cortical delineations will largely rely in the accuracy of the segmentation. Indeed, a procedure that enforces topological constraints during the segmentation, should be preferable to avoid inaccuracies in the final reconstructed surfaces. If these topological constraints can not be enforced during the processing, the resulting segmentation can be directly corrected from the volumetric data. Yet, if none of these options are available, and one can only assume that the segmentation obtained is reliable to some extent, one can still attempt to enforce topological proprieties direct on the mesh representing the cortical surface obtained after the surface extraction step (again, see Fig.3.3). The methods presented in this Part II belong to this last case. Starting from a set of segmentation labels, we intend to obtain an anatomically and topologically correct mesh, representing the cortical surface of a newborn.

Part II of this thesis dissertation aims to develop methods to obtain a fully automated pipeline for the study of brain connectivity in newborn data not obtainable with methods developed for adult populations. At the beginning of each chapter we present an overview on the state-of-the art methods for surface reconstruction on one hand, and registration and cortical parcellation on the other. These specific introductions set the context and motivations leading to the methods developed in this thesis.

In Chapter 4 we present new methodology to repair cortical surfaces extracted directly from the segmented volumes. Though the initial surfaces appear topologically correct, geometrical inconsistencies such as sharp peaks (usually due to noise) cause the failure of any further processing. Those peaks are generally not detectable using common measures of surface characteristics like the Euler or Betty numbers, but create a real problem, for instance, for the registration task. In this work, we used curvature information for detecting these surface singularities and to remove them using their $i^{th} - ring$ information. The resulting oriented point-cloud is then reconstructed using a smooth approximation of the signed distance function to the surface, as in (Calakli & Taubin, 2011).

The validation of the resulting surfaces is done using topological and geometric measures borrowed from the computer vision field and mathematical theory of geometric meshes. Most importantly, the resulting meshes allowed further processing of the surfaces yielding a cortical parcellation of newborn cortical structures. It is in Chapter 5 where we present a fully automatic processing stream, where we are able to delineate the main regions of the cortical surface in the case of newborn MRI.

In Chapter 5, we develop and qualitatively validate a fully automated pipeline to register and parcellate the topologically and geometrically correct surfaces obtained in Chapter 4. Taking advantage of a longitudinal dataset in which subjects were scanned at the newborn period and at 6 years of age, we propose an automated newborn cortical surface delineation. Two different schemes are presented, based on the cortical folding patterns of the surfaces: (i) one-to-one and (ii) one-to-average matching. The resulting parcellated cortical regions are then compared to the ones obtained with a state-of-the-art method commonly used for adult population.

Cortical Surface Reconstruction

4

4.1 Introduction and background

The human cerebral cortex is a highly folded ribbon of gray matter that lies inside the cerebrospinal fluid and outside the white matter of the brain. Its folding pattern consists of gyri (singular: gyrus, the visible ridges) and sulci (singular: sulcus, the buried valleys). It is this intrinsically complex structure together with the convolving pattern that makes the extraction of an accurate and topologically correct cortical surface a challenging problem. Yet, a reconstructed cortical surface without correct geometry and topology may lead to incorrect interpretations of local structural relationships and will prevent cortical folding (Han *et al.*, 2002).

4.1.1 Geometry of cortical manifolds

The process of increasing folding and fissuring of the cerebral cortex is referred to as *gyrification*. The exact and complete causality of the cortical folding is still largely unclear, but a few elements are commonly agreed upon. One central hypothesis behind cortical folding pathways is the influence of the fiber tension within the white matter. Indeed, in 1997 David C.Van Essen postulated the tensions of the axons along white matter as the potential responsible for the cortex to fold. (Van Essen, 1997). Other popular hypotheses explained cortical folding as a consequence of the restricted space in the skull (see (Welker, 1990) for a review). On the contrary, other studies emphasized the developmental mechanisms of the cortex ir the relation between the thickness of the supragranular (i.e., cortical layers $I - III$) versus infragranular layers (i.e., cortical layers $V - VI$) as a major causes of gyrification (see (Zilles *et al.*, 2013)).

From gestation to term birth, the fetal brain develops from a simple tubular structure to its complex folding pattern structure. Specially during the second trimester of human fetal development, neural structures in the brain undergo significant morphological changes (Huang *et al.*, 2009). During normal growth, the cerebral cortex gradually folds as the whole brain volume increases and the sulci develop. Chronologically, the Sylvian fissure appears first, followed by the calcarine and the central gyri. The sulci belonging to the parieto-occipital regions are the one emerging the latest (see Fig 4.1). We refer the reader to (Garel *et al.*, 2001) for a complete chronology of sulcation extracted for MR imaging series.

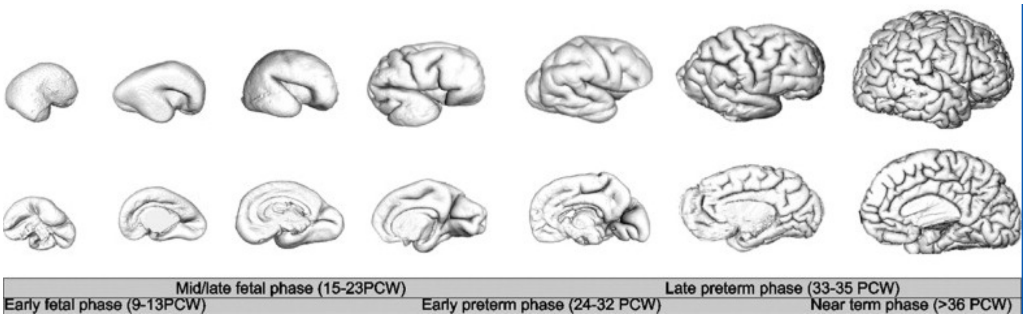

Figure 4.1: Gyrification process: three dimensional reconstruction of the cortical surface from early fetal phase (9-13 PCW) to late preterm phase (33-35 PCW) development.

Thus, at term[1], newborns present an "adult-like"' cortical surface. Although the newborn's brain volume dramatically increases until childhood to reach normal adult-like volume, the cortical pattern, i.e. all the sulci and the gyri, that we see in adults are already present. This is not the case before 40 weeks of gestational age[2] (GA), as we can see in Fig. 4.2). In this figure we show two MR scans of the same prematurely born subject. The first scan was acquired few days after premature birth (the subject was born at 28 weeks of GA) and the second one at *term equivalent age* (TEA)[3]. As expected, the Sylvian fissure and the calcarine and central gyri are already present at 28 weeks of gestation (see again Fig. 4.2).

From normal birth (40 week GA) to adulthood, the brain will moderately increase in volume, while its cortical surface area will drastically increase due to this gyrification process (see Fig. 4.3). This disproportionately large cortical surface area with respect to whole brain volume (when compared to other species) is believed to be the factor that provides the abilities to communicate, synthesize information and perform analytical tasks of human beings.

4.1.2 On curvature

Cortical surfaces are often represented as high resolution unstructured triangular meshes, i.e a 2-manifold $\mathbb{R}^3$. Let S we the cortical surface parametrization. For each point on this surface we can locally approximate the surface by its *tangent plane*, orthogonal to the *normal vector* $\mathbf{n}$.

In differential geometry, for any n-dimensional Riemannian manifold [4] we can derive the first and second fundamental forms, which are quadratic forms of the tangent plane of the manifold. The *first fundamental form* (generally known by the Roman I) is the inner product on this tangent space. It permits de calculation of curvature and metric properties of a surface. In higher dimensions $n > 2$ the *second fundamental form* (denoted by II) is linked with the shape operator[5]. Together with the first fundamental form, it serves to define extrinsic invariants on the surface,

---

[1] A pregnancy with a single fetus lasts 40 weeks from the first day of the last menstrual period. This calculation determines a pregnant woman's estimated date of delivery (EDD). Babies are considered "term" if they born anytime between three weeks before and two weeks after the EDD (37–42 weeks of gestation). Nevertheless, in this dissertation *term birth* or just *term* refers to being born at 40 weeks of gestational age.

[2] "Gestational age" (or "menstrual age") is the time elapsed between the first day of the last normal menstrual period and the day of delivery.

[3] Term equivalent age is a term used to describe children who were born preterm. This term is referred to the moment the newborn reaches the "normal" full-term age, i.e. 40 weeks GA.

[4] These two forms are usually denoted by I and II, respectively. They were originally introduced by Gauss.

[5] The second fundamental form is also known as shape tensor.

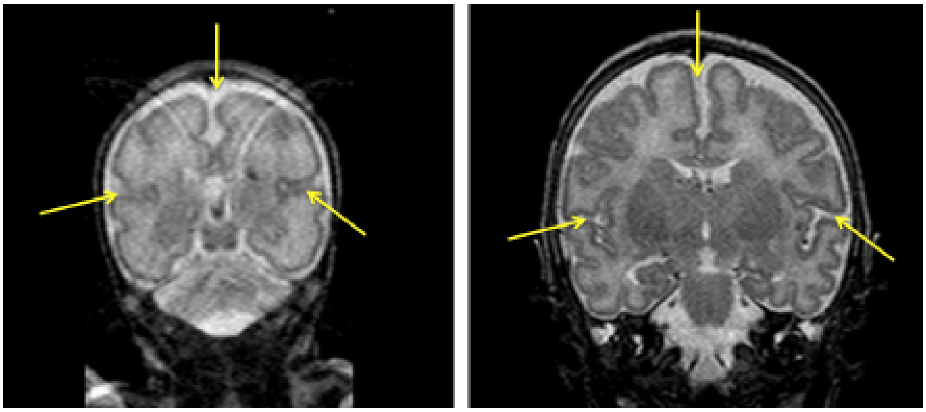

Figure 4.2: MRI scan for the same extreme premature subject at two different time points. The subject in the image was born at 28 weeks gestational age, first scanned 10 days after birth (29.2 weeks postconceptional age) (left) and then re-scanned with the same protocol one month and a half later (39.85 weeks post-conceptional age) (right). Yellow arrows point to landmarks that are already identifiable at 28 weeks of gestation and remain stable along lifespan. As we can see in the image, the gyrification pattern at term is similar to the adult case (though showing less deep sulci) whereas prior to 40 weeks of GA only few of the sulci are present.

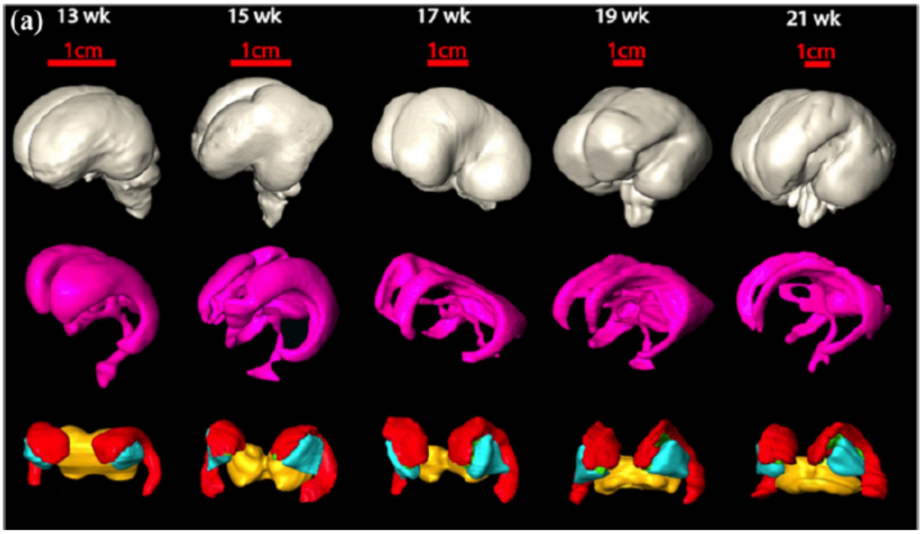

Figure 4.3: Three-dimensional reconstruction of the basal ganglia and ganglionic eminence (bottom row), ventricle (middle row), and whole brain (top row) of a fetus from 13 weeks post-gestational age to 21 weeks. Different colors represent different brain structures: whole brain (gray), ventricle (pink), ganglionic eminence (red), putamen and globus pallidus together (cyan), thalamus (yellow), and caudate nucleus (green). Image from (Huang *et al.*, 2009).

its *principal curvatures* κ_1 and κ_2.

The local bending of the surface is measured by *curvatures*. For every unit direction $\mathbf{e}_\theta$ in the tangent plane, the normal curvature $\kappa_N(\theta)$ is defined as the curvature of the curve that belongs to both the surface itself and the plane containing both $\mathbf{n}$ and $\mathbf{e}_\theta$. The principal curvatures κ_1 and κ_2, are the extremum values of all normal curvatures (Meyer *et al.*, 2002). Indeed, Gauss showed that, despite the fact that at every point of a given surface there is an infinite number of directions, there are always two directions that produce a maximum and a minimum value of curvature. These directions are always orthogonal to each other. One can express the normal curvature of a surface in terms of its principal curvatures such as:

$$\kappa_N(\theta) = \kappa_1 cos^2(\theta) + \kappa_2 sin^2(\theta) \tag{4.1}$$

The *mean curvature* k_H (or simply H) of a surface is an extrinsic measure of curvature that locally describes the curvature of an embedded surface in its ambient space[6]. It is defined for objects embedded in another space in a way that relates to the radius of curvature of circles that touch the object. It is not a property of the surface itself, but rather of how it is embedded in three-dimensional space (Ronan *et al.*, 2011). It is defined as the average of the normal curvatures, i.e:

$$H \triangleq \frac{1}{2\Pi} \int_0^{2\Pi} \kappa_N(\theta) d\theta \tag{4.2}$$

Combining 4.1 and 4.2 leads to the well-know definition of the mean curvature H as the average of the principal curvatures:

$$H = \frac{\kappa_1 + \kappa_2}{2} \tag{4.3}$$

The *intrinsic curvature* (also known as Gaussian curvature and denoted by κ_K or K), is a function of the surface itself and it is defined as the product of the two principal curvatures:

$$K = \kappa_1 \kappa_2 \tag{4.4}$$

The degree of intrinsic curvature is proportional to the degree of differential expansion; bigger differences in expansion across the surface give rise to greater degrees of intrinsic curvature.

The *first variation of area* formula relates the mean curvature of a hypersurface to the rate of change of its area, as it evolves in the outward normal direction. If $\sum(t)$ is a smooth family of oriented hypersurfaces in M, such that the velocity of each point is given by the outward unit normal at that point, the the first variation of area is given by:

$$\frac{d}{dt} dA = H \cdot dA \tag{4.5}$$

where dA is the area element of $\sum(t)$. This equation provides a direct relation between surface area minimization and mean curvature flow, reflecting that a surface with zero mean curvature everywhere has minimal area [7].

---

[6] Ambient space is the space surrounding a mathematical object.

[7] Note that $H = 0$ is the Euler-Lagrange equation for surface minimization.

4.1.3 Surface extraction and reconstruction

Cortical surfaces are generally extracted from segmented volumes, generally by tesselating the volumes coming from isosurface representations. This is done once cutting planes have been computed to separate the two hemispheres and disconnect the subcortical structures. Yet, this procedure is far from trivial when dealing with neonatal data. The first studies for automatic newborn MRI segmentation were done using the k-nearest neighbour algorithm (KNN) (Weisenfeld & Warfield, 2009), over different MR contrasts (T1w, PD, T2w). Atlas-based segmentation has been also applied in newborns Pastrawa *et al.* (2005), but such methods need probabilistic atlases to overcome intensity contrast limitations. More recently, some knowledge-based segmentation algorithms have been developed for neonatal brain segmentation (Bazin & Pham, 2007; Nishida *et al.*, 2009; Weisenfeld & Warfield, 2009; Xue *et al.*, 2007). Typically, those methods combine (1) an intensity image, which can be used as an intensity model for the atlas-to-subject registration, and (2) some probabilistic maps of GM, WM and CSF, which can be used as prior tissue probability maps for guiding segmentation. However, the major drawback in those studies (as in general for all segmentation studies) is that the validation of the results is difficult to achieve as there is no gold standard. The commonly used standard (the manual segmentation), is difficult to obtain since highly convoluted structures in low-contrast, noisy data are very hard to trace. Moreover, in newborn MRI, myelinated and non-myelinated white matter have ambiguous boundaries, which makes manual segmentation results highly variable and difficult to reproduce (Pastrawa *et al.*, 2005).

In this work, we used the segmentation method proposed by Gui et al. (Gui *et al.*, 2012). This method is based on the infusion of high-level brain morphology knowledge, regarding relative tissue location, connectivity and structure (Gui *et al.*, 2012). Thus it does not require manual interaction, or the use of an atlas, and the generality of its priors makes it applicable to different neonatal populations (preterm and full-term born infants), while avoiding atlas-related bias.

Once segmented, the resulting cortical sheet can be split into two hemispheres, linked by the corpus callosum and the anterior and posterior/fornix comissures. Intrinsically, its "unfolded" structure is that of a two-dimensional (2-D) sheet, which is several millimetres thick (Ségonne *et al.*, 2005). From the Riemannian geometry, we know that any 2-manifold[8] without topological artefacts can be mapped conformally onto a sphere. Thus, if the opening at the brain stem is artificially closed, each hemisphere of the cortical surface is geometrically equivalent to a sphere (Han *et al.*, 2002), provided one can assume that the resulting cortical surface, after the closing, is a smooth twice-differentiable 2-dimensional manifold embedded in $\mathbb{R}^3$.

Due to this equivalence, the projection of the cortical surface onto a spherical manifold is commonplace, specially in downstream applications where further processing is intended. For instance, mesh inflation allows coarse registration, a challenging task when facing the highly irregular structure of the reconstructed cortical sheet meshes. This mapping gives rise to spherical feature maps, either after inflation (Fischl *et al.*, 1999a,b) or conformal mapping (Angenet *et al.*, 1999), that are used in surface registration task. As we will see in the next chapter, the registration process using these spherical surfaces is driven by the features embedded on them such as surface normals, curvature, geodesic distances to crown vertices, as well as anatomical features like cortical thickness or sulcal depth.

Nevertheless, the segmentation procedure is likely to introduce errors. Due to noise, partial volume effects, and other problems during the MRI data acquisition process, the reconstructed brain surface mesh often contains topological defects and artefacts. Added to the acquisition

---

[8] A Riemannian manifold is a smooth and parametrized surface.

errors, the segmentation of the MRI images also yields to errors, as voxels considered as outliers [9] often translate to surface singularities that are hard to detect. Thus, and even if a brain surface is not required to be homeomorphic[10] with a sphere, for inter-subject analysis it is preferable to repair such errors before further processing, specially if its inflation is imaginable (Yotter *et al.*, 2009). This step, crucial for improving noisy surfaces acquired from scanning devices, is intended to avoid errors in downstream applications, like model reconstruction and numerical simulation. It is commonly referred as *mesh denoising*.

On the other side, for computational purposes, surfaces are usually modelled by polyhedral surfaces, a procedure also know as surface tesselation. It is generally done using isosurface constructions algorithms (Lorenson & Cline, 1987). An advantage of an isosurface representation is that it naturally supports models of arbitrary genus[11], that is, with any number of handles (Wood *et al.*, 2004). Indeed, polygon meshes are quite easy to generate since all we need is a set of sample points on the subject's surface that have to be connected in order to define a piecewise linear approximation of the underlying surface (Bischoff *et al.*, 2005). However, surfaces extracted from volumetric data are often of arbitrary topology and are in need for a fairing (i.e. *surface smoothing*) step to ensure the required manifold smoothness (Taubin, 1995a). Indeed, while the tesselation of the surface produces meshes that are sufficient for mere visualization, the resulting triangulated surfaces are not suitable for further processing since they may have small holes, overlapping faces, degenerate triangles [12], singularities or other topological and geometrical inconsistencies.

Albeit having some substantial differences, denoising in mesh processing is similar to smoothing or fairing. Denoising removes the noise or spurious information, while trying to preserve the original feature frequencies. Smoothing or fairing, by contrast, removes certain frequency information on the surface mesh (Wang *et al.*, 2012).

4.1.4 Surface smoothing

The most popular linear technique for surface smoothing is the Gaussian smoothing. It is related to the idea of scale-space (Florack *et al.*, 1995; Perona & Malik, 1990) and it has been widely used thanks to its simplicity in numerical implementation (Perona & Malik, 1990).

Gaussian kernel smoothing (*aka.* Laplacian smoothing) can be viewed as weighted averaging of voxel values. It weight an observation according to the Euclidean distance between one vertex and its neighbours. The main drawback of Gaussian smoothing is that though it effectively reduces high frequency surface information, it tends to flatten the surface (Ohtake *et al.*, 2000). Moreover, Gaussian kernel smoothing does not respect the natural boundaries of objects. Despite its simplicity, it has the problem of shrinkage towards the mean near the data boundary, mainly because the convolution with Gaussian kernel is not a pure low-pass filter operation (Taubin, 1995a,b). Indeed, when smoothing methods are iteratively applied, the shape undergoes significant deformations, eventually converging to the centroid of the original data (Taubin, 2000). In

---

[9] Tissue outliers in the segmentation are voxels wrongly classified as one type of tissue laying outside the tissue of interest.

[10] Loosely speaking, *being homeomorphic* can be translated as *being equivalent*. Formally, in the mathematical field, an homeomorphism is defined as continuous bijection between two topological spaces whose inverse is also continuous.

[11] The genus of a connected, orientable surface is an integer representing the maximum number of cuttings along non-intersecting closed simple curves without rendering the manifold disconnected. It is an invariant property of a manifold and it is equal to the number of handles on it.

[12] Degenerate triangles are faces with total area equal to 0.

other words, the iterative smoothing procedure results in the surface collapsing to a point.

The Gaussian kernel is isotropic in Euclidian space and it assigns the same weights to observations equal distance apart. However, when an observation lies on the cortical surface, it is more natural to assign the weights based on the *geodesic distance*[13] along the surface. Indeed, on the highly convoluted brain surface, data fails to be isotropic in the Euclidean sense, a clear example of how spatial proximity does not always coincide with geodesic proximity[14] (Bischoff *et al.*, 2005). For this reason smoothing data residing on manifolds requires constructing a kernel that is isotropic along the geodesic curves.

In such cases, by solving a *diffusion equation* on a manifold, Gaussian kernel smoothing can be indirectly generalized. The natural extension of the Euclidean Laplacian to an arbitrary Riemannian manifold is called the *Laplace-Beltrami* operator, which is equal to the i^{th} component of the mean curvature vector H. More formally, it is defined as the divergence of the gradient operator.

Since Perona and Malik first introduced them (Perona & Malik, 1990), diffusion equations have been widely used in image processing as a form of noise reduction. Diffusion smoothing generalizes Gaussian kernel smoothing to an arbitrary manifold (Chung, 2004). This kernel generalization is known as a *heat kernel*. It has been widely used in computer vision, mainly for surface fairing and mesh regularization (Desbrun *et al.*, 1999; Sochen *et al.*, 1998; Taubin, 1995a, 2000) as well as in smoothing data along the cortical surface (Gaser *et al.*, 2006). The heat kernel can be interpreted as the transition probability density for an isotropic element with respect to the surface area element.

When solving the diffusion equation on a curved surface, the Laplacian has to somehow incorporate the geometry of the curved surface. One can use the finite element method (FEM) to represent the Laplace-Beltrami operator explicitly for an arbitrary surface. Yet, in the case of a triangulated manifold, it is not necessary to calculate the Beltrami flow through evaluation of the intrinsic Beltrami operator formulation. Indeed, in such cases, manifolds and embedding need not necessarily be analytically defined through parametrizations and metrics. Instead, the manifold can be sampled as discrete values at triangulated vertex and one can take advantage of the equivalence of the mean curvature vector, which can be directly estimated from the enhanced triangulated mesh M.

4.1.5 Curvature estimation

Roughly speaking, the discrete mean curvature flow moves every vertex in the normal direction with speed equal to a discrete approximation of the mean curvature at the vertex (Ohtake *et al.*, 2000). The problems then reduces to finding a good and efficient curvature estimator.

An intuitive approach to estimate curvatures in a triangulated manifold consists of estimating the *first* and *second fundamental forms* of the manifold. Hamann fitted a bivariate polynomial locally to the vertex of interest and its first-order neighbours (Hamann, 1993). As both principal curvatures κ_1 and κ_2 are computed separately, both the mean curvature H and the intrinsic (*aka*

---

[13] The Euclidean distance is the standard distance in 3D spaces. It is a extrinsic property of a surface and is not invariant under isometric mapping. Geodesic distance is an intrinsic property of a surface, thus invariant to parametrization, and computed as the shortest path that links 2 points of the surface.

[14] On the curved surface, a straight line between two points is not the shortest distance so one may assign smaller weights to closer observations.

Gaussian) curvature K are then easily computed.

Yet, most of the curvature discretization methods which deal with 2D manifolds embedded in a 3D space are mean curvature-only estimators. These estimators usually take the general form:

$$\mathbf{H}(\mathbf{x}_i) = \sum_{j \in N_1(x_i)} \omega_{ij}(\mathbf{x}_i - \mathbf{x}_j) \tag{4.6}$$

where $N_1(x_i)$ denotes the "$1 - ring$" neighbours of vertex x_i, i.e.vertices that are directly connected to x_i thorough a single edge, and where ω_{ij} are some weights assigned to the edge.

Taubin in (Taubin, 1995a) proposed the inverse number of $N_1(x_i)$ as a possible choice for edge weight, such as:

$$\omega_{ij} = \frac{1}{\mid N_1(x_i) \mid} \tag{4.7}$$

where $\mid \cdot \mid$ denotes the cardinality of a set. The resulting estimator is the *umbrella operator*. Desbrun et al. proposed a more sophisticated weighting (Desbrun *et al.*, 1999):

$$\omega_{ij} = \frac{cot\alpha_j + cot\beta_j}{4A} \tag{4.8}$$

where α_j and β_j are the two angles opposite to the edge $e_{i,j}$ in the two triangle sharing this edge, and A the sum of the areas having $\mathbf{x}_i$ as a common vertex, i.e. the area of the $1 - ring$ patch. The complete mean curvature vector estimator can be written as follows:

$$\mathbf{H}(\mathbf{x_i}) = \frac{1}{4A} \sum_{j \in N_1(i)} (cot\alpha_j + cot\beta_j)(\mathbf{x}_i - \mathbf{x}_j) \tag{4.9}$$

Compared to Desbrun's estimator, Meyer's et al. discretization differs only in the area term (Meyer *et al.*, 2002): they chose the *Voronoi region* around vertex x_i so the triangles do not overlap [15].

Albeit less common, the estimation of the intrinsic curvature of the surface, K, is done in a similar way as the mean curvature vector estimation. Formally, we first need to find an exact value of the integral of the intrinsic curvature K over a finite-volume region on a piecewise linear surface. Instead, this integral is approximated through intrinsic curvature measures at each vertex of the surface reconstruction using the principles of the *Gauss-Bonnet* scheme for the $1 - ring$ neighbourhood:

$$\int \int_A K dA = 2\Pi - \sum_{i}^{N_{fac}} \theta_i \tag{4.10}$$

where θ_i is the angle of the i_{th} face at the vertex x_i and N_{fac} denotes the number of faces around this vertex. Particularly, the intrinsic curvature is calculated as the surfeit or deficit of the vertex angle divided by one third the sum of the vertex areas:

$$K = \frac{2\pi - \sum_i^{N_{fac}} \theta_i}{\frac{1}{3} \sum_i A_i} \tag{4.11}$$

---

[15] The Voronoi region is chosen for non-obtuse triangles only, and some specific care needs to be taken for obtuse triangles.

Formally, the cerebral cortex is both extrinsically and intrinsically curved (Ronan *et al.*, 2011). The mean curvature clearly follows the morphology of the cortex and sulci and gyri will always be represented by opposite local extrema of the mean curvature map. The intrinsic curvature is of a much higher spatial frequency, indicating uneven differential rates of tangential surface development of the human cortex. Indeed, differential expansion, if present, increases as expansion increases, i.e. as the magnitude of the surface area increases. This is analogous to changes in cortical gyrification, which also increases as surface area increases.

4.2 Context and motivations

Smoothing methods are most often designed from a graphical point of view, with the only goal of improving mesh smoothness. Certainly, the Laplacian smoothing flow increases mesh regularity, but also develops unnatural deformations. Smoothing by the discrete mean curvature flow is relatively independent from the mesh sampling rate, but increases the mesh irregularity. Both approaches may lead to oversmoothing and loosing desirable geometric features.

In short, and albeit their relative simplicity, smoothing methods are generally devoted only to reduce mesh noise for rendering or visualization purposes. Indeed, smoothing methods focus on creating meshes of correct topology, while disregarding the geometry of the resulting triangulation. They do not generalize well to MRI data sets or biomedical imaging tasks, reducing their utility.

4.2.1 Motivations

Smoothing methods provide topologically correct surfaces. Yet, they do not handle mesh geometric singularities such as sharp peaks or high geometric inconsistencies of the triangulation. These sharp peaks, which are nearly invisible artefacts, hinder subsequent operations like mesh simplification, remeshing and parametrization (Wood *et al.*, 2004).

To re-establish the homeomophism between the sphere and the brain, several automated approaches have been proposed. They can be divided in 3 groups: (i) methods that enforce topological constraints during the segmentation process (Han *et al.*, 2002), (ii) methods that correct the segmentation results directly on the volumetric data (Ségonne *et al.*, 2005) and (iii) methods that work on triangulated surfaces. The method presented in this chapter belongs to this last group, as only the segmentation labels are provided.

In this chapter we address the problem of reconstructing the cortical surface, assuring correct topology *and geometry*, an essential step for building the newborn connectome. We use a combination of already existing techniques borrowed from the medical imaging processing and computer vision fields, together with a newly developed technique for mesh singularities detection and removal, and surface restoration. We present a fully automatic technique which converts a geometrically inconsistent input mesh into an output mesh that is *guaranteed* to consistently represent the closed manifold surface of the cortical surface of a newborn subject.

We consider several functions of the curvatures on the gray-white junction. In particular, the method is executed using the following steps: (1) conversion of the cortical surface to FreeSurfer data format and (2) computation of mean and intrinsic curvatures using FreeSurfer software (Dale *et al.*, 1999; Fischl, 2012), (3) peak detection based on curvature information, (4) peak removal using $i^{th} - ring$ information, (5) point cloud reconstruction using the SSD method (Calakli & Taubin, 2011) and finally, (6) inflation of the corrected surface onto the sphere, again using FreeSurfer tools. This process is sketched in Fig. 4.4.

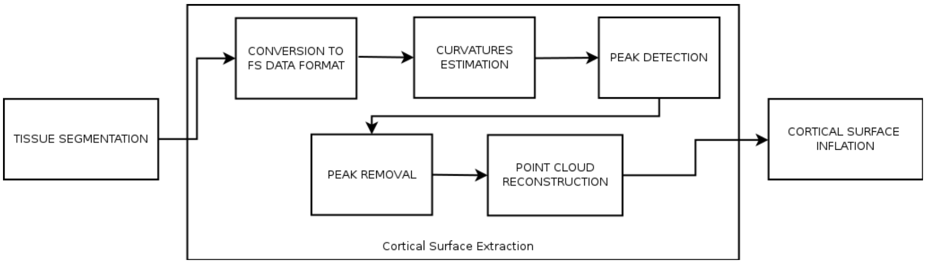

Figure 4.4: Block diagram showing the main processing steps to restore and reconstruct the cortical surfaces.

4.3 Materials and methods

In the next paragraph we will describe in more detail the available brain dataset and the surface restoration scheme employed to build topological and geometrical correct cortical surfaces. The main goal is to obtain a reliable representation of the newborn cortex so it can be used to obtain an anatomical coherent cortical parcellation of the newborn brain.

4.3.1 Newborn data

Four neurological normal preterm neonates with corrected gestational ages (GA) between 29-33 weeks were imaged. The imaging protocol included T1-weighted (T1w) and T2-weighted (T2w) MR sequences, collected on a $1.5T$ Eclipse Philips scanner. The protocol was approved by the local ethic committee and the infants' parents gave written in formed consent for the acquisitions. Coronal images covering the whole head (including the skull) were acquired. For the T1w images, the MPRAGE protocol was used, with $TE = 2.5ms$, $TI = 1100ms$ and $TR = 2200ms$. For the T2 image, the TSE protocol was used, with $TE = 150ms$ and $TR = 4600ms$. The resolution for both scans was of $0.7x0.7x1.5mm^3$. The acquisition time was of 6 min 29 s for the T1w image, and of 5 min 33 s for the T2w image. Three localizers (axial, coronal and sagittal) were used to ensure proper alignment of the coronal planes with the longitudinal axis of the brainstem. When the acquired images were affected by newborn motion, acquisition was repeated until satisfactory scans could be obtained.

This dataset is a subset comprising 4 subjects from a longitudinal dataset from the Geneva University Hospital. In this database, preterm children were longitudinally scanned at three different time points: (i) at birth, provided that the newborn infants did not need any clinical support such as artificial ventilation, (ii) at term equivalent age (i.e. at 40 weeks of corrected GA) and at (iii) 6 years-old. In Part I of this thesis manuscript we used the third time point while in Part II we will focus in the second time-point. Time-point 1 and 2 scans were acquired between years 2002-2004. Time point 3 was acquired in between 2008-2010.

Images were segmented using the method proposed in (Gui *et al.*, 2012). This method provides us with a segmentation at both global level (it automatically separates both hemispheres) and at the tissue level. It performs, in this order: (1) extraction of the intracranial cavity and of the two hemispheres, (2) detection of the subcortical gray matter,(3) separation of the cortical gray matter, unmyelinated white matter and CSF, (4) segmentation of the cerebellum and of the brain-stem, and (5) detection of the myelinated white matter (see Fig. 4.5 as an example).

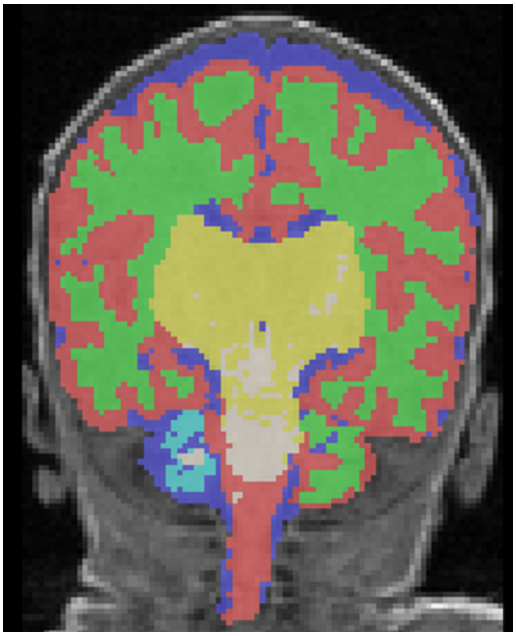

Figure 4.5: Coronal view of the detection of cortical an subcortical gray matter, myelinated and unmyelinated white matter and CSF for a for one of our four subjects' MR scan. Red – cortical gray matter, yellow - subcortical gray matter, green - myelinated white matter, white – unmyelinated white matter, blue – external CSF obtained with the method proposed in (Gui *et al.*, 2012). Notice the presence of mislabelled voxels mainly in the interface between GM and CSF.

While the overall segmentation is of good quality, we still have some outliers, mislabelled voxels and disconnected components. Mislabeled voxels appear mainly at the interface between the cerebrospinal fluid (CSF) and GM. Because CSF has the highest intensity in neonatal T2w images and the image resolution of neonatal MRI is usually no more than $0.9mm^3$, many voxels between CSF and GM will have similar intensities to WM which is brighter than GM and darker than CSF. These outliers appear mainly in the cortical gray matter and within the white matter.

4.3.2 Proposed scheme for cortical surface restoration

Starting from the tissue classification generated by the automated segmentation algorithm (Fig. 4.5), we reconstruct the inner (WM-GM) and the outer (GM-CSF) cortical surfaces using the algorithm proposed in (Dale *et al.*, 1999; Ségonne *et al.*, 2005) and included in the freely available Freesurfer (FS) package (Fischl, 2012) (see Figure 4.6) .

We do not apply the whole FS-processing stream. The method first introduced in (Dale & Sereno, 1993) and further developed by (Dale *et al.*, 1999) comprises several steps that are not meaninful for neonatal data, such as Talairach registration, intensity normalization, skull-stripping and white matter labelling. Instead, we use our segmented volume as a WM mask (after converting it to the FreeSurfer data format) and run the FreeSurfer stream from the tesselation step.

Reconstructed noisy surfaces

Each reconstructed cortical surface is represented as a polygon mesh consisting of between $70,000$ and $120,000$ triangles. Though in adult procedures the pial surface (GM-CSF interface) is generally used, in this study we rather use the WM-GM interface, which appears to be a less distorted version of the cortical surface (see Figure 4.6, green line).

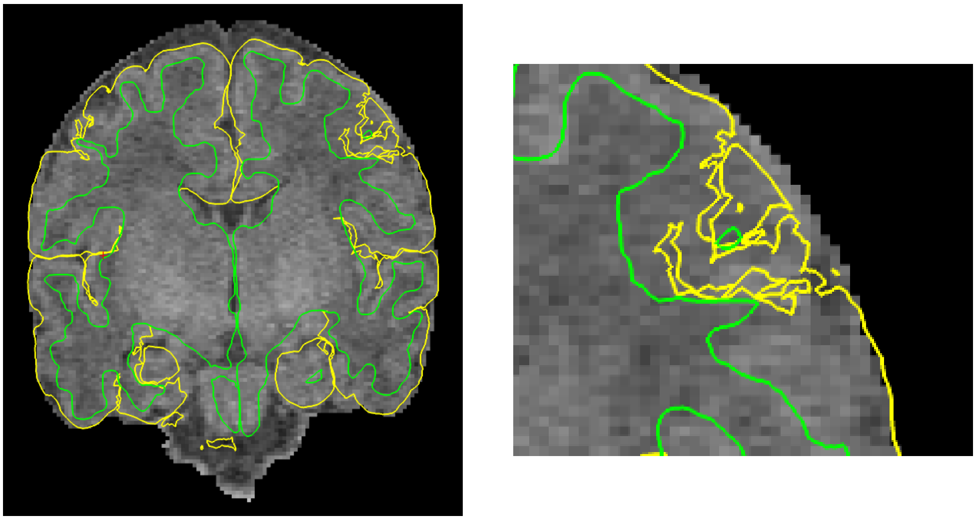

Figure 4.6: (a) Intersection of tessellated WM (green line) and GM (yellow line) surfaces with the MRI volume for newborn data. In some regions, both surfaces collapse to a single point preventing a correct pial surface extraction. (b) Zoom to a central region of the brain. Due to technical limitations, the convolving pattern of the CSF-GM interface is lost.

Due to the on-going myelination process, the boundaries of the pial surface extracted from the segmentation process collapse with the GM-WM interface in some regions. This absence of the pial interface mainly occurs in the frontal lobe of the brain known to myelinate later in development. Yet, due to technical limitations in the pre-processing methods, the folding pattern is almost lost on the CSF-GM interface, making impossible to use the curvature information needed for the surface correction algorithm (see Figure 4.6, (b)). On the contrary, the white matter surface matches directly a morphological feature and also tends to be less sensitive to cortical thinning or thickening. Some studies have recently proposed the use of the central cortical surface (i.e. the middle line between GM and WM) as a more accurate representation of the newborn cortex (Xue *et al.*, 2007). In this study, the resulting inner and outer surfaces did not allow us to obtain a correct central surface.

Surface pre-smoothing and peak detection

The reconstructed WM surfaces are first smoothed using 10 iterations of the smoothing method proposed by Taubin (Taubin, 1995a). This method alternates two scale factors of opposite signs with the negative factor of larger magnitude in a weighted Laplacian flow[16]. In our settings, these factors are set to $\lambda = 0.5$ and $\mu = -0.53$. This method suppresses high frequencies of the discrete Laplacian operator defined on the mesh while enhancing low frequencies, all without shrinking the surfaces. Fig. 4.7 and 4.8 display the same surface before and after smoothing. This first step provides us with relatively smooth surfaces[17], without handles or holes.

Yet, the resulting meshes still contain inaccuracies such as degenerate and self-intersecting faces, with vertices being located within neighbouring or slightly distant triangles (see Fig. 4.9). Those sharp peaks and micro-folds are likely to have a high impact on later processing, as for example, preventing surface inflation to the sphere. Even if the smoothness constraint on the manifold is assured after smoothing, the resulting spherical parametrization on the sphere might not be correct [18].

To detect these mesh inconsistencies we propose to analyze both the mean and the intrinsic curvature of the smoothed surface. As already mentioned in Section 4.1.1, the cortical surface has a particular geometry, being both intrinsically and extrinsically curved (Ronan *et al.*, 2011). Its extrinsic curvature (i.e. mean curvature, H) arises from mechanical folding of the surface, while its degree of intrinsic curvature (i.e. Gaussian curvature, K) is proportional to the degree of differential expansion (Ronan *et al.*, 2011). Thus, while the mean curvature provides information of the gyrification pattern, the intrinsic curvature is related the non-uniform surface expansion. This means that some points expand faster than others, introducing a variance into the distance between points. Importantly, this variance increases as expansion increases, such that points that expand the fastest will increase the distance between them at a greater rate than points that expand slower. In other words, the intrinsic curvature can be seen as a marker for the folding process.

Hence, over the smoothed surface we calculate both the mean and the intrinsic curvature maps, as well as the face normals, chosen to point outwards the surface. The surface mean curvature is estimated using the Desbrun approximation (as in eq. 4.9) while the intrinsic curvature maps are computed using the Gauss-Bonnet scheme (eq. 4.10). From those maps, we propose to characterize the sharp peaks (or spikes) on the surface as vertices of high mean and intrinsic curvature, whose "$1st - ring$" neighbourhood show *non-consistent normals* (see Fig. 4.10).

Let x_i and x_j be two vertices of mesh M and e_{ij} the edge connecting x_i to x_j. The "$1st-ring$" neighbourhood $N_1(i)$ of x_i is defined as all vertices x_j such that there exist and edge e_{ij} between x_i and x_j. In this work, we define the neighbouring normals as being non-consistent if at least one angle between the normals of the triangles forming the $N_1(i)$ of v_i is higher than 90 degrees.

The "normals constraint" over the surface give us a set of potential spikes. However, just considering the surface's normal information would lead to erroneously detect vertices as being artefacts or mesh singularities. To check whether a given vertex x_i is a peak or not, we estimate the principal curvatures of the mesh. Then, if the neighbourhood of x_i show normals inconsistencies, i.e. the polygons forming this N_1 ring have normals with opposites signs, and the curvature estimates at vertex x_i have extreme values, this vertex is considered to be a peak. In summary, as curvatures can de estimated at every point on a surface, i.e. at each vertex of the triangulated mesh (again, see Section 4.1.1) ,we use this information for selecting the *true spikes* among the

---

[16] When the scale factors are equal in magnitude, the Taubin smoothing scheme its equivalent to the bilaplacian smoothing flow (Kobbelt *et al.*, 1998)

[17] A smooth surface means a surface which is regular, oriented, compact with or without boundaries.

[18] Indeed, if these inaccuracies are not fix before the inflation procedure, the resulting sphere parametrization will be not bijective.

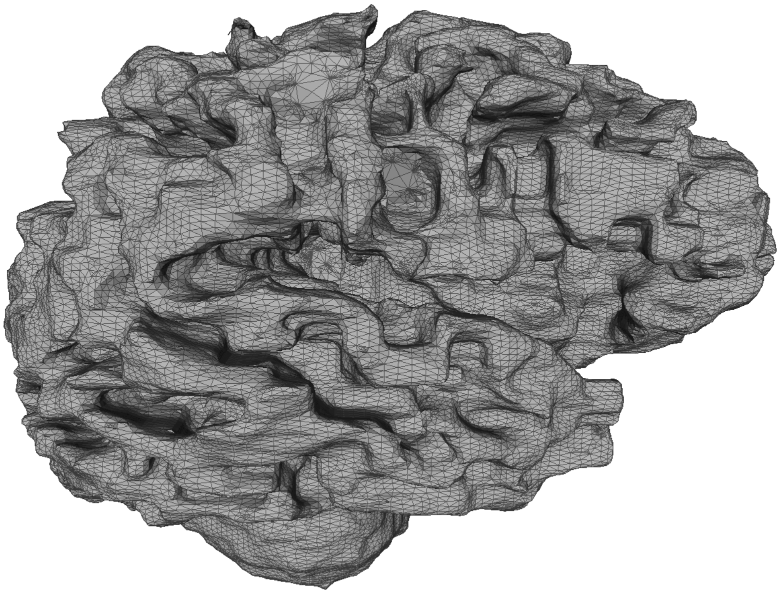

Figure 4.7: Original tesselated surface for one subject's right hemisphere.

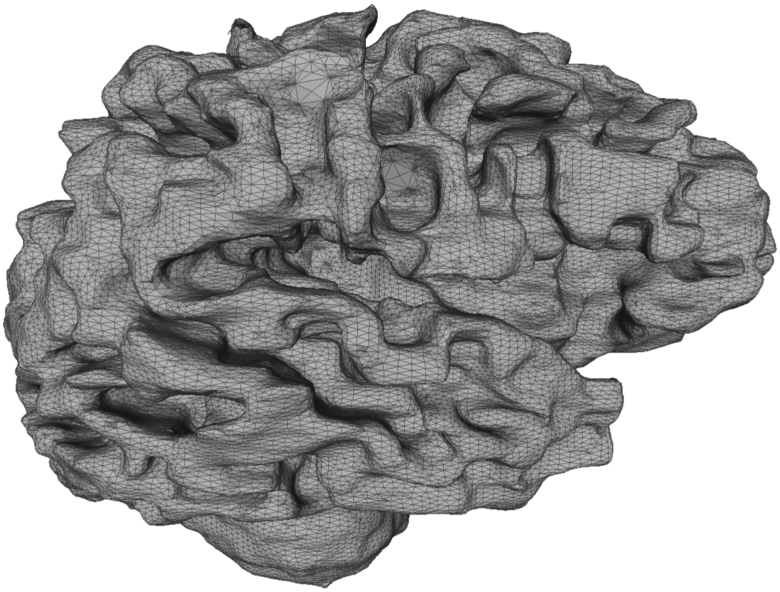

Figure 4.8: Same surface after 10 iteration of the Taubin smoothing approach with $\lambda = 0.5$ and $\mu = -0.53$. The surface appears to be smooth and some topological errors are removed. Although the underlying tesselation increases in its regularity, sharp peaks are still present.

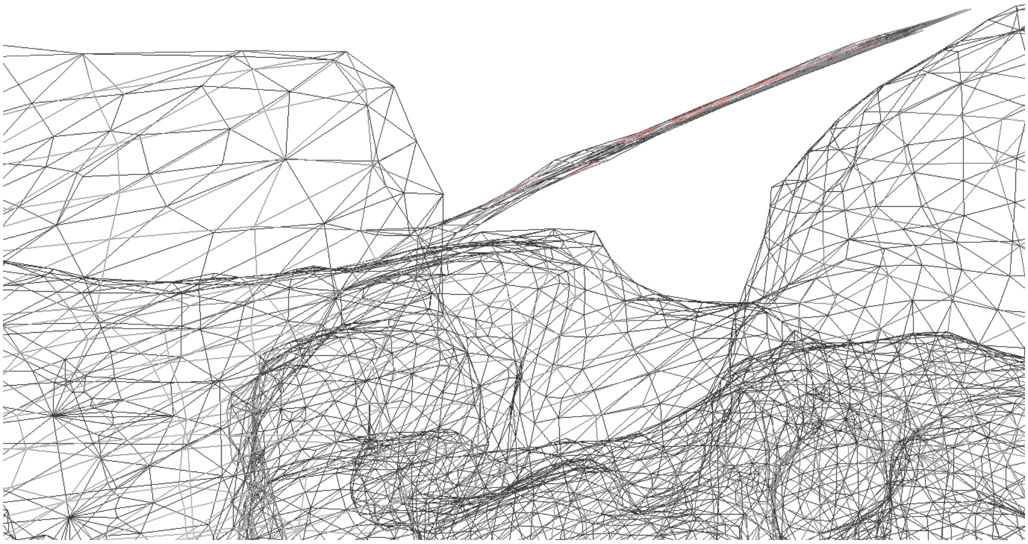

Figure 4.9: Zoom to a sharp peak located in the central part of the right cortical surface reconstruction of a newborn subject. In red, intersecting faces of the surface mesh. As seen in this figure, intersecting faces appear in a peak neighbourhood.

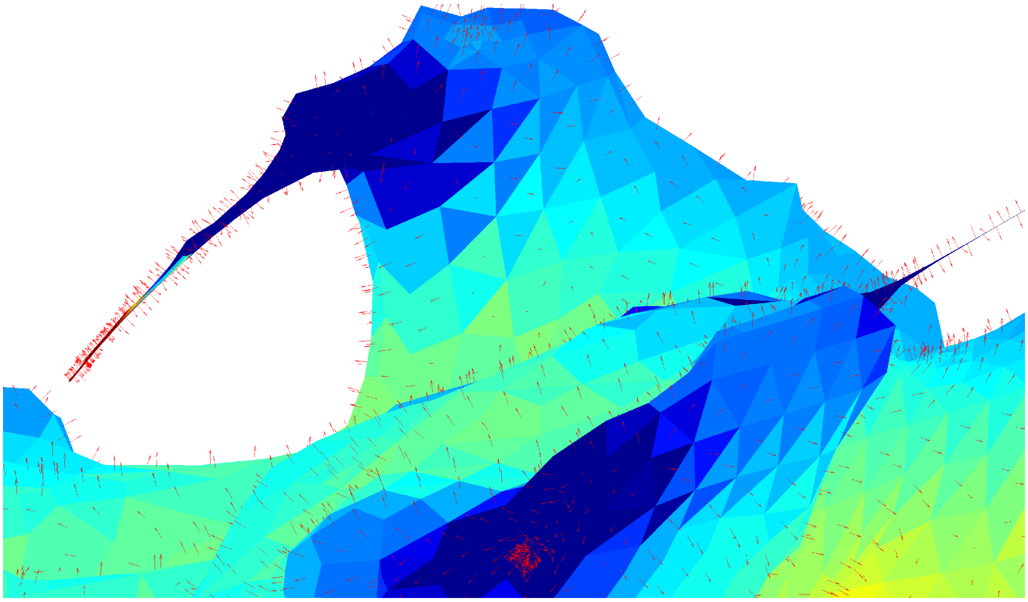

Figure 4.10: Zoom to a sharp peak located in the central part of the right cortical surface reconstruction of a newborn subject. Red arrows show face normals. In the neighbourhood of a peak, face normals are of opposite signs.

candidates obtained using the surface normal information.

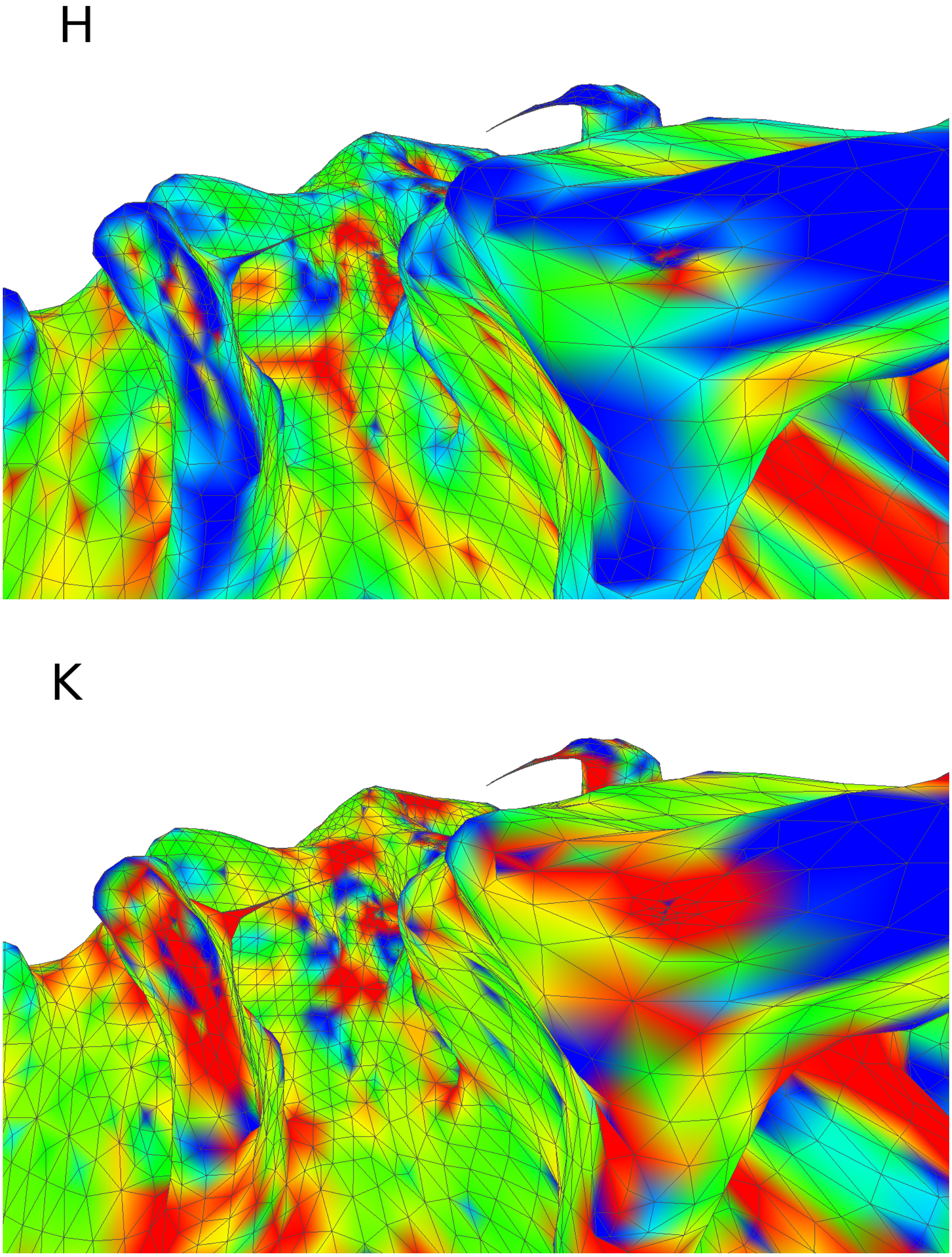

Figure 4.11: Zoom to the central part of the reconstructed cortical surface. Surface is color-coded based on curvature information, showing extreme values on the spikes neighbourhood and in the crest of the gyri. Mean curvature H (top) and Gaussian curvature K (bottom).

In (Pienaar *et al.*, 2008), a qualitative examination of the surface at the millimeter-scale revealed it to be predominantly negatively curved, with an average magnitude of intrinsic curvature of about $0.06mm^{-2}$. Nevertheless, in the FreeSurfer process stream all data is sub-sampled to a unit voxel size of $1mm^3$, giving a limit of resolution of $\frac{\sqrt{2}}{2}mm$, equivalent to a radius of curvature of $1.41mm^{-1}$. In other words, $\mid 1.41mm^{-1} \mid$ is the limit resolution by which we can rely on principal curvature measures. In this context, among the list of candidates we select as peaks those vertices whose curvature was outside this range. Specifically, for the detection we use (1) the mean curvature H, (2) the intrinsic curvature K, (3) the union of both (i.e.vertices whose mean or intrinsic curvature lay outside this range), $U = H \cup K$ and (4) the intersection of both, $B = H \cap K$.

Peak removal and surface reconstruction

Once the surface peaks are detected, they are removed together with their $i^{th} - ring$ neighbourhood. Essentially, we build an isotropic neighbourhood, starting from the vertex detected as a peak. Our algorithm is greedy and processes a single local peak at the time, before moving on to the next one. Indeed, the isolated spikes can be more easily removed one-by-one as we do not require global access and analysis of the entire surface topology. Our approach proceeds as follows: each detected vertex x_i is set as a seed node. From this node, an isotropic neighbourhood search is initialized by selecting all vertices belonging to its $N_1(i)$. Those vertices become at their turn seed nodes, and the procedure is repeated a fixed number of steps, considered as the ring cardinality. Thus, we build an *enhanced neighbourhood of size i*, $i^{th} - ring$,by recursively adding vertices to this neighbourhood, with i being the number of iterations.

The enhanced vertex neighbourhood is removed by eliminating all vertices belonging to the $i^{th} - ring$ and the faces incident to them. This gives us topologically incorrect surfaces of genus $g \neq 0$. To restore the sphere-cortex homeomorphism, rather than attempting to repair the holes directly on the isosurface of the filtered mesh (Zhao *et al.*, 2007), our algorithm considers the remaining vertices as an oriented point-cloud, and reconstruct the surface from those. Filling a complex hole over an irregular region is far from being a trivial issue. Ideally, hole-filling algorithms should be able to cover an arbitrary hole for any model (i.e. they should be robust), while being computationally efficient. Most importantly, they must enable the patched surface to match the missing geometry. Unfortunately, when dealing with the highly irregular and convoluted cortical surface, hole-filling methods hardly satisfy these properties. In particular, the robustness condition.

In this work we chose to reconstruct a watertight surface from the oriented point cloud. It is out of the scope of this chapter to review the state-of-the-art of surface reconstruction. We refer the reader to (Schall & Samozino, 2005) for a survey in recent developments. Among all possible choices, we decided on the method developed by Calakli and Taubin (Calakli & Taubin, 2011). The algorithm formulation is close to the Poisson Reconstruction approach (Kazhdan *et al.*, 2006), and was selected based on its good behaviour near boundaries and holes and uneven sampling as well as its computational efficiency.

The Smooth Signed Distance Surface reconstruction method (SSD) (Calakli & Taubin, 2011) implicitly reconstructs a surface from a finite set of oriented points, forcing the implicit function to be a smooth approximation of the signed distance function on the sphere. As the smooth signed distance can be approximated as a unit slope in the neighbourhood of the point set, the normal vector data can be incorporated directly into the energy function. By constraining the vector field to be the gradient of the implicit function, the problem reduces to a least squares problem and does not require boundary conditions. The implementation of the SDD algorithm uses a primal-graph octree-based hybrid finite element-finite difference discretization and the Dual Marching

Cubes isosurface reconstruction algorithm. In our approach, the octree-resolution is set to 12.

Validation of surface topology and geometry

The topological correctness of a polygonal tessellation can be easily determined by computing the Euler number of the surface. The Euler characteristic is a topological invariant, i.e. a number that describes a topological space shape or structure regardless of the way it is bent. It is commonly denoted by χ. The number of holes or handles (i.e. genus, g) in the manifold is related to the Euler number by the Euler–Lhulier's formula: $v - e + f = 2 - 2g$, where v, e, and f are the number of vertices, edges, and faces, respectively. A topologically perfect reconstruction should result in a surface with no holes ($g = 0$), and thus with Euler number equal to 2, such as the sphere.

Non-manifold components are quite easily detectable. Any point in the triangulated manifold has a neighbourhood topologically equivalent to an open disk in $\mathbb{R}^2$. Thus, any mesh M will be a *manifold mesh* if (i) three corners of a triangle refer to different vertices (no zero area, i.e. degenerate triangles), (ii) each edge bounds exactly two triangles (i.e. two adjacent triangles share the same edge, thus, there are no intersecting faces) and (iii) the star[19] of each vertex forms a single cone.

Validating the geometry of the surface reconstruction is more difficult than validating the topology, since the geometry is variable across individuals, and is not known a priori. When no gold-standard for comparison is available, the goodness of a surface mesh is typically measured by its smoothness and its angle quality (Wang & Yu, 2011). The angle quality makes a significant impact on the approximation accuracy of numerical solutions. Ideally, meshes with uniform angles are more desirable. Yet, triangles with small angles (below 5 degrees, for instance) or extreme aspect ratios lead to badly-conditioned numerical operators.

Thus, in the absence of ground-truth, alternative measures can be used for the assessment of mesh quality. These measures are based on geometric criteria and often serve as a quality control mechanism (Knupp, 2001). They are derived from the singular values of a matrix whose columns are formed by the edge vectors of the mesh elements[20]. They are easily computable and lead to a better assessment on the underlying surface triangulation (Pébay & Baker, 2003). In this work we used as quality measures the angle and edge ratio, the radius ratio and the aspect ratio.

The *angle* (resp. the *edge*) *ratio* is calculated as the ratio between the bigger angle (resp. longer edge) of the triangulation and the smallest (shortest) one. The *radius ratio* ρ is a nondimensional quality measure consisting of comparing for each mesh element (i.e. triangle, t) the radius of the inscribed (r) and circumscribed (R) circle of t. The *aspect ratio* of a triangle is defined as the longest edge divided by its height, where height is the smallest distance of a vertex to a side. It is indirectly related to the area of the mesh elements. These quality measures are generally used to detect the so-called *needle* and *flattened triangles*. In Pébay (Pébay & Baker, 2003) these two nearly-degenerate triangles are defined as follows:

- A *needle* is a non-degenerate triangle that has one and only one angle close to 0.
- A *flattened triangle* is a non-degenerate triangle that has one angle close to Π.

---

[19] The star of a vertex v is defined as the union of all edges and triangles incident upon v

[20] An element quality metric is a scalar function of node positions that measures some geometric property of the element.

Mesh elements belonging to one of these two nearly-extreme cases generally lead to mesh reconstructions that will unavoidably yield to errors in downstream applications. The measures introduced in (Pébay & Baker, 2003) provide extreme values to determine the goodness of the triangular surface reconstruction. When no gold-standard is available, they allow a better assessment of the overall planar and triangulated surfaces. They are defined and extensively discussed in (Pébay & Baker, 2003). We thus refer the reader to it for a comprehensive explanation of the measures.

Other measures over the mesh geometry have been used to measure errors on simplified surfaces (Aspert *et al.*, 2002; Cignoni *et al.*, 1998). A commonly used metric to estimate the distance between discrete 3D surfaces represented by triangular meshes is the *Hausdorff Distance*. The Hausdorff Distance is a mathematical construct to measure the "closeness" of two sets of points that are subsets of a metric space. Informally, two sets are close in the Hausdorff Distance sense if every point of either set is close to some point of the other set (Aspert *et al.*, 2002). In other words, it is the maximum of all the distances from a point in one set to the closes point in the other set.

In this work, for each original reconstructed surface we applied our peak-finding algorithm and artefact removal scheme for (i) 4 different combinations of curvature information (used for peak detection) and (ii) three different ring sizes (for peak removal). The whole set of reconstructed meshes were tested for topology correction by calculating the Euler number and by checking for the existence of degenerate and intersecting faces. We also computed the Hausdorff distance (Aspert *et al.*, 2002) between the original noisy surface and the reconstructed meshes as a measure of reliability of the reconstructed algorithm, as we want the reconstructed surfaces to be as close as possible to the original cortical representation.

In summary, and since no gold-standard was available for the resulting reconstructed surfaces, the initial evaluation of the reconstructed surfaces quality was performed by a visual inspection of the surfaces by an experienced neuroanatomist. In addition to this qualitative evaluation of the final meshes, a quantitative evaluation was performed by the computation of the quality measures defined in (Pébay & Baker, 2003). The Hausdorff Distance allowed us to evaluate closeness to the original surface, while the element quality measures to test for mesh inconsistencies. Their evolution with respect to the ring size and curvature information used for the reconstruction was further mapped and compared in order to determine the default settings for peak detection and surface reconstruction.

Importantly though, the final validation of the surface reconstruction was mainly based on the appropriateness of these surfaces for further processing. Recall that Part II of this thesis is intended to provide tools to aid the development of image analysis methods to obtain a fully automated pipeline to study brain connectivity in newborn data. We will discuss this point the next Chapter.

4.4 Results

Qualitatively, the subjective evaluation of the reconstructed cortical surfaces confirmed the good quality of our results. The reconstructed cortical surfaces maintained the gyrification pattern present in the original mesh, while eliminating the sharp peaks found in the original surface. Yet, while it is hard to observe these subtle differences in mesh geometry by visual comparison, this subjective evaluation allowed us to check whereas our approach yields unnatural mesh deformations. In Figs. 4.12, 4.13, 4.16 and 4.17 figures, we show the best and worst cases. As we can see in Figs. 4.12, 4.13, 4.16 and 4.17, the faceted profile of the surface (specially for the worst case, Fig. 4.16) was smoothed and all peaks and surface inconsistencies were removed while maintaining the original cortical shape (see the little red squares on the image). Indeed, if we look closer to the neighbourhood of one peak, Figs. 4.14 and 4.15, we can see how the peak is completely removed from the surface.

Quantitatively, the resulting reconstructed surfaces appeared topologically correct based on the Euler number, with no degenerate faces or self-intersecting triangles (see Table 4.1) in any of the cases.

	Mesh	Vertices	Faces	Euler number	Nbr. degenerate faces	Nbr. intersecting faces
RH	*Original*	71,244	142,484	2	69	87
	Ring size 4	114,250	228,488	2	0	0
	Ring size 5	113,292	226,572	2	0	0
	Ring size 6	112,224	224,444	2	0	0
LH	*Original*	65,810	131,616	2	66	41
	Ring size 4	102,247	204,499	2	0	0
	Ring size 5	100,821	201,666	2	0	0
	Ring size 6	99,275	198,566	2	0	0

Table 4.1: Topology information for the original mesh of one subject and the reconstructed meshes for different ring sizes for the same subject. The first four rows correspond to the right hemisphere (RH) cortical surface while the last four rows correspond to the left one (LH).

As assessed in Section 4.3.2, the geometrical goodness of the resulting triangulation was evaluated by means of mesh element quality. Table 4.2 reports the mean values of these measures for the original mesh and the reconstructed ones with respect to the ring sizes chosen for the peak removal of one subject. We present here only the results for the surface reconstructed after using the combination of both curvatures (mean and intrinsic) for peak detection. As we will see in the following paragraph, the use of this combined information yields better reconstruction. Yet, the quality measures for the rest of the subjects showed the same trend as the ones reported here.

	Quality measures	Angle ratio	Edge ratio	Radius ratio	Aspect ratio
RH	*Original mesh*	0.4833	1.8171	90.1805	6.3376
	Ring size 4	0.3997	8.3870	11.4257	19.8935
	Ring size 5	0.3997	7.9754	19.6476	20.4782
	Ring size 6	0.3994	7.0788	10.7067	17.3571
LH	*Original mesh*	0.4855	1.7981	66.6559	5.6765
	Ring size 4	0.3983	7.3818	11.2770	17.9076
	Ring size 5	0.3987	6.3881	9.2414	15.6365
	Ring size 6	0.3987	7.0421	10.551	16.9991

Table 4.2: Mean values of mesh elements' quality metrics original mesh of one subject and the reconstructed meshes for different ring sizes. The first four rows correspond to the right hemisphere (RH) cortical surface while the last four rows correspond to the left one (LH).

In all cases, the reconstructed mesh presented smaller mean values of angle ratio and radius

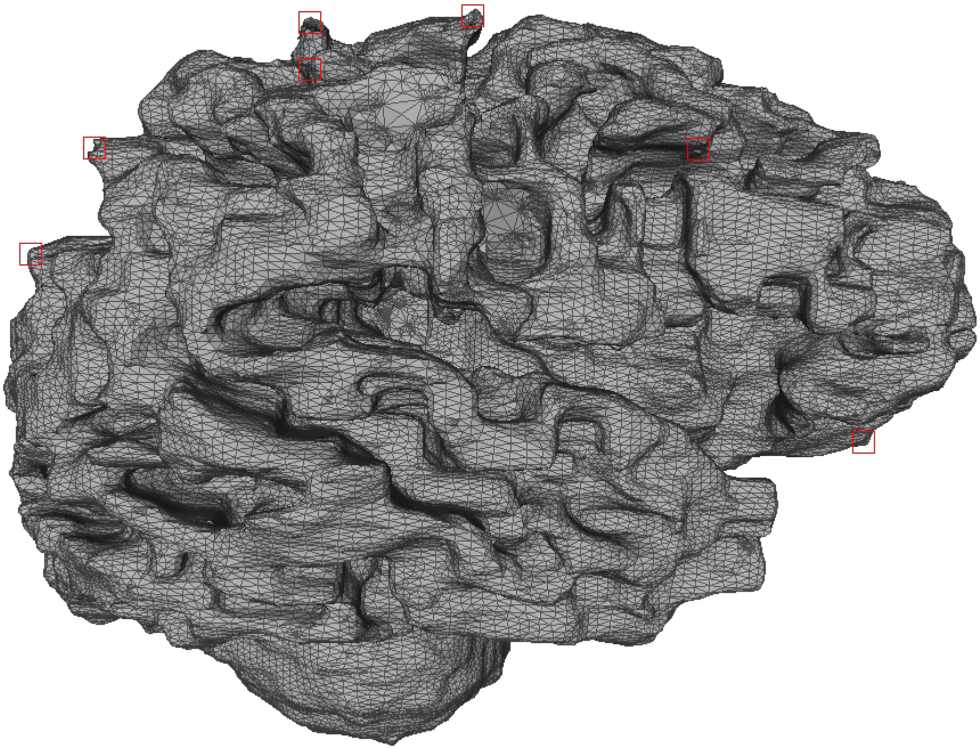

Figure 4.12: Best original cortical surface for one subject's right hemisphere. In red squares, some of the peaks present in the surface.

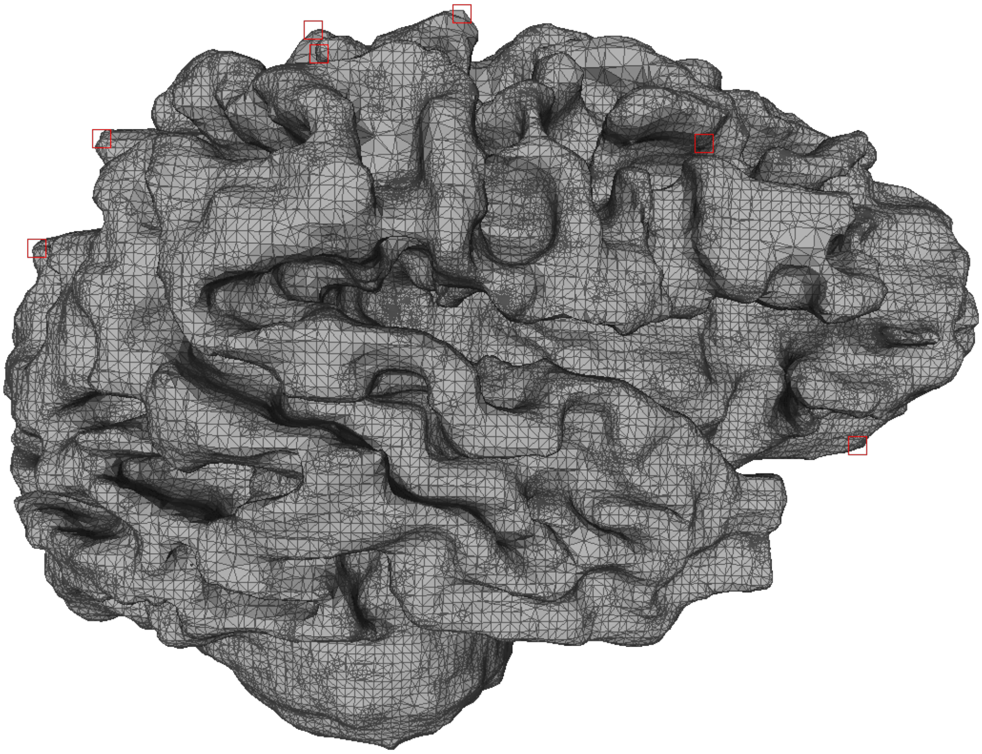

Figure 4.13: Final reconstructed surface. The reconstruction was performed considering the intersection of mean and intrinsic curvature information for the peaks detection and a peak neighbouring size of 5 rings. The peaks and other mesh inconsistencies are eliminated while maintaining the original cortical shape.

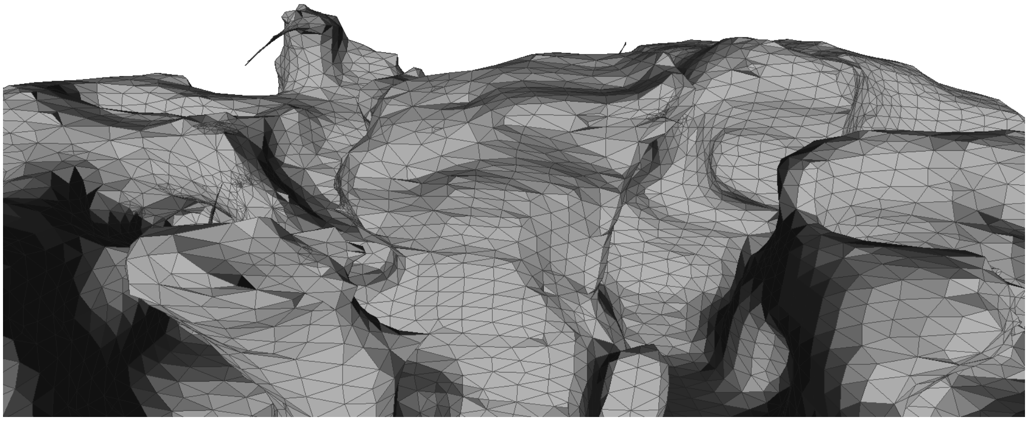

Figure 4.14: Zoom to a peak in the original surface.

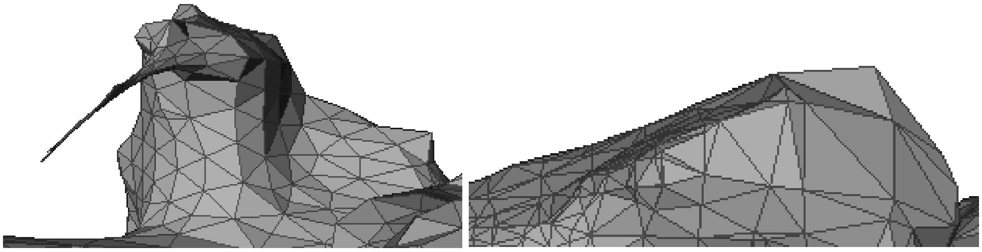

Figure 4.15: Closer zoom to the peak before and after removal.

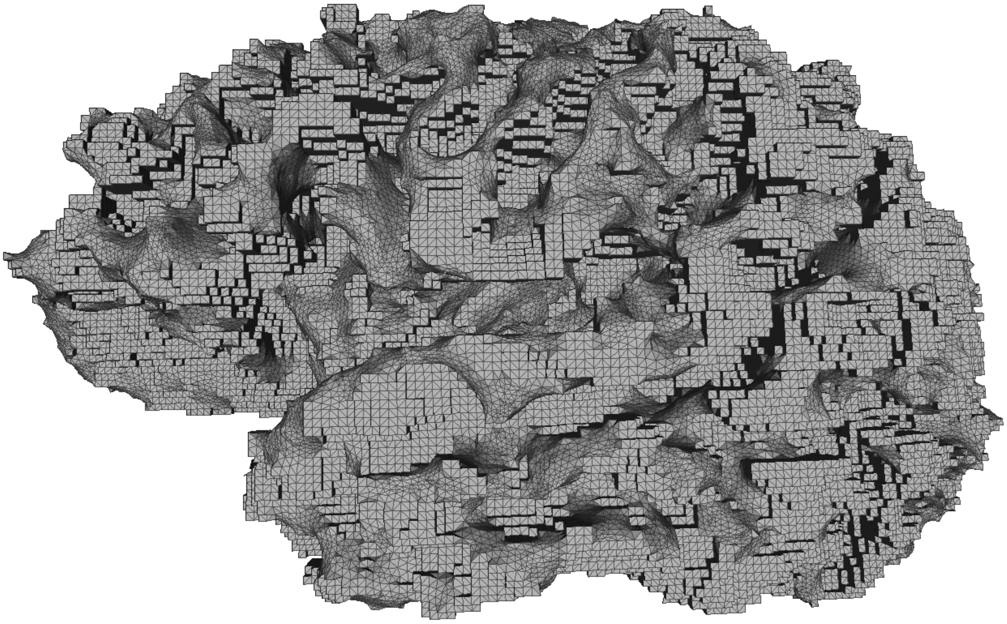

Figure 4.16: Worst original cortical surface.

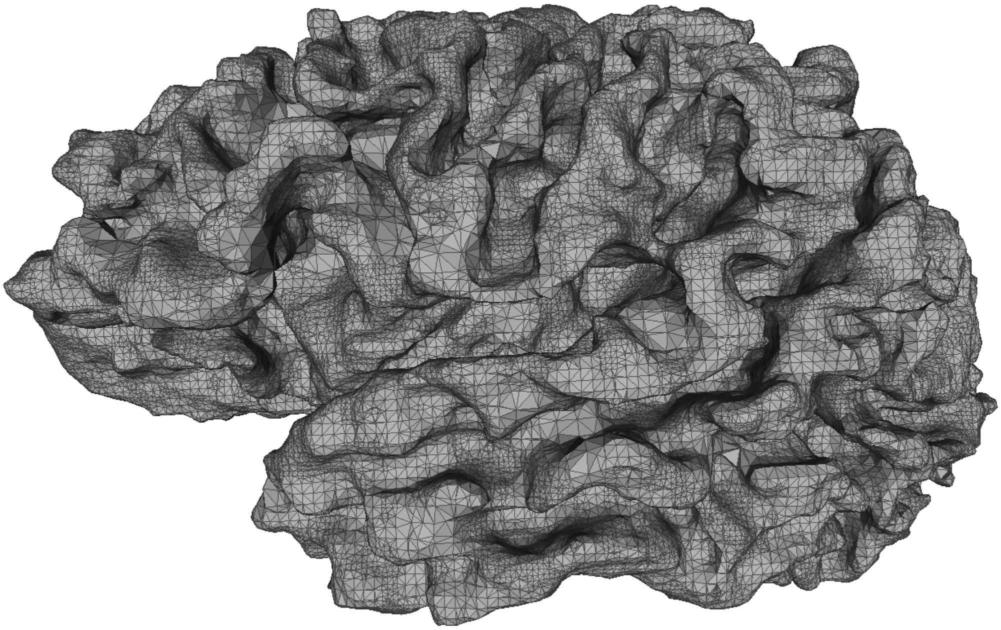

Figure 4.17: Final reconstructed surface. The reconstruction was performed considering the intersection of mean and intrinsic curvature information for the peaks detection and a peak neighbouring size of 5 rings. The faceted profile of the original surface is completely smoothed, highlighting the underlying cortical folding pattern.

ratio, while the edge and aspect ratio were increased after reconstruction. Sharp peaks are characterized by extremely close vertices in the neighbourhood of the singularity, with a prevalence of flattened triangles. From Section 4.3.2 we know that a flattened triangle has an angle close to π. Logically, the presence of mesh singularities leading to surface peaks will translate into higher mean angle ratios. Equivalently, as the vertices in the neighbourhood of the peaks are close to each other, the final edge ratio of the mesh will be smaller in the presence of spikes and will increase once the singularities are removed.

The radius ratio ρ is minimal only for an equilateral triangle. It is used to test the regularity of the mesh elements. For a triangular mesh, higher values of ρ indicate the presence of needles or flattened in the triangulation. Results displayed in Table 4.2 reports a considerable decrease of the radius ratio with respect to the original mesh, indicating a less irregular surface tesselation. In all cases, the reconstructed surface presents an increase of the aspect ratio when compared to the original triangulation. This result indicates a reduction of small angles, thus smaller number of needles in the triangulation.

4.4.1 Parameter choices

The mesh repairing approach presented here is based on two parameters that should be tuned to get optimal results: (1) the curvature used for the detection of mesh singularities and (2) the size of the neighbourhood to be removed. In the first case, the choice among the proposed curvatures was done based on the Hausdorff distance between the original and the reconstructed surfaces. Yet, the goal of this approach was to obtain topologically and geometrically correct surfaces, while being as close as possible to the original mesh.

Comparing the Hausdorff Distances obtained between the original surface and the reconstructed ones allows us to hypothesize that using the intersection of both curvatures (i.e. B curvature) provides a better peak selection, yielding closer-to-original surface reconstruction. Table 4.3 reports the Hausdorff Distance between the original surface of one subject and the reconstructed surfaces based on four different curvature information for different ring sizes. H stands for mean curvature and K is the intrinsic one. B is the intersection of both curvatures (i.e. $H \cap K$), while U is the union ($H \cup K$). By intersection we mean that only the vertices showing extreme values of H and K curvatures at the same time are retained as peaks, while the union indicates that a vertex is retained if H or K presented extreme values.

	Mesh	H	K	B	U
RH	*Ring size 4*	3.4442	3.8335	3.4447	3.8335
	Ring size 5	3.5735	4.3477	3.5756	4.3458
	Ring size 6	4.3350	5.1365	4.3351	5.1268
LH	*Ring size 4*	12.9387	14.5011	9.8201	14.5013
	Ring size 5	13.9312	14.4725	13.9306	14.4762
	Ring size 6	14.6564	14.6818	14.6563	14.6829

Table 4.3: Hausdorff Distance between the original surface mesh and the reconstructed ones using different ring sizes and curvature information. The first four rows correspond to the right hemisphere cortical surface (RH) while last four rows correspond to the left one (LH).

Neither the intrinsic nor the mean curvature, by themselves, capture the intuitive notion of "local shape". One needs both to construct the initial second order part of the Taylor series expansion (Koenderink & van Doorn, 1992).

The optimal peak neighbouring size (*aka.* ring size) was chosen by mapping the evolution of the mesh quality metrics while increasing the size of the neighbourhood. Albeit the algorithm seeks for correcting all possible singularities in the reconstructed surface, increasing the ring size implies removing more vertices, yielding to lower precision of the reconstruction. On top of that, increasing the ring size directly translates to an increase in the computational load, forcing the choice of the best setting for the reconstruction to be a trade-off between geometrical goodness of the reconstruction and computational load.

The evolution of these quality measures with respect to the ring size is shown in Fig. 4.18. We report only this evolution for the surfaces reconstructed using both the mean and intrinsic curvature for on subject hemisphere. Nevertheless, the same trend was observed in the other subjects.

As expected, the angle ratio and the edge ratio presented the same trends, decreasing while the ring size increases. Yet, though the differences are almost imperceptible when comparing these two measures, the radius ratio and the aspect ratio did show considerable differences. In both cases, the measures increased while increasing the ring size up to an inflection point when considering the $5_{th} - ring$ neighbourhood for peak removal. From this point, increasing the ring size translate in a drop of these two measures (see Fig. 4.18).

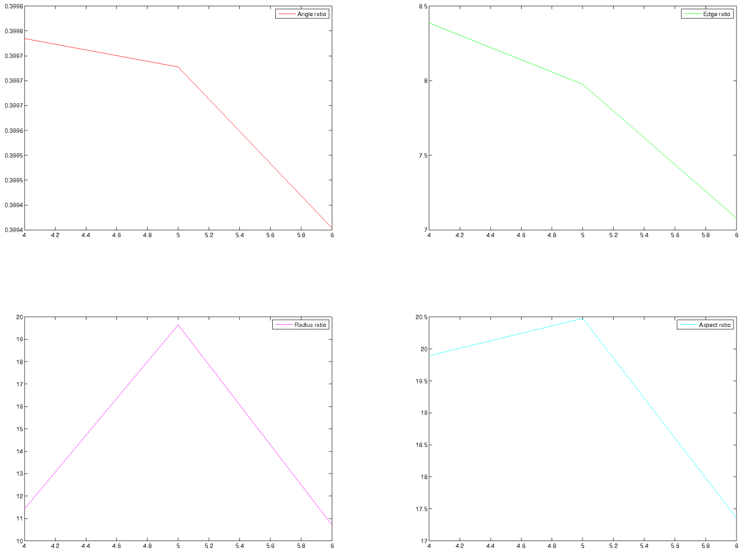

Figure 4.18: The evolution of quality measures with ring size for the reconstructed surface of the right hemisphere of one subject.

4.5 Potential improvement of the algorithm

Some improvements can be done to the approach presented in this chapter, in order to increase the accuracy of the reconstructed cortical surface, mainly in the peaks detection. Indeed, it may be highly interesting to adapt the peak neighbouring search to the size of each particular spike on the surface. In the current approach, the neighbouring vertex search imposes the same ring size for all peaks in the mesh. Yet, an interactive search allowing for different ring sizes, depending on the initial node seed, may yield more accurately repaired mesh.

We performed a preliminary analysis, using the Dijkstra algorithm to compute distances between neighbouring vertices. Fig. 4.19 and 4.20, show different trends in vertex distance distribution depending on the seed node. While for a standard vertex the distance between the seed node and the vertex belonging to the enhanced neighbourhood increases exponentially with the ring size, distance from a spike present an inflection point, giving the size of the ring that should be ideally removed. The same behaviour was observed when plotting the distance histogram (see Fig. 4.20).

Other surface reconstruction methods should be tested. The SSD algorithm (Calakli & Taubin, 2011) outputs a new mesh, ideally with no self-intersections or other degeneracies. However, if all spikes have not been perfectly removed, a new component may appear in the reconstruction, as the SSD approach uses dual marching cubes to construct a mesh with no constraints on the topology of the surface. Indeed, SDD is an implicit method for surface reconstruction. Yet, in such cases where the filtered point cloud presents some inconsistencies, it might be preferable to use an explicit representation.

4.6 Discussion and conclusions

In this chapter we have presented an approach to repair triangulated surfaces of the cerebral cortex, which is completely independent from the underlying segmentation. It needs no other information than the triangle mesh itself. It is a fully automated technique, which converts an inconsistent input mesh into an output mesh that is guaranteed to be clean and consistent, and represents the closed manifold surface of the cerebral cortex of one hemisphere.

The algorithm removes all typical mesh artefacts such as degenerate triangles, non-manifold vertices and edges and overlapping and self-intersecting triangles. Nearly all artefacts present on the cortical surface are eliminated, comprising the sharp peaks, nearly invisible artefacts likely to hinder subsequent operations like surface registration and parcellation. Access to topologically and geometrically corrected surface is necessary when processing is applied to the resulting mesh.

As seen in the beginning of this chapter, surface fairing methods are most often designed from the graphical point of view, with the only goal of improving mesh smoothness. These approaches generally lead to oversmoothing, which results in the loss of desirable geometric features in the surfaces. While they have been extensively used in the computer science field, they barely generalize when handling clinical data. Indeed, they only focus on creating meshes of correct topology, disregarding the geometry of the resulting triangulation.

The main contribution of the work presented in this chapter is a surface repair approach that provides surfaces correct both in the topological and the geometrical sense. The reconstructed surfaces, which present a correct topology, are tested for geometrical inconsistencies using a

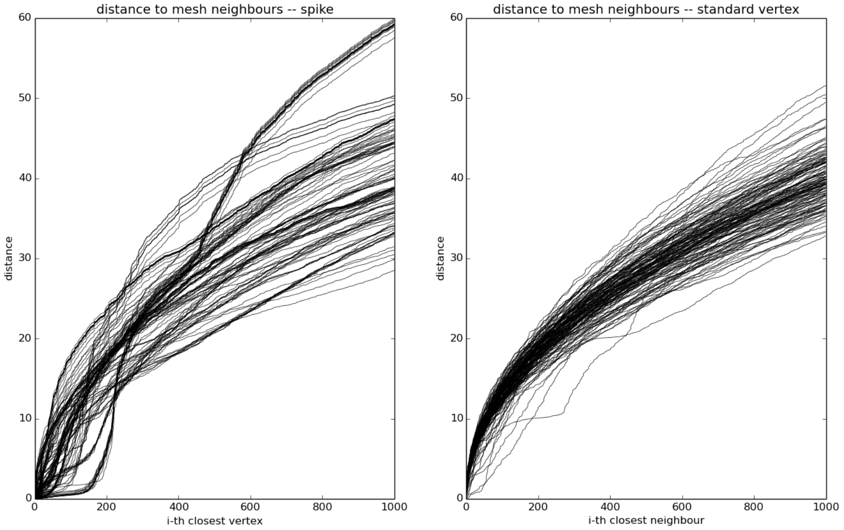

Figure 4.19: Distance growth for vertices considered spikes (left) and standard vertices (right).

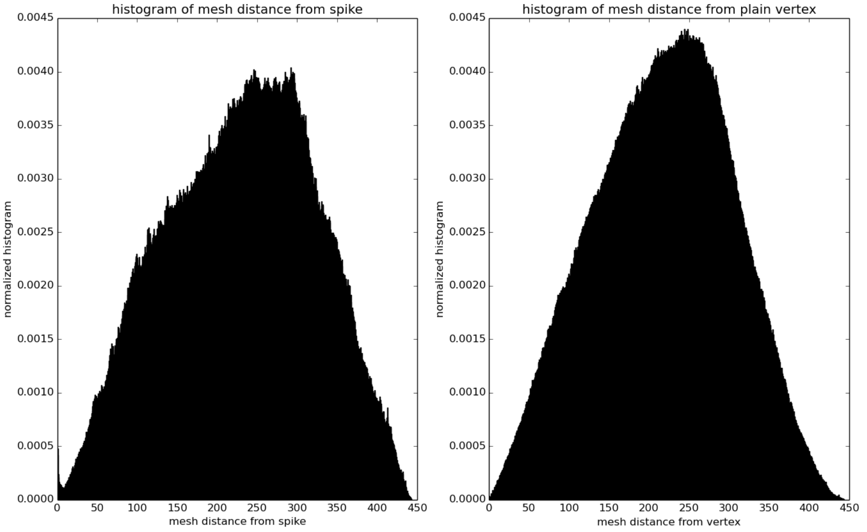

Figure 4.20: Distance histograms for vertices considered spikes (left) and standard vertices (right) .

combination of extrinsic and intrinsic curvature information. These singularities are then removed together with the vertices belonging to their close neighbourhood, a process resulting in the elimination of nearly degenerate mesh elements.

The resulting watertight surface is then constructed using an implicit reconstruction algorithm preserving both the shape and the boundaries of the surface, without loosing the topological and geometrical attributes required for the subsequent processing steps. Surfaces are validated topologically and geometrically by means of commonly used measures and the best parameters are estimated on the basis of the evolution of these measures along different settings.

The final reconstructed surfaces will be the input to the registration and parcellation scheme that we present in the next chapter, allowing the detection of cortical regions on the newborn cortical surface in a fully automated fashion.

5

Parcellating Newborn Cortical Surface

In their work, Tymofiyeva and colleagues (Tymofiyeva *et al.*, 2014), describe the two most critical steps to construct the newborn connectome (as for all connectomes) as: “(i) choosing connectivity measures that will serve as the network “edges” and (ii) finding an appropriate way to divide the brain into regions that will serve as the network “nodes” (Tymofiyeva *et al.*, 2014)”.

Indeed, one challenge when estimating the human connectome (independently of the subject’s age) is the determination of the anatomical partition of the cortical surface. This estimation strongly relies on the choice of a convenient subdivision of the cortical surface (and subcortical structures), or equivalently, the choice of the network nodes. This choice is not obvious and can impact the results of the final connectivity analysis (Meskaldji *et al.*, 2013).

Some attempts to partition the newborn cortical surface have been made using either equally sized regions or anatomical regions, with unclear relationship to the underlying functional organization of the brain (Tymofiyeva *et al.*, 2012). However, it is highly desirable to parcellate the brain into functionally distinct brain regions with distinct architectonics, connectivity, function, and/or topography (Felleman & Van Essen, 1991). Indeed, an accurate parcellation allows each node in the macroscale connectome to be more informative by associating it with a distinct connectivity pattern and functional profile.

Such a parcellation of localized areas of the cortex based on brain function and/or connectivity has been accomplished using diffusion tractography and functional connectivity (Beckmann *et al.*, 2009), by non-invasively measuring connectivity patterns and defining cortical areas based on distinct connectivity patterns (see (Cloutman & Lambon Ralph, 2012) for a review). Such analyses may best be carried out on a whole brain and by integrating non-invasive modalities. However, it would be desirable to have each node corresponding to a functionally and anatomically coherent area, potentially homogeneously affected in case of pathology.

A typically chosen approach to define a brain network’s nodes is to register the brain MRI to some anatomical template (or atlas). The Automatic Anatomical Labeling (AAL) (Tzourio-Mazoyer *et al.*, 2002), which partitions the cortical and sub-cortical volumes into 90 regions approximating the Brodmann areas[1], is generally the preferred choice. Nevertheless, atlas-based

---

[1] A Brodmann area is a region of the cerebral cortex, in the human or other primate brain, defined by its cytoarchitecture, or histological structure and organization of cells. They were originally defined and numbered in 1909 by the German anatomist Korbinian Brodmann based on the cytoarchitectural organization of neurons he observed in the cerebral cortex using the Nissl method of cell staining.

approaches are generally limited by the inter-subject variability and can be especially problematic in the context of brain maturation and neuroplasticity (brain restructuration after damage).

However, pure atlas-based approaches suffer from the so-called brain atlas concordance problem. This concept, introduced by Bohland et al. (Bohland *et al.*, 2009), considers the effect that even if multiple different methods exist for partitioning the brain into a discrete set of anatomical regions (parcellating), no widely accepted standard exists for partitioning the cortex and subcortical structures, or for assigning labels to the resulting regions. This concordance problem has been traditionally seen as a nomenclature problem, as multiple distinct terms are often used to refer to the same anatomical or functional brain structure and vice versa. Yet, spatial relationships between sets of defined regions are not always apparent. As Destrieux et al. assess in (Destrieux *et al.*, 2010), anatomical cortical description is a matter of convention: depending on the chosen number of parcellating units and their respective limits, several parcellation schemes may be defined, and the same anatomical label may correspond to a parcellation unit whose boundaries vary in different conventions.

Albeit this limitation, what remains clear is that the precise localization of sulco-gyral structures of the human cortex is important for morphofunctional studies (Destrieux *et al.*, 2010). As seen in Chapter 4, Section 4.1.1, the folds of the cerebral cortex are formed during fetal and early childhood development following a precise pattern of emergence, with identifiable sulcation landmarks appearing according to gestational age (Garel *et al.*, 2001; Toews *et al.*, 2012). Thus, the cortical sulcation pattern appears as a less-variable feature for establishing correspondences between homologous anatomical regions. Although the cortical sulci formation is a complex process starting at 14 weeks of gestation that can potentially be influenced by underlying mechanisms of distinct origin (genetic, epigenetic, mechanical or environmental) (Dubois *et al.*, 2014), what seems clear is the existence of elementary cortical folds, the sulcal roots, known to be particularly stable across individuals (Cachia *et al.*, 2003). The sulcal roots are the locally deepest regions of major sulci, thought to be the first cortical folds to develop and closely relate to functional areas. As they show great spatial invariance, they appear to be extremely useful as stable anatomical landmarks (Im *et al.*, 2010).

Several methods achieve sulcal basin identification based on learned shape and neighbourhood statistics (Riviere *et al.*, 2002; Tao *et al.*, 2002; Tu *et al.*, 2007). Other methods are characterized by a hybrid approach using subject-to-template registration and local classification based on cortical folding patterns (Desikan *et al.*, 2006; Fischl *et al.*, 2004). In the case of adult MR images, the most widely used method for automatically labelling the cortical surface is the approach included in the FreeSurfer package (FS). FreeSurfer (Fischl, 2012), is an open-source set of tools for automated cortical surface and volume reconstruction together with an automated tissue labeling developed at the Martinos Center (MA, USA) [2]. It allows for (1) measuring various morphometric properties of the brain such as cortical thickness and curvature characteristics and (2) computing inter-subject cortical spatial normalization based on aligning an individual's cortical folding pattern to a population-averaged atlas. However, as its atlas is also based up on an adult training data set, it cannot be used for the analysis of newborn MRI.

5.1 Context and Motivations

Several automated cortical delineation protocols have been proposed in recent literature. The main advantage of these automated methods is that they do not require user interaction or neu-

---

[2] https://www.martinos.org/lab/lcn at the moment of this thesis dissertation.

roanatomical expertise. They are suitable for large-scale studies involving a large number of subjects and have the benefit of removing part of the inter-subject variability. However, in all cases, these methods require the data first to be transformed to a common coordinate system in which anatomical structures are aligned. In other words, the accuracy of these parcellation methods strongly relies on the accuracy of the *registration* procedure used.

5.1.1 Some words on registration

Registration is the spatial alignment to properly integrate useful information from separate images. Given a reference and a template image, its goal is to find a transformation such that the transformed template is as similar as possible to the reference image. In other words, image registration maps *homologous* points of different images representing the same object.

For automated image registration, the image's "homology" is commonly substituted by a measurable criterion of image dissimilarity, which is to be minimized (Zosso *et al.*, 2011). Depending on the images to be registered, different metrics are used to assess image dissimilarities. In modo-modal registration[3] (when one can assume that both images differ only by a geometric transform and an independent Gaussian noise on the intensities), the sum of the squared intensity difference (i.e. the squared error metric) is the preferred choice. In the multi-modal case other metrics such as the Kullback-Leibler distance or Mutual Information are more appropriate (Rueckert *et al.*, 1999; Wells III *et al.*, 1996).

Registration methods mainly differ in the deformation model and constraints applied to the resulting deformation field. Simple transformations, like *rigid* or *affine* ones, are defined globally for the whole image space. They can be represented by a small number of parameters (resp. 6 and 12 in 3D), restricting the degrees of freedom of the transformation. Nevertheless, considering the high variability of the human brain cortex, a "model-free" deformation allowing for individual (local) displacement of each point in the image domain may be preferable. However, one should restrict such free-form deformation fields to a physically meaningful deformation, by introducing some constraints on the field regularity.

Given a *fixed image* $F(\cdot)$ and a *moving image* $M(\cdot)$, "free-form" (formally, *non-parametric* or *non-rigid*) image registration aims at finding the displacement of each pixel so as to get a reasonable alignment of the images (Vercauteren *et al.*, 2009). Nevertheless, over the space of non-parametric transformations, registration is an ill-posed problem which results in ill-conditioning, instability of solutions and highly non-convex cost functions. Undeniably, a simple optimization of the similarity criterion of the two images alone leads to unstable and non-smooth solutions.

In order to deal with this instability of the energy function to be minimized, a regularization term is often introduced. Due to the introduction of this regularization term, image registration is also known to be an *optimization problem*, whose cost function comprises an *image dissimilarity term* and a *regularization term* which is normally assumed to be smooth. This regularization term is an additional penalty term that penalizes undesirable transformations, but it can be also used to add some a priori information such as underlying tissue properties. Image distance metric and regularization penalty are commonly incorporated into a single energy minimization, with its most general formulation as:

$$E = E_{similarity} + \lambda E_{regularization} \tag{5.1}$$

---

[3] In mono-modal registration the images to be registered are acquired with the same sensors leading to similar image intensities through the whole image.

where λ controls the amount of regularization needed. Two main approaches can be distinguished for all registration methods: *voxel-based* and *feature-based* approaches.

In the first case, various approaches have been proposed such as intensity-based non-rigid registration in the voxel space (Rueckert *et al.*, 1999; Vercauteren *et al.*, 2007). Tough intensity-based non-rigid registration works well in intra-subject registration, the aligned cortical folds do not usually match well. Indeed, in such cases these methods may not effectively address the issues arising from the variability across populations (Acosta *et al.*, 2012).

Feature-based approaches are landmark-based or segmentation-based. In both cases, identifiable anatomical elements need to be extracted in both reference and moving images, and their correspondence determines the registration transformation. A large variety of model-based registration, using high-level anatomical information (sulcal lines, functional surfaces, etc.) have been proposed (Collins *et al.*, 1998; Narayanan *et al.*, 2005; Ou & C., 2009; Thompson & Toga, 1996; Vaillant & Davatzikos, 1997; Van Essen *et al.*, 2000; Vercauteren *et al.*, 2009; Zöllei *et al.*, 2010) (see (Klein *et al.*, 2009) for a evaluation of several non-linear deformation methods). However, due to the highly irregular structure of the reconstructed cortical sheet meshes, it is challenging to align cortical surfaces.

Projection of the cortical surface on a spherical manifold is common, preserving both topology and connectivity (Fischl *et al.*, 1999a,b; Hebert *et al.*, 1995; Zosso *et al.*, 2011). Mesh inflation allows coarse registration and gives rise to spherical feature maps, either after inflation (Fischl *et al.*, 1999a,b) or conformal mapping (Angenet *et al.*, 1999). The registration process using these spherical surfaces is driven by the features embedded on them such as surface normals, curvature, geodesic distances to crown vertices, as well as anatomical features like cortical thickness or sulcal depth.

In a first approximation, the flattening of local sections of spherical parametrizations into a 2D representation allows using classical 2D image registration methods. However, this procedure introduces major irregular dilations and contractions (Zosso *et al.*, 2011). Yet, this procedure is carried out only after several incisions have been made in the cortical surface to allow it to lie flat without major distortion. This is problematic, as the resulting surface does not respect the topological structure of the original cortical surface; neighbouring points on the surface that lie on opposite sides of a cut may have very different locations on the flattened surface. Inded, the exact position of the incisions can greatly affect the resulting registration (Fischl *et al.*, 1999b).

Bruce Fischl and colleagues developed in (Fischl *et al.*, 1999b) a spherical-based coordinate system adapted to the folding pattern of individual subjects. In their work, they generate an average folding pattern across a large number of individual subjects as a function of the unit sphere and of non-rigidly aligning each individual with this average. The FreeSurfer registration method is a surface-, landmark-based method. It is not a pure curvature minimization method, but rather tries to minimize image distortion such that the final surface have minimal folding (Fischl *et al.*, 1999b; Fischl, 2012).

Based on the spherical feature maps introduced by Fischl and colleagues, Yeo et al. (Yeo *et al.*, 2010) proposed the *Spherical Demons* registration framework (SD), which extends the *Diffeomorphic Demons* (Thirion, 1998; Vercauteren *et al.*, 2009) algorithm to the sphere. Spherical Demons (SD), i.e. the spherical variant of the Demons non-parametric registration algorithm, exploits spherical vector spline interpolation theory and efficiently approximates the regularization of the Demons objective function via spherical iterative smoothing.

The Demons algorithm was first introduced in 1998 by Thirion. In (Thirion, 1998) he proposed to consider non-rigid registration as a diffusion process. He introduced in the image entities (*aka.* demons) that push accordingly to local characteristics of the images. These forces, inspired from the optical flow equations, are actually an approximation of a second order gradient descent on the sum of square intensity difference regularity criterion (Pennec *et al.*, 1999).

One of the main limitations of the Demons algorithm is that it does not provide diffeomorphic[4] transformations. Yet, a diffeomorphic deformation preserves the topology of the image and prevents it from folding, even at large deformations. Moreover, inversibility of the deformation field is an essential property when it comes to rendering the registration process inverse consistent or even symmetric (Rogelj & Kovacic, 2006). In (Vercauteren *et al.*, 2009), the Demons algorithm was extended to a diffeomorphic setting. Both, Freesurfer and Demons (in its original and spherical version) are the state-of-the-art methods for automatic surface-based non-rigid registration. Both are very popular and are broadly used in group analyses due to their robustness and accuracy.

In this work we use FreeSurfer's registration approach (from now on FS registration). More specifically, we use the the `mris_register` algorithm. Although both, FS and SD methods are appropriate for the spherical registration task, the decision was made based mainly on two facts. On the one side, the 6 years-old scans were already processed using the FreeSurfer stream and we wanted the procedure to be less dependent on the possible bias introduced by using different registration procedures for each time-point.

More importantly, we wanted to exploit one interesting characteristic of FS registration. As we will detail in the next chapter, the final similarity measure used for the registration in FS is weighted by the variance of the convexity across subjects at each location and integrated over the entire cortex (Fischl *et al.*, 1999a). The use of this variance of convexity gives greater effect on the registration procedure to highly consistent folding patterns such as the Sylvian fissure and the central sulcus with respect to more variable patterns (Pantazis *et al.*, 2010), an appealing property considering our hypothesis on cortical folding formation[5].

5.1.2 Motivations

As seen in the introduction of this chapter, the folds of the cerebral cortex are formed during fetal and early childhood development following a precise pattern of emergence, with identifiable sulcation landmarks appearing according to gestational age (Garel *et al.*, 2001; Toews *et al.*, 2012). Albeit the cortical sulci formation is a complex process starting from 14 weeks of gestation onward that can potentially be influenced by underlying mechanisms of distinct origin, the sulcal lines are considered as the most robust landmarks of the human cerebral cortex (Cachia *et al.*, 2003; Im *et al.*, 2010; Kersbergen *et al.*, 2014).

The convolutions of the cortical sheet are very complex but by no means entirely random. There seems to exist a common "base-model" for the human cortex, which is then modulated by the individual basis. Thus, when trying to register images of the same subject at different time points, one can cast aside the inter-subject variability (or the abnormal growing if the gap is big

---

[4] By definition, a diffeormorphism is an invertible deformation that maps one image to another such that both the deformation and its inverse are smooth (differentiable).

[5] As seen in Chapter 4, Section 4.1.1, the Sylvian fissure and the central sulcus appear first in development and are the most stable structures across individuals.

enough), and assume the differences of both images to be due to the acquisition process only.

In this chapter we use the original FS registration algorithm to align one subject surface extracted at two different time-points: term equivalent age (TEA) and 6 years of age. The main goal of this registration step is to provide both surfaces in the same referential by taking advantage of the longitudinal evolution of the cortical surface from early to late childhood. This registration will then assist the parcellation of the newborn cortex. Indeed, as seen in section 4.1.1 newborn present, at term, an "adult-like" cortical surface. Thus, one might expect that both surfaces will differ only on a certain factor of scaling, while the localization of the main sulci and gyri will remain stable across lifespan, making the registration procedure possible.

Based on this hypothesis, and using the newborn surfaces automatically reconstructed in the previous chapter, we propose an atlas labelling scheme of the newborn cortical surface. For each subject, the 6 years-old's surface is selected as a target to which the newborn surface is coregistered. As already mentioned in the introduction, to properly achieve the registration task, the target for registration should be the least biased in relation to the population under study. Indeed, the main strength of the analysis proposed in this chapter is given by the longitudinal dataset. Here, the registration task is performed over two acquisitions of the same subject, which diminish the bias due to the use of templates and atlases. Both surfaces are previously inflated to a sphere, and the registration procedure is driven by the mean curvature of the surface, based on the fact that the sulcal pattern in both surfaces is essentially the same. Two different approaches are tested for the cortical structure delineation: (1) subject-to-subject mapping and (2) subject-to-average mapping. Both will be compared to the original FreeSurfer labelling procedure.

5.2 Material and Methods

5.2.1 MR brain data

In this chapter we use a longitudinal set from the Geneva and Lausanne University Hospitals. As described in Chapter 4, Section 4.3.1, subjects under study underwent MR examinations at birth (time-point 1, *TP1*), at term equivalent age (time-point 2, *TP2*) and at six years-old (time-point 3, *TP3*). In this chapter we use TP2 and TP3 acquisitions. The choice of using only these two time-points was based on the equivalence of the sulcal patterns among the two acquisitions, as the cortical folding patterns at TEA is the same as than at 6 years of age, which is not the case for TP1.

The same four subjects as in the previous chapter are considered, based on the newborn dataset described in section 4.3.1. Subjects 1 and 2 were born moderately premature at 33 weeks GA and diagnosed for IUGR. Both were first scanned 12 days after birth (TP1) and 6 weeks after birth (TP2). Subjects 3 and 4 were born preterm at 29 weeks GA without prenatal restriction. They were first scanned 11 days after birth (TP1) and 11 weeks after birth (TP2).

5.2.2 Surface inflation, flatting and projection onto a sphere

At 6 years of age brain structures are fully comparable to the adult ones. Consequently, TP3 images can be straightforward processed using the FreeSurfer's (FS) *recon-all* pipeline[6](Fischl

---

[6] See https://surfer.nmr.mgh.harvard.edu/fswiki/recon-all (at the moment of this thesis) for the overall FS cortical reconstruction and labelling process.

et al., 2004). In FS software, the reconstruction of the cortical surfaces procedure is broken into a number of subtasks. First, intensity variations due to magnetic field inhomogeneities are corrected and a normalized intensity image is created. Next, extracerebral voxels are removed, using a "skull-stripping" procedure. The intensity normalized, skull-stripped image is segmented based on the geometric structure of the gray-white interface. Cutting planes are then computed that separate the cerebral hemispheres and disconnect subcortical structures from the cortical component. This generates a preliminary segmentation that is partitioned using a connected components algorithm. Any interior holes in the white matter components are filled, resulting in a single filled volume for each cortical hemisphere. Finally, the resulting volume is covered with a triangular tessellation and deformed to produce an accurate and smooth representation of the gray-white interface as well as the pial surface. The resulting surfaces are inflated in an area-preserving transformation and subsequently homeomorphically transformed to a sphere (Fischl *et al.*, 1999a)

For TP2, we use the surfaces obtained in Chapter 4 and, similarly to the 6 years-old case, we map them onto a sphere using FS. However, in order to use FS commands, the newborn surface's tesselations reconstructed in chapter 4 (stored as a set of vertices and corresponding faces) are converted to *ASCII* format using the `write_freesurfer` command. The resulting tesselation is then mapped onto the unitary sphere in two steps using the `mris_inflate` and `mris_sphere` FS-commands.

The inflation step is an intermediate step that "unfolds" the surface providing an alternative to expose hidden sulci and to simplify the geometry for cortical mapping to a sphere (Acosta *et al.*, 2012). This inflation procedure preserves the global shape of the surface at a coarser level and simplifies the determination of shape correspondences when mapping to the sphere. We perform 55 iterations (the default setting) and set the metric distortion/smoothness trade-off to 0.1. This term controls the relative strength of the metric preserving term in the cost function versus the smoothing term. The resulting surfaces are then mapped to the sphere using 3000 iterations of the `mris_sphere` command. After the spherical transformation, there is a one-to-one mapping between faces and vertices of the surfaces in the native geometry and the sphere.

5.2.3 Registration scheme

The problem now is reduced to registering the corresponding surfaces of the target and moving scans in the spherical space, while maintaining the correspondence between each face on the registered sphere and each face from the native geometry[7]. Roughly, the registration is performed by shifting vertex positions along the surface of the sphere until there is a good alignment between moving and fixed spheres with respect to certain degree of the cortical folding patterns. As the vertices move, the areal quantities assigned to the corresponding faces are also moved along the surface.

Thus, as the registration is based on the cortical folding patterns, before registering the surface we first recompute the curvature measures from the reconstructed tesselation. We computed both the mean and intrinsic curvatures using the FS `mris_curvature` command applying 10 smoothing iterations prior to the computation.

In FS, the alignment of the cortical surfaces is carried out by minimizing the squared difference between the average convexity (Fischl *et al.*, 1999b) across a set of subjects (the cortical

---

[7] A registration method that produces a smooth, i.e. spatially differentiable, warp function enables the smooth transfer of areal quantities.

atlas) and that of the individual subject. The squared error is weighted by the variance of the convexity across the subject at each location and integrated over the entire cortex (Fischl *et al.*, 1999a). Here, instead of considering the FS cortical atlas based on adult populations, we define our own atlas by (1) considering the subject's 6 years-old counterpart and (2) averaging the surfaces of the 6 year-old time-point.

In the first case the registration is straightforward as no "template" needs to be constructed first. We register the newborn surface to its corresponding 6 years-old counterpart using the `mris_register` command. Setting the flag -1 in the command line allows treating the target argument as the name of a single subject's surface instead of a template file. The resulting registration file is stored as a canonical surface named `(r/l)h.sphere.reg` [8]. Vertices' locations in the resulting `.reg` surface show how each vertex needs to be positioned to align the subject's curvature data to the chosen template.

We also build a dedicated atlas from our 6 years-old surfaces using the `mris_make_atlas`. The inputs are the four 6 year-old spherical surfaces previously processed using the whole FS recon-all pipeline with their corresponding smoothed and inflated surfaces as well as their curvature informations and sulcal positioning (FS *.curv* and *.sulc* files). This process allows to calculate a mean pattern of curvature-related values across our 4 subjects along with the variance of these variables. As the original `mris_make_atlas` command expects the input subjects to be aligned (which is not the case), the process proceeds iteratively. We refer the reader to the FS website for a comprehensive explanation of this procedure.

We stored the resulting registration files as `(r/l)h.sphere2avg.reg`. In a third registration step, and in order to compare with previously proposed results, we also registered the newborn spherical surfaces to the FS adult atlas without any prior processing giving us the `(r/l)h.FSsphere.reg`.

5.2.4 Classification

The proposed registration scheme provides us with three different `.reg` files depending on the template used for the registration of the newborn surface. The final delineation of cortical labels, i.e. parcellation, is then performed by projecting both the registered feature maps and the *cortical labels maps* for each case into the respective subject space using the FS `mris_ca_label` command.

In the following sections we detail the main steps to build the cortical label maps and perform the classification. Yet, as in the registration case, we construct two different cortical label maps that will be used for the delineation: (1) single-subject atlas based on the 6 years-old cortical labels and (2) an "average" atlas from the available 6 year-olds' datasets. As a third step, and to illustrate the improvement of the parcellation task due to these two dedicated atlases, we also use the standard FS procedure, i.e., using an adult-based atlas.

5.2.4.1 Building the cortical labels maps

In (Desikan *et al.*, 2006), Rahul S. Desikan proposed a manual labelling of the cortical surfaces with 35 gyral units as shown in Fig. 5.1. For an exact definition of how the regions were delineated we refer the reader to the original paper (Desikan *et al.*, 2006).

---

[8] `r/l` stands for right and left hemispheres *resp.*

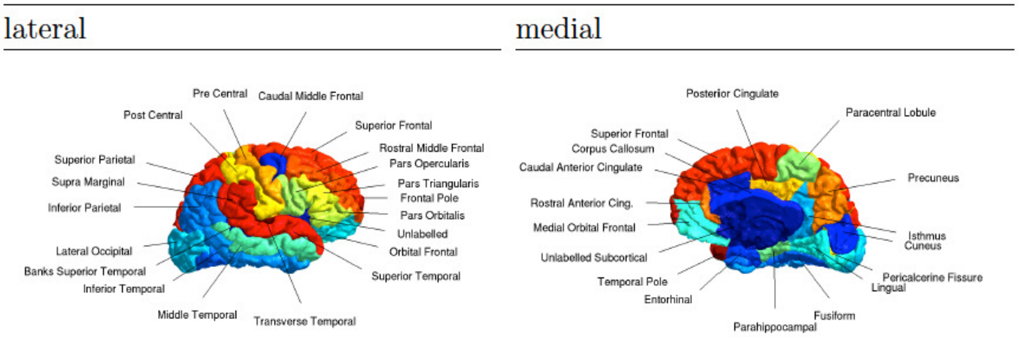

(a) pial

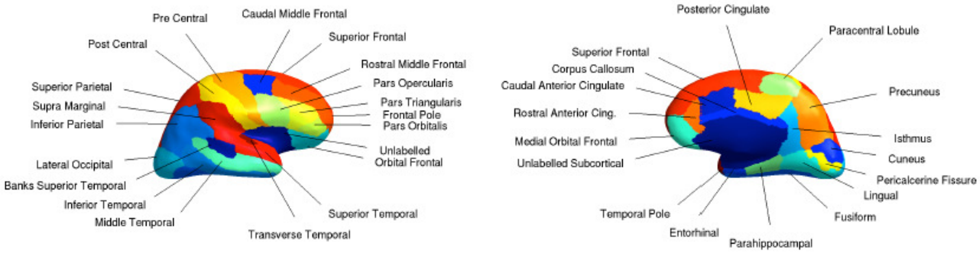

(b) inflated

(c) sphere

Figure 5.1: Manual parcellation scheme in the Buckner cerebral cortex dataset. The delineation was done manually in a sulcal approach, i.e., "tracing from the depth of one sulcus to another, thus incorporationg gyrus within" (Desikan *et al.*, 2006). The parcellation is shown both from a lateral and a medial view, as well as on (a) the pial surface, (b) the inflated surface and (c) the sphere. The pial view allows the easiest identification of the gyral regions, while the inflated surface reveals otherwise hidden buried structures, such as the banks of the superior temporal sulcus or the pericalcarine fissure. The spherical surface is the configuration which is actually used for registration and classification. Image reproduced form Dr. Dominique Zosso's thesis dissertation with personal approval.

.

This manual parcellation was done over a set of 40 adult scans. Yet, as seen in the introduction of this chapter, using an adult-based atlas for newborn population will lead to classification errors. Therefore, prior to the classification of the newborn cortical surfaces, 2 different cortical atlases are created using the `sphere.reg` and `sphere2avg.reg` obtained after the registration and the `mris_ca_train` command of FS. The `mris_ca_train` command creates a cortical parcellation atlas file based on one or more annotated[9] subjects.

The command `mris_ca_train` builds probabilistic information estimated from the 40 manually annotated subjects from (Desikan *et al.*, 2006). Here, we build two specific annotation[10] files, for (1) the pairwise registration setting (newborn-to-6 years) and (2) the subject-to-average registration scheme.

In the pairwise case we use the `(r/h).sphere.reg` and the annotation file from the 6 year-old subject as label atlas. We input these files to the `mris_ca_train` command together with the look-up file relating the labels with the surface name. This file is a *.txt* file that will be directly embedded in the atlas so the information can then be used for illustration purposes. In this case, we use the default file provided by FS and know as `colortable_desikan_killiany.txt`. The `mris_ca_train` provides us with a `.gcsa` (Gaussian classifier surface atlas) file, which stores the region label probability data at standard grid locations at two different scales of grid (`subj#_my_atlas.gcs`).

The atlas for the newborn-to-average case (`average_my_atlas.gcs`) is created similarly, though this time the four 6 year-old's spherical surfaces previously processed using the whole FS pipeline are used with their corresponding annotation files, as well as the `(r/h).sphere2avg.reg` file. Formally, the atlas is created by retaining information about each parcellation unit at each point in space. Yet, given the atlas function f and a group of N parcellated subjects, the prior probability of the parcellation label occurring at each atlas location is calculated independently of the other locations.

5.2.4.2 Bayesian classification approach

After pairwise and subject-to-average registrations and once the atlas has been constructed, we use the established spatial relationships to project the feature maps and the parcellation schemes into the respective subject space, allowing for a delineation of cortical regions in the newborn cortex. Here we use the Bayesian approach proposed in (Fischl *et al.*, 2004), as it allows for an explicit incorporation of prior information into the parcellation.

The main idea is to formulate the conditional probability of a parcellation P given a surface model S in terms of the conditional likelihood of S *given* P and the prior probability of the parcellation. Formally, the problem of automatic labelling cortical gyri and sulci reads:

$$p(P|S) \propto p(S|P)p(P) \tag{5.2}$$

Eq. 5.2 relates the probability of a parcellation P given the surface S to the probability of the geometry of the surface model occurring given a certain parcellation, together with the prior probability of the segmentation. In order to determine a *maximum a posteriori* (MAP) estimate of the parcellation P we thus need to define both the (i) likelihood model $p(S|P)p(P)$, were S is the observed geometry of the subjects surface and (ii) a prior model for the parcellation $p(P)$.

---

[9] "Annotation" is synonymous with "parcellation"

[10] An annotation file contains the labels of a surface, for example the sulci and gyri labels of a cortical surface.

Assuming the noise at each vertex to be independent from all other vertices, then we may rewrite the global likelihood of the geometry as the product of the local probabilities at each single vertex:

$$p(S|P) = \prod_{i} p(G_i|P(x_i)) \tag{5.3}$$

were G_i denotes the local observation of the surface geometry at vertex x_i. In (Fischl *et al.*, 2004), the local observation of the surface geometry , i.e., the *local feature vector* $\mathbf{G}(\mathbf{r})$, is composed respectively by the *average convexity* and the *mean curvature*. From there, the geometrical feature vector probability, i.e., the likelihood of observing the surface geometry $\mathbf{G}$ given the parcellation label $P(\mathbf{x})$, is modelled as a Gaussian, of which the mean vector $\mu_c(\mathbf{x})$ and the covariance matrix $\Sigma_c(\mathbf{x})$ are estimated directly from the available labelled set of subjects.

$$P(G_i|P(\mathbf{x}) = c) = \mathcal{N}(G_i|\mu_c(\mathbf{x}), \Sigma_c(\mathbf{x})) \tag{5.4}$$

The parcellation prior is defined assuming that the spatial distribution of labels can be approximated by an anisotropic non-stationary Markov random field (MRF), reducing the dependency of the local labels from all other labels in the map to the first order neighbourhood. This restriction permits the probability of the entire parcellation to be rewritten in terms of its neighbourhood (*viz.* clique potentials), using the Hammersley-Clifford theorem and by introducing Gibbs distributions.

5.2.4.3 MAP estimate

To make the maximum-a-posteriori (MAP) estimation of the proposed MRF computationally tractable, in (Fischl *et al.*, 2004) the authors use the iterated conditional modes (ICM) algorithm (Besag, 1986). The important advantage of ICM over other MRF solvers such as simulated annealing (Geman & Geman, 1984) is its extremely simple structure and fast convergence although it has been shown that ICM corresponds to instant freezing from a simulated annealing point of view (Besag, 1986).

We use the ICM model as described in (Fischl *et al.*, 2004) and initialize the parcellation with the MAP estimate assuming the probability of the label at each vertex, given its neighbourhood as being uniform. Then, the parcellation is sequentially updated computing the label $P(x_i)$ that maximizes the conditional posterior probability $p(P(\mathbf{x})|P(x_i), \mathbf{G}, \mathbf{x_i})$. The process is applied until no vertices are changed.

After this automated procedure, no further post-processing is carried out. None of the resulting cortical parcellation is manually edited neither.

5.3 Results

Here we present the results of applying the surface-based parcellation technique according to three different parcellation schemes. The first one is the pairwise parcellation using the same subject's surface reconstructed at two different time-points: (1) 6 year-old and (2) TEA. The second scheme, the subject-to-average scheme, is based on an averaged template constructed from the young children scans available. Indeed, we use this averaged label map to label the surface at TEA. In the third one, we used the standard FS procedure, i.e., the adult-based cortical map. The results are qualitatively evaluated by comparing the resulting cortical delineations with its 6 year-old's counterpart parcellation.

The pairwise automated parcellation scheme yielded a consistent cortical delineation in three out of the four subjects under study. In Tables 5.1 and 5.2 we show, for subject #1, the parcellation results on the white and inflated cerebro-cortical surfaces for both the right and left hemispheres.

Subject #1	White surface	
parcellation scheme	Right hemisphere	Left hemisphere
6 year-old	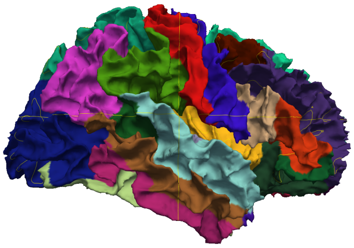	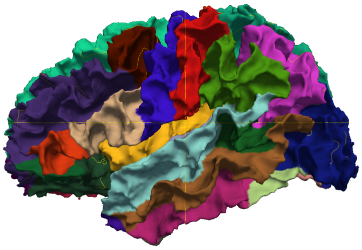
pairwise	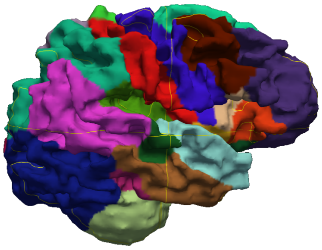	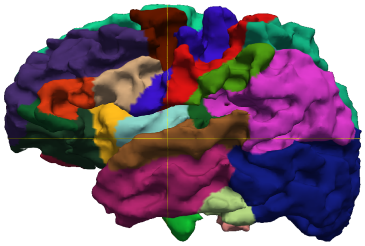
subject-to-average	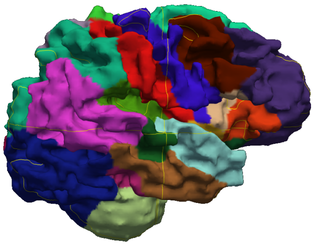	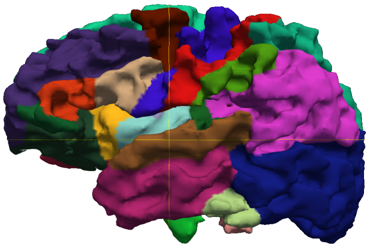
subject-to-adult (FreeSurfer)	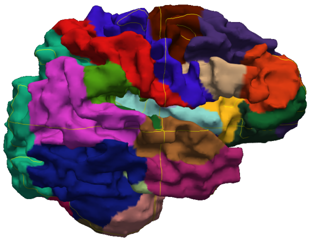	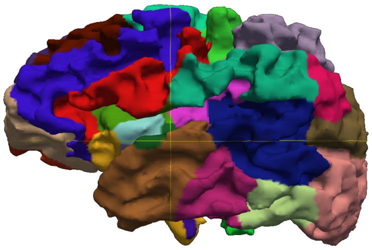

Table 5.1: Automatic parcellation for the same subject for each of the parcellating scheme presented compared to the 6 years-old counterpart obtained using FS standard procedure. Results are presented on the white surface. In each case, the first surface corresponds to the right hemisphere and the second one to the left hemisphere, respectively. The first row displays the parcellation of the 6 years-old cortical surfaces. The last three rows correspond to the parcellation of the same subject at TEA: the second row corresponds to the pairwise (subject-to-subject) scheme; the third one to the subject-to-average scheme. Last row present the results applying the FS standard procedure.

Subject #1	Inflated surface	
parcellation scheme	Right hemisphere	Left hemisphere
6 year-old	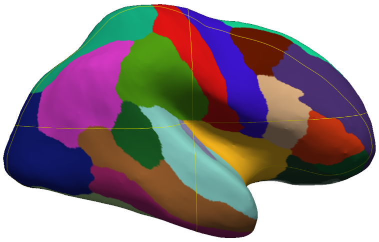	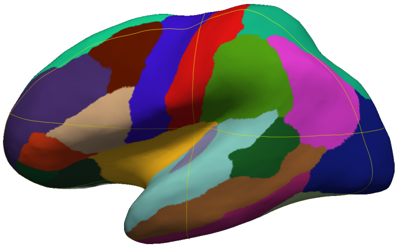
pairwise	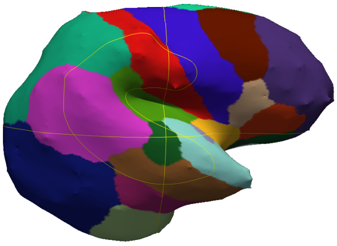	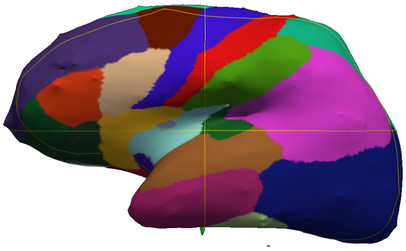
subject-to-average	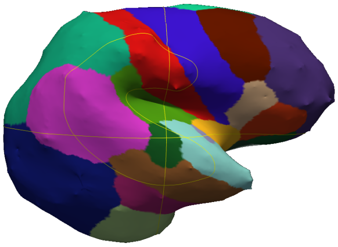	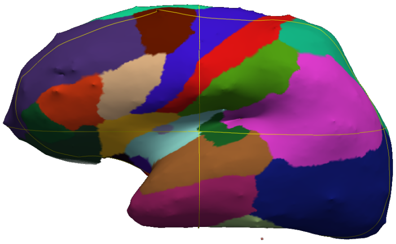
subject-to-adult (FreeSurfer)	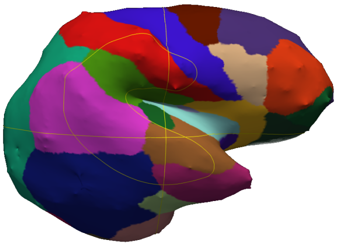	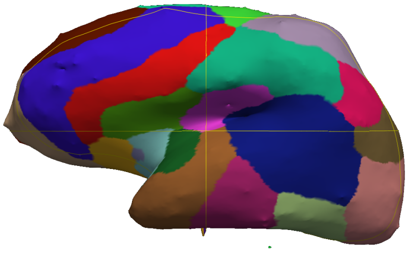

Table 5.2: Same parcellation results as in table 5.1, presented on the the inflated surfaces. Again, in each case, the first surface corresponds to the right hemisphere and the second one to the left hemisphere, respectively. The first row displays the parcellation of the 6 year-old's cortical surfaces. The last three rows correspond to the parcellation of the same subject at TEA: the second row corresponds to the pairwise scheme; the third one to the subject-to-average scheme. Last row present the results applying the FS standard procedure.

As we can see from the figures, cortical regions on the newborn are consistent with the 6 year-old's delineations mainly in the central and parietal regions of the cortex. These regions are mainly delimited by the central sulcus and the Sylvian fissure, highly consistent among individuals. The occipital and temporal regions are the ones showing lower correspondence. This lack of accuracy is especially evident in the fusiform and inferior and middle temporal cortical regions, and mainly in the right hemisphere. Indeed, one can see that the surface representing the right hemisphere contains part of the cerebellum which drives the registration towards a mismatch in the temporal regions. Nevertheless, the results obtained with both the pairwise and the subject-to-average registration provide much better results that the ones obtained with the FS standard procedure (see Fig. 5.1, last row).

While the white surface allows for an easier identification of the gyral regions, the inflated surface reveals otherwise hidden buried structures such as the banks of the superior temporal sulcus or the pericalcarine fissure. In Table 5.2, we show the same parcellation results, this time over the inflated surface. Here we can better appreciate how the pairwise and the subject-to average schemes yield to very similar results, with only some really light variations in the temporal cortical regions as well as in the pars orbitalis and pars triangularis. Indeed, the only difference between the two schemes is that the limits of each cortical region are smoother in the case of the subject-to-average, showing the effect of the average applied on the original labels.

What is clear from the two figures is that the standard FS procedure, based on adults templates, did not give an anatomically coherent parcellation. Although for the right hemisphere the results are close to be anatomically coherent for this subject, the left hemisphere, on the contrary, is mislabelled.

Similar results where observed for subjects #3 and #4. In Table 5.3, we present the worst results obtained, which belong to subject #3. We are just showing the results obtained with the pairwise scheme, as here again the subject-to-average scheme provided similar results with almost imperceptible differences. For this subject, as we can see in Table 5.3, the cortical delineations, especially on the left hemisphere, show inconsistencies in the occipital and temporal poles. On the contrary, the cortical regions obtained using the FS procedure were completely mislabelled (see last row of Fig. 5.3).

An accurate check of the outputs of each step of the procedure allowed us to detect the main reason of this inaccuracy. While for the rest of the subjects the original surfaces obtained from segmentation appeared pretty close to reality, the original surfaces for subject #3 were extremely faceted, especially for the left hemisphere, as we show in Fig.5.2. Yet, although the method presented in the previous section provided a smooth and clean surface, after the smoothing we lost some of the curvature information, specially in the Sylvian fissure (see Fig. 5.3).

Subject #3	Inflated surface	
parcellation scheme	Right hemisphere	Left hemisphere
6 years-old	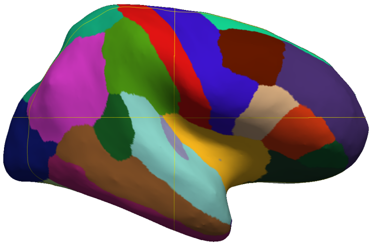	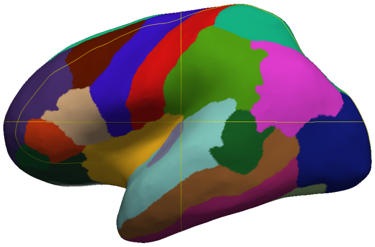
pairwise	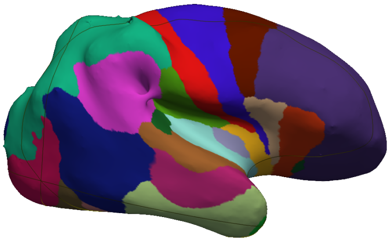	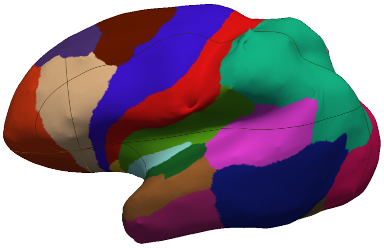
subject-to-adult (FreeSurfer)	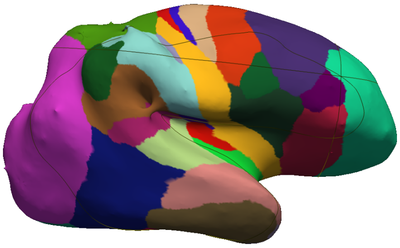	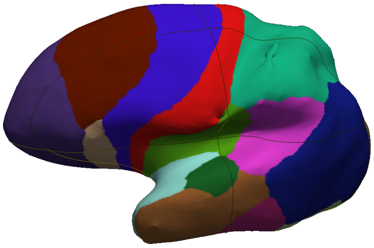

Table 5.3: Automatic parcellation for the worst case subject (subject #3) for the pairwise parcellating scheme presented compared to the 6 year-old's counterpart obtained using the FS standard procedure. Results are presented on the inflated surface. In each case, the first surface corresponds to the right hemisphere and the second one to the left one, respectively. The first row displays the parcellation of the 6 year-old's cortical surfaces. The second and third rows correspond to the parcellation of the same subject at TEA: the second row corresponds to the pairwise (subject-to-subject) scheme and the last row present the results applying the FS standard procedure.

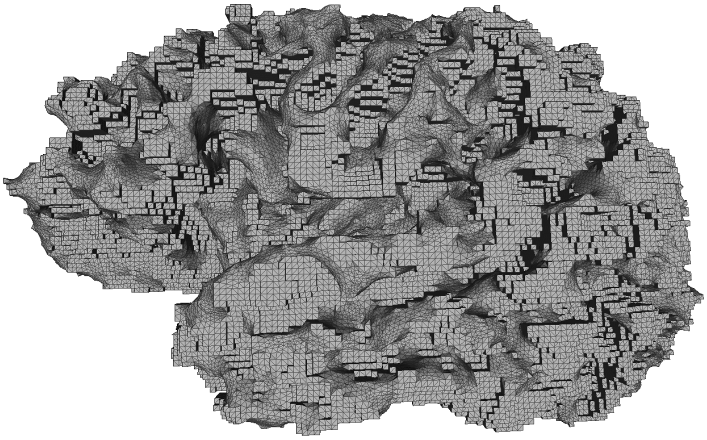

Figure 5.2: Original surface extracted from the segmentation for the left hemisphere of subject #3. The reconstructed surface is highly faceted

Indeed, when comparing the curvature maps for this subjects at the two different time points (TEA and 6 years-old) we can see how, in the first time point, the placement of the Sylvian fissure (SF), among others, is shifted (see Fig. 5.3, left). We observe the same behavior in the temporal region of this hemisphere, with a "displacement" of the lateral cerebral fissure (LCF) and the superior temporal sulcus (STS). Indeed, the LCF merges with the transoccipital sulcus (TOS), hiding the supramarginal (SMG) and angular gyrus (AG). In addition, the paracentral, central and postcentral sulcus (PCS, PC and PoCS, respectively), evident in the central regions of the brain, are also shifted towards the frontal part of the hemisphere. It is for that reason that the cortical delineation of the frontal regions appeared also imprecise, with the frontal pole almost mislaid and the pars orbitalis and pars triangularis regions being bigger than expected. On top of that, the reconstructed surface shows an unnatural distortion, mainly in the superior parietal region (highlighted with a light blue rectangle).

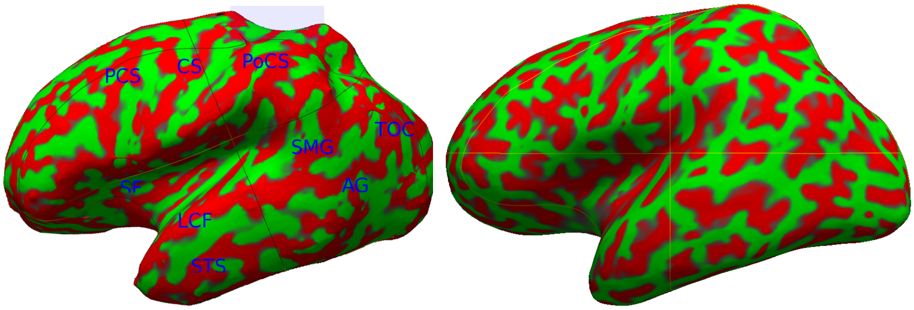

Figure 5.3: The mean curvature pattern for the inflated surface of subject #3 at TEA (left) and at 6 year-old (right). The per-vertex variable "convexity" of the inflated surface (*aka* 'sulc') is plotted in red color. On the newborn surface (left) some sulci are named in blue: SF stands for sylvian fissure; LCF, lateral cerebral fissure; STS, superior temporal sulcus; TOS, transoccipital sulcus; PCS, paracentral sulcus; CS, central sulcus, PoCS, postcentral sulcus; SMG, supramarginal gyrus and AG, angular gyrus. The distortion of the surface in the superior parietal region is highlighted with a light blue rectangle.

The effect of the misleading curvature information which shifts the limit of the cortical regions, together with the slight distortion of the surface, resulted in a less accurate registration and, as expected, in a mismatch in the cortical delineation. This fact is not surprising, as the surface-based non rigid registration employed for the registration task specifically uses the sulcal landmark to match both surfaces. Thus, if the sulci are not accurately placed, the resulting regions will be unavoidably misplaced.

Whereas subjects 1, 3 and 4 provided similar results, the parcellation scheme failed when processing subject #2. Again, the reason for the mismatch is due to the segmentation errors. In the surfaces obtained for this subject, we clearly observe how part of the brain stem is included as white matter (see Fig. 5.4). Here, even though the reconstruction procedure gave us the surface without artefacts and singularities, the surface matching is hard to obtain. Unavoidably, the registration task fails in this case.

Figure 5.4: Medial view of the white surface of the right hemisphere of subject #2. Due to segmentation errors, the brain stem is included as white matter.

5.4 Discussion and Conclusions

In this chapter we have exploited the surface correspondences of a longitudinal dataset to provide anatomically coherent cortical surfaces delineations for newborn subjects. The parcellation scheme presented here is fully automatic, with no manual interaction needed.

Premature subjects under study were scanned at several time points. The first images were acquired a few days after premature birth. Subjects were then re-scanned at TEA and at 6 years-old of age. As at TEA the sulcation pattern is the same as the one present in childhood, we hypothesized that the cortical surfaces extracted from these two time points will only differ in a factor of scaling. This equivalence allowed us to register the two surfaces using the curvature information, directly estimated from the underlying surface tesselation.

The results presented here demonstrate how a topologically and geometrically accurate extraction of the cortical surfaces makes it feasible to use of state-of-the art methods for cortical surface parcellation even at the newborn period. One additional condition needs to be full-filed, though. For the registration to work, the target image needs to be close to the original image, in shape and specially in curvature. Indeed, as we can see from our results, FS registration method works provided that the two spherical surface to register presents comparable average sulcal patterns.

In Fig. 5.5, we show the sulcal patterns of the left cortical surface of (a) subject # 1 at TEA and (b) the same subject a 6 years-old.

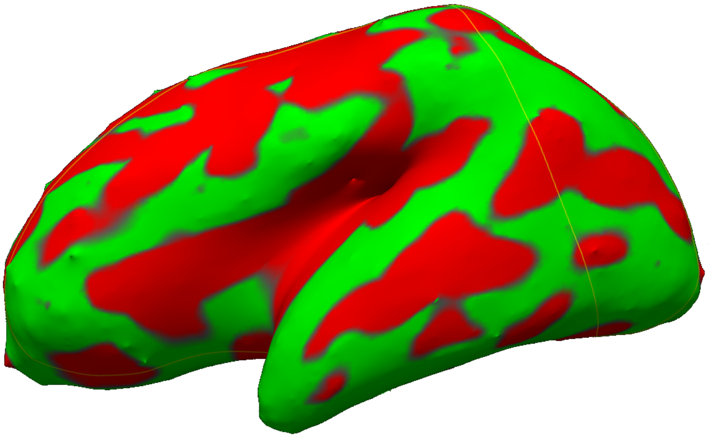

(a) Sulcal profile of the inflated surface of the left hemisphere of subject # 1 at TEA.

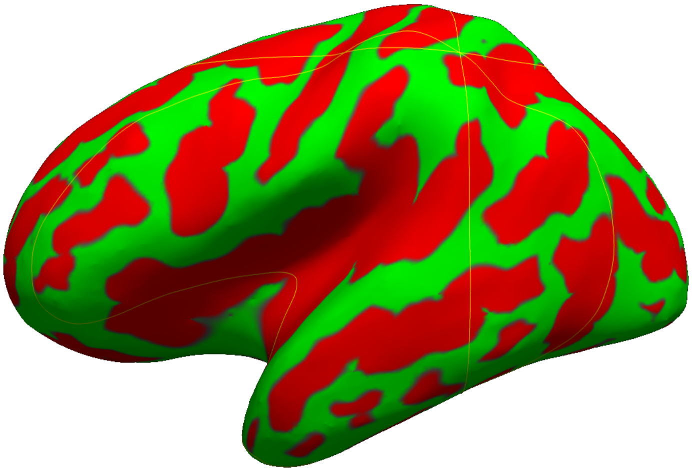

(b) Sulcal profile of the same surface at 6 years-old.

Figure 5.5: Sulcal profiles for the same subject's surfaces a two different time point: (a) TP1, TEA and (b) TP2, 6 years-old.

If we compare these two profiles to the profile from the sample subject provided by FreeSurfer

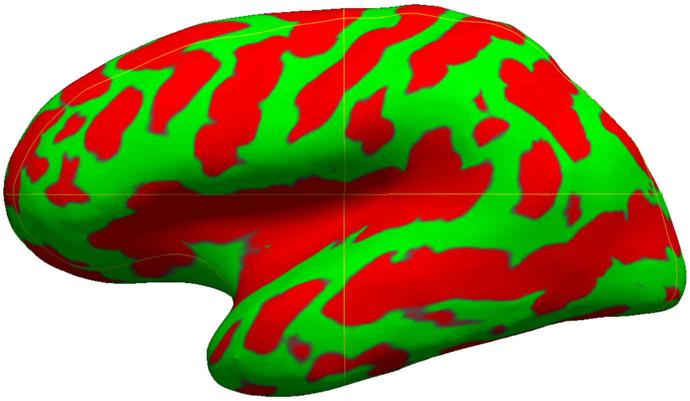

Figure 5.6: Sulcal profile of the Freesurfer's a sample subject, "bert".

(Fig. 5.6), we can see how the averaged sulcal pattern differs from the one obtained over "adult data". Indeed, while at 6 years-old this pattern is equivalent to the "adult" average, at TEA part of the sulcal profile is missing. Yet, what is clear is that the main "sulcal roots" are already present at TEA. This is due to the fact that FS registration minimizes the squared difference between the average convexity, enhancing those highly consistent folding patterns. Surely, comparing the newborn and 6 year-old surfaces, we still see some inaccuracies, mainly in the frontal and occipital lobes, but having access to a "middle" time-point, in between the newborn and adult surfaces, enabled the registration and posterior parcellation.

Indeed, our results corroborate the fact that when trying to register two different surfaces, having "similar" structures is a key point. As we already said in the overview of this Part II, (and as assessed by (Aljabar *et al.*, 2009)), if we want to achieve a correct registration, the target surface should have similar structures with the to-be-registered image. As the sulcal pattern at 6 year of age looks smoother than for the adult case, the correspondence with the newborn time-point is easier to obtain, which is clearly not the case if the adult time-point is used instead.

Nevertheless, having a "closer" time-point is not enough. As we have seen through the second part of this dissertation, to assure a consistent correspondence, the surfaces to be registered need to be both topologically and geometrically consistent. The presence of inconsistencies and singularities in the reconstructed surface undoubtedly impedes the use of any post-processing algorithms, preventing, in our case, the cortical parcellation of the newborn structures. Indeed, the results presented in this chapter strongly rely on the segmentation procedure used to obtain the GM-WM interface. While the automatic surface reconstruction and repair approach presented in the previous chapter (Chapter 4) clearly handles surface singularities (generally due to tissue outliers) and is even able to restore highly faceted surfaces (see Fig.5.2), it cannot cope with major segmentation errors, such as, for instance, the inclusion of the brain stem (again, see Fig. 5.4).

In conclusion, in the last two chapters of this thesis dissertation we have presented a fully automated pipeline that, starting from a set of segmentation labels, restores and reconstructs a topologically and geometrically correct surface. Thanks to this procedure, and after the inflation of the resulting surfaces to an unitary sphere, we are able to register and parcellate the newborn surfaces. This last step was done using an older time-point scan of the same subject. Indeed, this middle point acquisition, which was acquired in early childhood, enables to obtain a surface matching between acquisitions.

We acknowledge that this automatic procedure needs further validation, as for the moment it has been tested only in 4 subjects and the results are preliminary. Yet, we believe that this automated procedure can clearly be the starting point to allow the delineation of newborn cortical structures, and thus, the newborn connectome analysis.

Part III

Discussion and Conclusions

Discussion and Conclusions

6

This thesis arises from a tight interaction between magnetic resonance neuroimaging techniques, graph analysis mathematical methods and medical science. Together with the new advances in the computer vision field, this collaborative effort intends to elucidate fundamental clinical and biological questions in brain development, and set the technical basis that we believe will make feasible to perform connectivity analysis as early as term birth.

The main goal was to study the effects of extreme prematurity and intra uterine growth restriction in school age children, while setting the technical basis to study the brain structural connectivity and the topological and organizational principles of brain networks in early stages of development.

6.1 Summary and contributions

A primary question faced in this work was the investigation of possible brain connectivity alterations characterizing a sensitive population of preterm born children at school age. As we have seen all along this thesis dissertation, extreme prematurity and prenatal growth restriction are, by themselves, major risk factors for long term morbidities, including developmental disabilities such as cerebral palsy, mental retardation and a wide spectrum of learning disabilities and behavior disorders. Brain developmental alterations in structures such as the cerebellum, the hippocampus and white and gray matter volumes have been linked to abnormal behavior and cognition in childhood. Yet, it remains still unclear whether these subtle variations in cognitive and behavioral traits observed during normal development are associated with subtle variations in the structural properties of long-distance connections.

The connectome analysis presented in the first chapter of this thesis, together with the definition of a two-term weighted measure of structural connectivity, allowed to comprehensively study both long-ranging and short-ranging connectivity in preterm school-age children. Our results suggest that EP and IUGR have altered structural connectivity on the cortico-basal ganglia-thalamo-cortical loop connections, whose maturation start early in development. Indeed, we also evidenced alterations of the orbitofrontal cortex circuitry (responsible for reward learning, reality check, and socio-emotional processing). Interestingly, specific short associational cortico-cortical connections, which develop later and are most likely influenced by environmental sensory inputs, showed both diminished and increased strength of connectivity between areas known to play an important role in language, problem solving, and social behavior. More importantly, the strength of these altered connections was associated with children's socio-cognitive performance at school age, providing a link between early life events (extreme prematurity and IUGR), circuitry development, and specific socio-cognitive disabilities.

In order to complement the results obtained in Chapter 2, in Chapter 3 we have characterized the network structure and function by measuring changes related to the refinement in specific metrics of networks topology. As seen in Chapter 2, EP and IUGR affects structural connectivity mainly in the sub-networks related to high cognitive skills and executive functions. Yet, it is not evident if in such cases preterm's brain reorganizes to overcome some of the structural deficits and if they do, to which extent.

The results presented in Chapter 2 show that, the brain network's topology is actually modified after premature birth and/or IUGR. Again, these results suggest that altered fetal nutrition and/or premature birth has an impact in the macrostructural development of brain connectivity, mainly translating to a reduction in network capacity. Indeed, the overall network measures showed correlation with cognitive and behavioral skills. This fact may explain long-term difficulties in learning and social behavior of these children. It bears noting, though, that the combination of both factors did not lead to a worse outcome than considering the two risk factors independently. Instead, the effects of EP seem to prevail over IUGR.

Nevertheless, what still remains unclear is if structural connectivity alterations are already present, and to which extent, in the earlier stages of brain development. Early impairments of white matter connectivity are likely to be of difficult detection, especially due to the technical challenges faced when constructing the connectome in the newborn period. Yet, their characterization is of central importance for the monitoring of brain development and for the identification of neuroimaging biomarkers for early diagnosis. Especially, since there is increasing evidence that deviations from normal connectome development are linked to some neurodegenerative disorders.

In this context, in the second part of this thesis dissertation we set the technical basis to enable the connectome analysis at normal birth time. First and foremost, we have developed a fully automated pipeline to restore and reconstruct the newborn cortical surface in a non-supervised manner. Albeit the results are still preliminary, we provide evidence that a topologically and geometrically coherent cortical surface extraction makes it feasible to use state-of-the art methods to delineate the newborn cortical structures.

As we have shown in Chapter 4, the presence of surface singularities and other nearly invisible artefacts hinder subsequent operations like surface registration and parcellation. Yet, the access to topologically and geometrically corrected surface is necessary if further processing is foreseen for the resulting meshes. In Chapter 4 we presented an approach to repair triangulated surfaces representing the cerebral cortex, which is completely independent from the underlying segmentation. It needs no information other than the triangle mesh itself. It is a fully automated technique which converts an inconsistent input mesh into an output mesh that is guaranteed to be clean and consistent representing the closed manifold surface of the cerebral cortex of one subject's hemisphere. Although the algorithm is clearly dependent on the goodness of the segmentation labels, it removes all typical mesh artefacts such as degenerate triangles, non-manifold vertex and edges overlapping and intersecting triangles. Notably, nearly invisible artefacts present on the cortical surface are also eliminated, comprising sharp peaks.

The surface restoration presented in Chapter 4 made it feasible the registration and parcellation of the newborn cortical surfaces. Taking advantage of a longitudinal dataset, where the same subject was scanned at three different time-points 6 years apart, in Chapter 5 we have aligned the surfaces obtained in Chapter 4, to their corresponding counterpart at 6 years of age. This spherical non-rigid alignment allowed us to use the cortical labels available at 6 years of age to map them in the newborn surface. The main assumption behind this procedure, was that the localization of the main sulci and gyri is stable across lifespan, as at term equivalent age newborns present the same cortical structure than in adults. Indeed, our hypothesis was that these two surfaces were intrinsically the same, differing only on a certain factor of scaling. More importantly, we expected this "factor of scaling" to be smaller when considering a "middle time-point" in the developmental process. It is certainly true that the gyral pattern at normal birth is the same that adults. And it is also clear that the cortical surface will progressively increase by increasing the sulcal depth. Thus, it is logical to expect that the averaged curvature value of the newborn cortical surface will be closer to the surface extracted at 6 years of age rather than an adult one. Indeed we consider this factor, together with the accurate reconstruction of a clean and consistent surface mesh, as being the two main agents that enable the cortical parcellation of the newborn cortical shown surface in Chapter 5.

To conclude, in the second part of this thesis we have presented a set of anatomically coherent cortical delineations for the newborn surfaces, that we believe will enable the construction of the connectome at the neonatal period.

6.2 Perspectives

Higher risk for long-term behavioral and emotional sequel are clear hallmarks of extreme premature birth and birth after pregnancy conditions leading to intra-uterine growth restriction. As the preterm phase (from 24 to 36 post conceptional weeks) is known to be crucial for the growth of the thalamocortical, projectional and commisural fibers, it seems reasonable to expect that changes in intra- or extra-uterine environment translate in changes in neuronal architecture and organization. Specially since the normal development of the cerebral cortex and the cortical axonal pathways happens in a series of sequential events, specific for each of the developmental phases.

In the first part of this work we have shown how the investigation of brain connectivity provides important insights into brain structure and brain's organizational principles. Indeed, the novel MRI techniques are just starting to define the quantitative and qualitative MRI biomarkers that are related to the cognitive outcome seen as a result of underlying changes in prenatal histogenesis. From this point of view, the perspective of analysing specific brain sub-systems for the characterization of brain connectivity alterations is of particular interest. Actually, rather than localized cortical or white matter insults, the effects of EP and IUGR are characterized by in subtle variation in long-distance connections, whose clear description is still elusive.

On the other hand, "higher-order" cognitive processes that will be fundamental to successful adult independence – such as planning, problem solving, working memory – are not phrenologically localized to a specific brain region. Instead, most consciously effortful cognitive processes are thought to emerge from large-scale network of interactions between multiple regional populations of cells that may be anatomically separated from each other over long distances.

Thus, more broadly, it is tempting to assume that specific cognitive, executive and behavioral functions may be encoded within specific brain subnetworks or, equivalently, functional circuits, interconnected across the brain. Brain systems tend to be organized in modules with a high level of interaction within modules and sparser connectivity between them. This near-decomposability of systems into quasi-independent units has well-known operational advantages. Even though this vision might be too simplistic, the understanding of the relationship between (i) the brain network architecture, (ii) the functional processes taking place on the top of the anatomical substrate, and (iii) the sensorimotor, behavioral or cognitive effects resulting from this interaction, is a fundamental interrogative.

Recent studies have suggested that the resting-state activity can be decomposed into sparse sequences of temporally-localized activation events, building up transient and spatially-distributed synchronization patterns. These transient activations may potentially be associated with internal or external mental stimuli, information processing or cognitive functions. For example, resting-state synchronization patterns between parieto-occipital areas, temporally recurring with increasing frequency over single fMRI scanning sessions, have been associated with state of drowsiness or light sleep. In this direction, the investigation of resting-state dynamics *via* functional MRI may provide interesting insights into the relationship between brain functioning (neural activations and communication of information) on the one side, and mental functions (perception, movement, cognition, etc.) on the other side.

It is now commonly accepted that risk factors as early exposure to extra-utero environment or antenatal adverse conditions such as IUGR affects brain structure. Nevertheless, it will be interesting to know whether the brain, during its development, is able to overcome these abnormalities. To develop a comprehensive connectivity model of a developmental disorder, will entail understanding how the disorganization evident in child or adults brain networks has emerged from abnormal developmental processes over several years prior to clinical diagnosis. In this sense, one of the ultimate goals of developmental cognitive neuroscience is to link the complex behavioral milestones that occur throughout the time period elapsing from birth to early childhood with the equally intricate functional and structural changes of the underlying neural substrate. Unfortunately, the remaining technical limitations and open biological issues related to developmental network studies, makes this study complicated.

Although part of these issues have been addressed in this thesis, the conclusions of the second part of this dissertation have revealed directions of future research that may lead to further enhancements of the proposed method. Thus, yielding an improved characterization of brain architecture and functionality at any age. The first one involves the peak detection part. As we already mentioned, in the approach presented here the peak's neighbouring search imposes the same ring size for all peaks in the mesh. Yet, an interactive search allowing for different ring sizes depending on the initial node seed may yield to a more accurate repaired mesh.

On the other side, we acknowledge that other point cloud reconstructing methods should be tested. Because SSD uses dual marching cubes to construct the mesh, if all peaks are not perfectly removed, a new connected component might appear. Although in our analysis this was not the case, it still may happen. This is due to the fact that SSD reconstruction has no constraints on the topology of the surface for the reconstruction of the resulting point cloud, that is, is an implicit method. Still, we know that the final topology of the surface should be equivalent to a sphere, so an explicit method enforcing this topology constraint may give more consistency to the final reconstruction in terms of topology goodness.

Considering the automated cerebro-cortical delineation, the procedure presented in this thesis undeniably needs further validation, and its performance has to be tested in a higher number of subjects. This is clearly the first step to take, and the comparison with a ground-truth, if available, is a good starting point. A further step can be testing this procedure using other state-of-the-art methods such as Demons spherical registration.

From a more practical point of view, a pre-rigid registration of the spherical feature maps might help improving the pairwise inter-subject agreement between label maps and thus, the outcome of the parcellation. Indeed, we also suggest including better spatial and smoothing priors, e.g., as we know that boundaries between gyral regions willf avorably be located at sulcal cusps (as opposite to gyral ridges).

Going one step further, it would be extremely interesting to adapt this procedure to an earlier time-point. Currently, we are able to delineate the cortical regions at term equivalent age. Yet, the subjects under study were also scanned at birth, thus at earlier gestational ages. Certainly, the assumption taken on the sulcal pattern for the TEA case will not hold. However, we can take advantage of the sulcal roots. As we have been all along this manuscript, these sulcal lines are stable and reliable landmarks. They appear close to the 20th week of gestation and remain stable along development and across subjects. Thus, enforcing the registration procedure to stick only to those landmarks and omit the others should lead to a anatomical meaningful cortical parcellation, even with fewer regions of interest.

The next step to take is, undoubtedly, to perform a whole connectome analysis on the newborn data. This thesis was (implicitly) driven towards this ultimate goal. Indeed, the analysis of structural brain connectivity patterns at birth (or TEA) will enable the quantification of a broad range of brain network characteristics that may be used to assess neurological outcome, including network architecture, connectome brain structure and eventual alterations due to antenatal and postnatal risk factors.

Appendices

Appendix A
Computing the connectivity matrix

A

A.1 Computing connectivity matrix

A.1.1 MRI acquisition

Children underwent MRI examinations on a 3T Semens Trio Tim system (Siemens Medical Solutions, Erlangen, Germany). For each subject, a high resolution T1-weighted image was acquired using a 3D magnetization prepared rapid acquisition gradient echo (MPRAGE) sequence. Following a non-diffusion weighted image, diffusion weighted images (DWI) were acquired using a single-shot, spin-echo planar imaging (SE-EPI) sequence covering 30 diffusion directions with a maximum b-value of 1000 s/mm^2, providing whole brain coverage (see table A.1 for scanning parameters). None of the subjects were sedated during the acquisition.

Sequence	TR/TE (TI) (*ms*)	Resolution (mm^2)	Thickness (*mm*)	FOV (mm^3)
T1-w MPRAGE	2500/2.91(1100)	1.8*x*1.8	2	160*x*256*x*208
SE-EPI	1020/107	1.82*x*1.82	2	230*x*230*x*256

Table A.1: Scanning parameters

A.1.2 Building the connectivity matrix

The extraction of the individual whole brain connectivity density matrices was performed using the CMTK software (freely available at www.cmtk.org (Daducci *et al.*, 2012)) following the procedure developed by P. Hagmann and colleagues (Cammoun *et al.*, 2012; Hagmann *et al.*, 2010a, 2007). In short, for each subject, the T1-MPRAGE image was first registered to the non-diffusion-weighted image ($b = 0$) by an affine registration using the FLIRT package implemented in FSL (www.fmrib.ox.ac.uk/fsl). From there, the processing pipeline was divided into two pathways. The WM-GM interface (cortical surface) and the subcortical structures were extracted from the high-resolution T1-weighted image using FreeSurfer segmentation. This method uses intensity information and refines the segmentation using local geometric information. The cortical surface is smooth, with finite curvature everywhere, resulting in a locally planar, structure where cortical gray matter borders other tissue types such as white matter or CSF. The segmentation procedure employs this information by detecting the plane-of-least-variance and using intensity information in this plane as a basis for classifying regions where intensity information alone is insufficient for accurate tissue classification (Dale *et al.*, 1999). Cortical surfaces were subdivided into 66 anatomical parcels by matching the most important sulci using the atlas-based segmentation implemented in FreeSurfer software (http://surfer.nmr.mgh.harvard.edu/) ((Desikan *et al.*, 2006; Fischl *et al.*, 2004) and added to the 16 sub-cortical regions and the brain stem (summing up to 83 regions of interest). The sub-cortical regions and the brain stem were also provided by the FreeSurfer segmentation. This was done in order to have the regions of interest (ROI) in the same anatomical location within all subjects, such that connectivity could be compared locally. The diffusion tensor elements were constructed using a weighted-least-squared method from the diffusion images. The whole brain tractography was performed using a in-home built streamline algorithm. Although the tractography algorithm was constrained within the WM, the streamlines were forced to invade the GM-WM interface, resulting in millions of virtual fibers (streamlines) spread over the brain.

Connectivity density matrices were constructed as follows: for each pair of ROI i and j, the number of virtual fibers passing through them (with end-points in i and j) was computed and its density value stored in the matrix at cell (i, j). This value was estimated as the ratio of the sum of all virtual streamlines connecting each pair of ROI over their individual length and ROI size. This normalization term acts as a correction term to eliminate the linear bias towards longer fibers introduced by the tractography algorithm. Thus, each cell of index (i, j) can be considered as the connection density (CD) of the bundle connecting the ROI i and j. In order to avoid noisy measures, each value in the matrix was threshold by the mean fractional anisotropy (FA) along the bundle. That is, if the mean FA value along the whole bundle connecting ROI i and j was lower than 0.2, the element of the connectivity matrix (i, j) was set to zero, as the connection was considered to be due to noise. This threshold was set empirically and for the pediatric data it was chosen as being relatively low. Diagonal values of the matrix (that reflect ROI self-connections or closed loops) were also discarded.

A.2 Modelling structural connectivity (SC): ADC-weighted and FA-weighted connectomes

Based on (Hagmann *et al.*, 2010b), the structural connectivity (SC) between regions was modelled as the product of two components: (1) the group-connection density (gCD) and (2) the connection efficacy (CE). The first term (gCD) was considered to capture the relative importance of a given fiber pathway within a group of individuals and computed as the average of all subject connectomes within a group, thus conserving the maximum grid of connection shared by all subjects in the given group. Therefore, one connection was considered if it existed in at least one subject of that group. The connection efficacy was considered to be subject-dependent and computed as the mean FA value of the neural pathways connecting two regions (in the FA-weighted case) and as the inverse of the mean apparent diffusion coefficient (1/ADC) in the ADC analysis. Thus, the structural connectivity for subject m was defined as:

$$SC_n(i,j) = \frac{1}{N_{subj}} \left[\Sigma_{m \in group} CD_m(i,j)\right] \times CE_n(i,j) \tag{A.1}$$

The choice of these scalar indexes was twofold. Following (Hagmann *et al.*, 2010b), the ADC value was chosen as a weight for the connection density in order to model white matter maturation as it has been generally used to probe the microstructural pattern of tissues. On the other hand, the FA index was chosen as it is thought to be the most representative of three-dimensional directional diffusivity. Indeed, it has been suggested that variations on the FA values may well be due to fiber packing and fanning as well as axonal myelination and axonal diameter.

Appendix B
Statistical analysis of connectomes

B.1 Statistical analysis for global and local connectivity

As structural connectivity (SC) refers to the existence of axonal fiber paths that interconnect parts of the brain, brain connectomes can be considered as high-resolution matrices that estimate inter-regional connectivity of the human brain (Fischi-Gómez *et al.*, 2014; Meskaldji *et al.*, 2011, 2013). This compact representation of all axonal connections can be used to analyze any eventual connectivity alteration between groups of individuals in a (i) high-level approach (considering global measures) and in a (ii) more local approach, considering all possible pairwise relations between cortical and subcortical regions.

B.1.1 Global analysis of ADC-weighted and FA-weighted connectomes

From each subject's SC-connectome (in both the ADC-weighted and the FA-weighted case) a single measure representing the (i) whole brain connectivity and the (ii) intrahemispheric and (iii) interhemispheric connectivity was derived. This univariate summary statistic (considered as a function of all axonal connections within and between hemispheres) was compared between individuals using a Mann-Whitney test.

B.1.2 Local analysis of FA-weighted connectomes. Pairwise FAw structural connectivity

Local approaches permit a more in-depth analysis of the inter-regional connectivity. However, even if both ADC and FA weighted analysis were performed, the ADC-analysis appeared to be less sensitive to connectivity differences (compared to the FA case). The ADC value is known for providing information about myelin and axonal diameter changes. However, at a b-value = 1000 s/mm^2, the FA index appeared to be more suitable for detecting connectivity alterations, as it is sensitive in a more configurational level (orderliness, packing density of fibers or fiber dispersion).

Similarly to the global analysis, the cortico-cortical and the subcortico-cortical networks were tested using a Mann-Whitney test. This local analysis involved a large number of single correlations that needed to be corrected for multiple comparisons. In such situations, if no correction is applied, there's a greater risk to find "false-positive" associations emerging by chance alone. In order to overcome this multiplicity issue, a novel two-step methodology that exploits the information of positive dependence of the data to increase the power of testing was used (Meskaldji *et al.*, 2013). In short, the tests were first grouped in meaningful disjoint subsets, in which they were supposed to be positively dependent. These subsets were selected based on a recent study performed by Chen et al. (Chen *et al.*, 2012). In their work, the authors exploit the inherent hierarchical, modular (and predominantly symmetric among hemispheres) genetic structure of the cortical area to define a new cortical parcellation, by grouping the cortical areas that share similar genetic expression patterns. This parcellation system reflects shared genetic influence in regional differentiation in humans, demonstrating a biologically sensible organization of the structure of the human brain (Chen *et al.*, 2012). We have grouped ROI derived from FreeSurfer in 13 subsets resembling Chen's clusters (Chen *et al.*, 2012). In each of these subsets, a first screening of the data was performed using a summary statistic at a predefined threshold α/m (being m the number of subsets considered and $\alpha = 0.05$). This first step was followed by a local investigation of the subsets that appear statistically significant, in such a way that the global family-wise error rate (FWER) was controlled at a significance level α (Meskaldji *et al.*, 2013) for detailed information).

Appendix C
Extreme prematurity and intra-uterine growth restriction

C

C.1 Definitions

Preterm birth is defined as babies born alive before 37 weeks of pregnancy are completed. There are sub-categories of preterm birth, based on gestational age (GA): (i) extremely preterm (GA<28 weeks), very preterm (GA=28 to <32 weeks) and (iii) moderate to late preterm (32 to <37 weeks).

IUGR is the pathologic counterpart of small-for-gestational-age. The latter includes fetuses that are small but have reached their appropriate growth potential. Many babies are simply genetically small and are otherwise normal. Fetal growth is dependent on genetic, placental and maternal factors. The fetus is thought to have an inherent growth potential that, under normal circumstances, yields a healthy newborn of appropriate size. The maternal-placental-fetal units act in harmony to provide the needs of the fetus while supporting the physiologic changes of the mother. Limitation of growth potential in the fetus is analogous to failure to thrive in the infant.

The most widely used definition of IUGR is a fetus whose estimated weight is below the 10th percentile for its gestational age and whose abdominal circumference is below the 2.5th percentile. At term, the cutoff birth weight for IUGR is 2,500 g (5 lb, 8 oz). Growth percentiles for fetal weight versus gestational age are shown in C.1. Approximately 70 percent of fetuses with a birth weight below the 10th percentile for gestational age are constitutionally small; in the remaining 30 percent, the cause of IUGR is pathologic. In this dataset, IUGR is defined as estimated fetal weight below the 10th percentile according to local standards (Figueras & Gardosi, 2010) confirmed at birth and Doppler umbilical artery pulsatility index above 95th percentile and/or cerebroplacental ratio below 5th percentile and/or mean uterine artery pulsatility index above 95th percentile. Pregnancies were dated according to the first-trimester crown-rump length measurements.

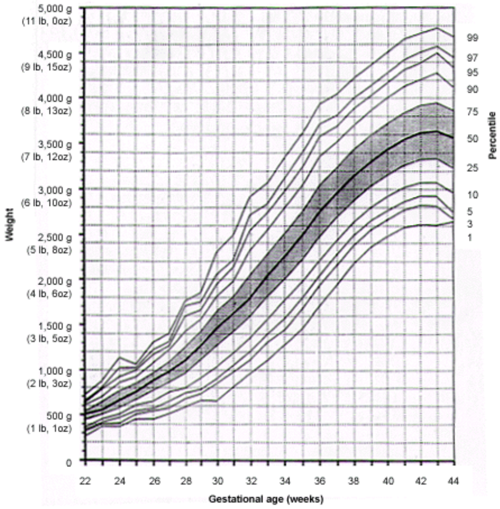

Figure C.1: Fetal weight percentiles throughout gestation.

C.2 Causes, incidence and outcomes of extreme prematurity and IUGR.

C.2.1 Extreme prematurity

Globally, prematurity is the leading cause of death in children under the age of 5. And in almost all countries with reliable data, preterm birth rates are increasing. Inequalities in survival rates around the world are stark. In low-income settings, half of the babies born at 32 weeks (two months early) die due to a lack of feasible, cost-effective care, such as warmth, breastfeeding support, and basic care for infections and breathing difficulties. In high-income countries, almost all of these babies survive.

More than three-quarters of premature babies can be saved with feasible, cost-effective care, e.g., essential care during child birth and in the postnatal period for every mother and baby, antenatal steroid injections (given to pregnant women at risk of preterm labour and meeting set criteria to strengthen the babies lungs), kangaroo mother care (the baby is carried by the mother with skin-to-skin contact and frequent breastfeeding) and antibiotics to treat newborn infections. Common causes of preterm birth include multiple pregnancies, infections and chronic conditions, such as diabetes and high blood pressure; however, often no cause is identified. There is also a genetic influence. Better understanding of the causes and mechanisms will advance the development of solutions to prevent preterm birth.

C.2.2 Intra-uterine growth restriction

Fetal growth restriction is the second leading cause of perinatal morbidity and mortality, followed only by prematurity. The incidence of intrauterine growth restriction (IUGR) is estimated to be approximately 5 percent in the general obstetric population. However, the incidence varies depending on the population under examination (including its geographic location) and the standard growth curves used as reference. In assessing perinatal outcome by weight, infants who weigh less than 2,500 g (5 lb, 8 oz) at term have a perinatal mortality rate that is five to 30 times greater than that of infants whose birth weights are at the 50th percentile. The mortality rate is

70 to 100 times higher in infants who weigh less than 1,500 g (3 lb, 5 oz). Perinatal asphyxia involving multiple organ systems is one of the most significant problems in growth-restricted infants.

Appendix D
Cognitive assessment

At six years of age, the neurodevelopmental outcome of the children in the study was assessed by three different tests: (i) social reasoning abilities were assessed by administering the Social Resolution Task (SRT) (Barisnikov & Hippolyte, 2011); (ii) problematic behavior was assessed by using the French version of the Strength and Difficulties Questionnaire (SDQ) (Goodman, 1997) and (iii) cognitive assessment was carried using the French version of the Kaufman Assessment Battery for children (K-ABC) (Kaufman & Kaufman, 1993).

SRT is designed to test the emotional and socio-cognitive abilities of infants and adults with neurodevelopmental problems. It is an relatively exhaustive battery of tests which relate the social behavior and the processing skills of social and emotional information. SRT assesses the ability to judge, identify, and reason about moral and conventional rules (Barisnikov & Hippolyte, 2011). Only Judgment scores (SRT Q1) and Identification scores (SRT Q2) from SRT were used in analysis, since they were considered appropriate for this age group.

SDQ (Goodman, 1997) is a behavioral screening questionnaire for children aged from 4 to 16 years. It includes 25 items grouped in four dimensions that assess problematic behaviors (conduct problems, hyperactivity/inattention, peer problems and emotional symptoms) and a fifth dimension regarding prosocial behavior. The evaluation consists in a questionnaire completed by the child's parents. We took special attentions into the hyperactivity/inattention index, since preterm children (and especially those who suffered from IUGR) are at risk of these kinds of disorders. In this scale, higher scores are associated with worse outcome.

K-ABC (Kaufman & Kaufman, 1993) evaluates the cognitive abilitiy by means of three scales: (a) sequential processing (SEQ), (b) simultaneous processing (SIM) and (c) achievement scales. Scores from teh SEQ and SIM scales are combined to form a Mental Processing Composite (MCP), which can be interpreted as a measure of intelligence in the K-ABC. Raw scores are transformed into standard scores with mean 100 and standard deviation 15, being considered normal results higher than 85. Family socio-sconomic status (SES) was assessed for each group using the Largo scale (Largo *et al.*, 1989). Exploratory regression analysis (linear regression models) was used to estimate the effect of the GA and IUGR on achieved cognitive scores when adjusting for SES and sex.

Cognitive Assessment Scales	EP (< 28 w GA) n = 23	IUGR (IUGR) n = 21	Control (> 28w GA no IUGR) n = 8
SDQ emotions (> average)	50	70.58	50
SDQ conduct (> average)	45	64.70	37.50
SDQ hyperactivity (> average)	45	52.94	12.50
SDQ peer relationship(> average)	40	47.05	37.50
SDQ prosocial behaviour (< average)	0	17.64	0
K-ABC sequential (< average)	26.08	14.28	0
K-ABC simultaneous (< average)	17.39	9.52	0
K-ABC composite (< average)	21.73	23.80	0
K-ABC knowledge (< average)	30.43	14.28	0

Table D.1: Cognitive sample characteristics of the study participants according to gestational age (GA) and presence of intrauterine growth restriction (IUGR) at 6 years old (data is presented as percentage %). SDQ scores interpretation: Four first scores: when high indicates high substantial risk of clinically significant problems. (a) SDQ prosocial score lower than average indicates high substantial risk of clinically significant problems. (b) K-ABC test, Kaufmann models: help to identify an individuals strengths and weaknesses in cognitive ability and mental processing. Average value set at 85.

Cognitive Assessment Scales	GA mean(stdev) / p-value	BW mean(stdev) / p-value
SDQ emotions (> average)	-0.06(0.13) / p=0.6271	0.1(0.81) / p=0.9068
SDQ conduct (> average)	-0.05(0.09) / p=0.5768	-0.56(0.57) / p=0.3346
SDQ hyperactivity (> average)	-0.14(0.14) / p=0.3254	-1.73(0.89) / p=0.0602
SDQ peer relationship(> average)	-0.01(0.08) / p=0.9166	-0.04(0.48) / p=0.9323
SDQ prosocial behaviour (< average)	-0.08(0.09) / p=0.3867	1.3(0.56) / p=0.0255 (*)
K-ABC sequential (< average)	0.6(0.75) / p=0.4237	0.47(4.91) / p=0.9234
K-ABC simultaneous (< average)	1.54(0.5) / p=0.00391 (*)	7.25(3.31) / p=0.0341 (*)
K-ABC composite (< average)	1.18(0.61) / p=0.0614	4.65(4.04) / p=0.256
K-ABC knowledge (< average)	1.45(1.12) / p=0.2017	4.79(7.35) / p=0.5184

Table D.2: Linear regression model testing the effects of gestational age (GA) and intra uterine growth restriction (IUGR) on children's performance in cognitive workload tasks. *SDQ*: Strengths and Difficulties Questionnaires. *KABC:* Kaufman Assessment Battery for Children. All tests are controlled for sex and family SES and for GA and BW resp.

Appendix E
Modularity and consensus clustering

E

E.1 Estimation and comparison of clustering structures

E.1.1 Algorithms for community detection

Community detection algorithms have gained increasing interest in different domains of applied science, from social networks to biological systems. Since it has become clearer that complex systems share non-random topological properties, a variety of approaches such as divisive or agglomerative algorithms, optimization strategies or methods based on graph dynamical processes have been proposed to disentangle network communities structures (Fortunato, 2010; Newman, 2010). It is out of the scope of this thesis to provide here an extensive review of community detection algorithms. Instead, we will focus on approaches that have been typically used in brain network analysis, with particular attention to the multi-scale and hierarchical nature of the brain network organization.

Let's consider a network module as a set of nodes highly interconnected between them, but sparsely connected with the rest of the network. In such scenario, the modularity quantity Q is a popular and effective measure of network decomposability and quality of the partitions. Modularity was originally defined by (Newman & Girvan, 2004) as the number of edges connecting nodes belonging to the same community, minus the expected value of interconnecting edges in absence of any community structure, i.e. in an equivalent random graph. Formally, Q can we expressed as (Newman, 2006):

$$Q = \frac{1}{2m} \sum_{ij} (A_{ij} - P_{ij}) \delta(C_i, C_j) \tag{E.1}$$

with A the binary or weighted adjacency matrix of network G (A_{ij} being an element of the A), m the total number of edges in the graph, and the δ function expressing the co-occurrence of two nodes (i, j) in the same cluster, i.e.,

$$P_{ij} = \frac{k_i k_j}{2m} \delta(C_i, C_j) = 1 iff C_i \equiv C_j \tag{E.2}$$

P_{ij} expresses the expected number of edges between nodes i and j in an equivalent random network [1]. This probability of connection between two nodes is proportional to the product of their

---

[1] A random equivalent network is a random network equal to our non random graph G in degree sequence.

degree k:

Thus, the modularity can be written as:

$$Q = \frac{1}{2m} \sum_{ij} (A_{ij} - \frac{k_i k_j}{2m}) \delta(C_i, C_j) \tag{E.3}$$

The modularity has been used to compare the quality of different graph partitioning algorithms, or as an objective function by itself. However, the modularity optimization is a computationally hard problem, and different strategies have been proposed such as greedy techniques or simulated annealing. Here we review a greedy approach to the modularity optimization problem proposed by (Blondel *et al.*, 2008) and known as Louvain algorithm. The Louvain algorithm has been often used for brain community detection (Meunier *et al.*, 2009; Rubinov & Sporns, 2011a), and is included in brain graph analysis toolboxes (Rubinov & Sporns, 2010b). Besides its computation efficiency, the Louvain algorithm does incorporate a notion of modular hierarchical structure that is well suited to brain analysis questions. The algorithm is composed of two steps which are iteratively repeated until convergence to a modularity maximum. First, each node is placed in a separate module, and all possible node moves between modules are evaluated in terms of modularity gain (step 1). When no individual move can further improve the Q value, nodes belonging to the same community are agglomerated (step 2) in order to form new 'super-nodes'. Step one (moves evaluation) is repeated on the new "super-nodes" network. The two steps are repeated until convergence. The procedure is sketched in Fig. E.1.

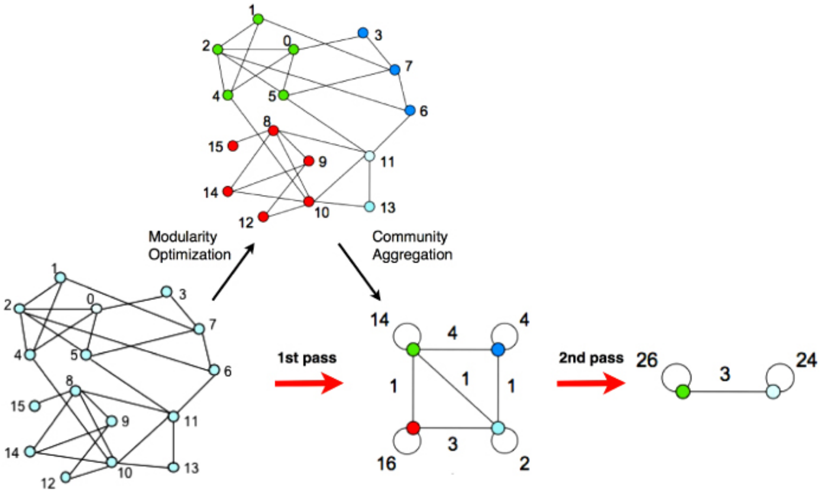

Figure E.1: Schematic representation of Louvain algorithm procedure. First, all possible nodal moves between communities are performed if increasing the modularity Q. Second, nodes belonging the the same community are agglomerated into new "super-nodes": edges between the community nodes and the rest of the network are summed-up, while intra-community edges are transformed into self-loops. The two-steps procedure is repeated iteratively until convergence. From (Blondel *et al.*, 2008).

As mentioned above, brain topology can be modelled as a hierarchical modular network. In fact, hierarchical scales span various orders of magnitude, from nervous column level, to long distance communication (Leergaard *et al.*, 2012). At the macroscopic scale, the brain network is composed of brain regions linked in segregated functional circuits, connected in order to form integrated large-scale subsystems corresponding to higher level functions (Sporns, 2013). It is therefore of interest to uncover multi-scale relationships between brain network elements. Even though the Louvain algorithm can provide a hierarchical partition of the brain network, it does not explicitly address multi-scale aspects of the brain network modular architecture. Different hierarchical and multi-scale graph partitioning have been proposed (Fortunato, 2010). We mention here the works by (Betzel *et al.*, 2013; Lambiotte, 2010; Schaub *et al.*, 2012). The approach described by (Betzel *et al.*, 2013; Lambiotte, 2010; Schaub *et al.*, 2012) is a multi-resolution technique delivering modules at different scales according to a tunable parameter t. Instead of optimizing the classic modularity function, the following quantity is optimized

$$Q'(\mathcal{P}, t) = \frac{1}{2m} \sum_{ij} \left(A'_{ij} - \frac{k_i k_k}{2m} \right) \delta(C_i, C_j) \tag{E.4}$$

with A'_{ij}, the flow graph adjacency matrix, with elements

$$A'_{ij} = (e^{-tL}_{ij} k_j) \tag{E.5}$$

where L is the normalized graph Laplacian matrix. The flow graph A' expresses the probability that a random walker will cross a given edge (i, j) at time t of a continuous-time random walk. The intuition underlying this approach is that random walkers on the original graph G will be "trapped" within progressively larger community as the diffusion time t increases. This method has been successfully used to highlight high resolution (small t) and lower resolution (larger t) structural brain network communities consistent with functional synchronization (Betzel *et al.*, 2013).

E.1.2 Information theory metrics for clustering comparison

A large variety of conceptually different and competing methods for community detection in graphs has been proposed in recent years. In order to evaluate the output of different algorithms and to compare the modular structures of different networks, measures quantifying similarities and differences between graph partitions are needed. In this section we review the mutual information *MI* and variation of information *VI* theoretical measures described by (Meilă, 2007).

Let's consider a network G with n nodes, and two clusterings C and C' of G, with K and K' number of non-overlapping modules in C and C' respectively. The mutual information *MI* quantifies how much information is shared by the two (different) partitions (C, C') of network G, and is defined as (Meilă, 2007)

$$MI_{C,C'} = \sum_{k=1}^{K} \sum_{k'=1}^{K'} P(k, k') \log \frac{P(k, k')}{P(k)P(k')} \tag{E.6}$$

The value $P(k)$ represents the probability of assigning a given network node i to the cluster k and is equal to

$$P(k) = \frac{n_k}{n} \tag{E.7}$$

with n_k number of nodes in cluster k. The quantity $P(k, k')$ expresses the probability that a given node i belongs to cluster k in partition C and to cluster k' in partition C', and is formally the joint probability

$$P(k, k') = \frac{n_{k,k'}}{n} \tag{E.8}$$

with $n_{k,k'}$ number of nodes in cluster k for C and in k' for C'.

The mutual information and variation of information measures are based on the concept of entropy. In an information theory framework, the Shannon entropy $H(C)$ of a network with clustering C represents the uncertainty intrinsic to C or, equivalently, its information content:

$$H(C) = -\sum_{k=1}^{K} P(k)logP(k) = -\sum_{k=1}^{K} \frac{n_k}{n} \log \frac{n_k}{n} \tag{E.9}$$

Intuitively, $H(C)$ expresses the uncertainty that a node i is a assigned to a given cluster in C. The conditional entropy of two clusterings is defines as

$$H(C \mid C') = \sum_{k=1}^{K} \sum_{k'=1}^{K'} P(k,k') \log \frac{P(k')}{P(k,k')} = \frac{n_{k,k'}}{n} \log \frac{n_{k'}}{n_{k,k'}} \tag{E.10}$$

The mutual information $MI(C,C')$ is always non-negative and inferior or equal to the entropy of the two clusters ($MI(C,C') \leq min(H(C),H(C'))$).

The variation of information VI is defined as

$$VI(C,C') = H(C) + H(C') - 2MI(C,C') \tag{E.11}$$

and expresses the quantity of information intrinsic to the two partitions, corrected by the information shared by the two partitions (Fig. E.2). Particularly, $VI(C,C') = 0$ *iff* $C \equiv C'$. Moreover the VI is always non-negative, symmetric and respects the triangle inequality, therefore representing a measure of distance in the data clustering space. VI is up-bounded by the logarithm of the number n of nodes ($\log n$) and can be therefore normalized by this value, giving a rescaled value of VI to the range $[0,1]$. This value is known as the "normalized variation of information" ad is formally defined as:

$$VIn(C,C') = VI(C,C')/\log n \tag{E.12}$$

Similarly, the mutual information measure can as well be rescaled to the $[0,1]$ range, giving the "normalized mutual information" index as (Danon *et al.*, 2005):

$$MIn = \frac{2MIn(C,C')}{H(C) + H(C')} \tag{E.13}$$

The consensus clustering is an approach proposed by (Monti *et al.*, 2003) that delivers an agreement partition across multiple runs of a given clustering algorithm. The basic element of the consensus clustering approach is the construction of a consensus matrix M which stores the normalized number of co-occurrence of two elements (i.e. of two nodes) (i, j) in the same cluster, considering the overall set of subject-wise partitions C^i, with $i = 1, ..., n$. The consensus matrix M has dimensions equal to the brain graph adjacency matrix G^i, and entries (denoted consensus indeces $m_{(u,v)}$) are bounded to the range $[0,1]$. A consensus index equal $m_{(u,v)}$ to 0 indicates that the two nodes u, v are never assigned to the same community, while $m_{(u,v)} = 1$ indicates that u, v are assigned to the same community for all the considered subjects. Ideally, a perfectly stable and recurrent partition over the 40 samples would correspond to a consensus matrix exclusively composed by $0s$ and $1s$, as the node affiliation would not change across samples. The consensus indeces can be used as similarity measure in place of the connection density $w_{(u,v)}$, and feed to the Louvain algorithm. In practice, the consensus matrix M obtained from the samples was thresholded at $\tau = 0.3$ (i.e. all the consensus indexes smaller than 0.3 were considered as noise and set to zero), and the Louvain algorithm was run in it $n_{iter} = 100$ times, delivering a new consensus matrix. This iterative procedure was repeated until the final consensus matrix M presented a perfectly binomial distribution of $0s$ and $1s$ values only, delivering the consensus clustering partition C^{cons}.

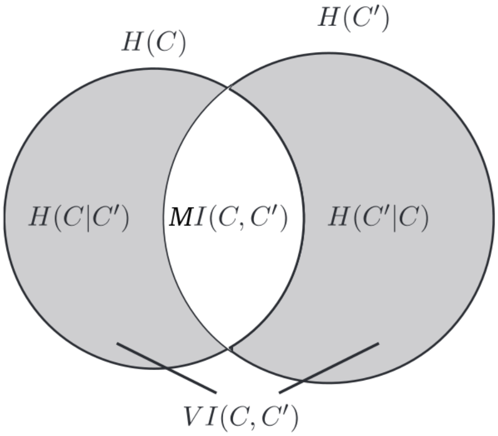

Figure E.2: Logical representation of *MI* and *VI* in function of clusterings entropy and conditional entropy. From (Meilă, 2007).

Bibliography

Acosta O, Fripp J, Dore V, Bourgeat P, Favreau JM, Chetelat G, Rueda A, VIllemagne V, Szoeke C, Ames D, Ellis K, Martins R, Masters C, Rowe C, Bonner E, Gri F, Xiao D, Raniga P, Barra V and Salvado O. (2012). Cortical surface mapping using topology correction partial flattening and 3D shape context-based non-rigid registration for use in qunatifyinf atrophy in Alzheimer's disease.. *Computational Neuroscience*, **205**, 96–109.

Alexander GE, DeLong MR and Strick PL. (1986). Parallel organization of functionally segregated circuits linking basal ganglia and cortex. *Annu Rev Neurosci*, **9(2)**, 357–381.

Alexander-Bloch A, Giedd J and Bullmore E. (2013). Imaging structural co-variance between human brain regions. *Nat Rev Neurosci.*, **14**, 322–336.

Aljabar P, Heckemann R, Hammers A, Hajnal J and Rueckert D. (2009). Multi-atlas based segmentation of brain images: atlas selection and its effect on accuracy. *Neuroimage*, **46(3))**, 726–738.

Anderson PJ. (2004). Executive Functioning in school-aged children who were born very preterm or with extremely low birth weight in the 1990s. *Pediatrics*, **114(1)**, 50–57.

Angenet S, Haker S, Tannenbaum A and R. K. (1999). On the Laplace-Beltrami operator and brain surface flattening. *IEEE Trans. Med. Imag.*, **18(8)**, 700–711.

Aspert N, Santa-Cruz D and Ebrahimi T. (2002). Mesh: measuring errors between distances using the Hausdorff distance. *In. Proc. IEEE International Conference in Multimedia and Expo (ICME)*, **1**, 705–708.

Bach-Cuadra M, Schaer M, Andre A, Guibaud L, Eliez S and Thiran JP. (2009). Brain tissue segmentation of fetal MR images. *MICCAI International Conference on Medical Image Computing and Computer-Assisted Intervention*, **8**, 234–240.

Bai F, Shu N, Yuan Y, Shi Y, Yu H, Wu D, Wang J, Xia M, He Y and Zhang Z. (2012). Topologically convergent and divergent structural connectivity patterns between patients with remitted geriatric depression and amnestic mild cognitive impairment. *The Journal of neuroscience : the official journal of the Society for Neuroscience*, **32**(12), 4307–4318.

Ball G, Boardman JP, Rueckert D, Aljabar P, Arichi T, Merchant N, Gousias I, Edwards AD and Counsell SJ. (2012). The Effect of Preterm Birth on Thalamic and Cortical Development. *Cer.Cortex*, **22**(5).

Ball G, Aljabar P, Zebari S, Tusor N, Arichi T, Merchant N, Robinson EC, Ogundipe E, Rueckert D, Edwards aD and Counsell SJ. (2014). Rich-club organization of the newborn human brain. *Proceedings of the National Academy of Sciences of the United States of America*, **111**(20), 7456–61.

Barisnikov K and Hippolyte L. (2011). Batterie d'évaluation de la cognition sociale et émotionnelle. in: Nader-grosbois n, editor. théorie de l'esprit: Entre cognition, émotion et adaptation sociale chez des personnes typiques et atypiques. *Bruxelles (Belgium): De Boeck*, 135–151.

Barre N and Others . (2011). Language abilities in children who were very preterm and/or very low birth weight: a meta-analysis. *J. Pediatr.*, **158**(5), 774–776.

Baschat A. (2011). Neurodevelopment following fetal growth restriction and its relationship with antepartum parameters of placental dysfunction. *Ultrasound Obstet Gynecol*, **37**, 501–514.

Batalle D, Eixarch E, Figueras F, Muñoz Moreno E, Bargallo N, Illa M, Acosta-Rojas R, Amat-Roldan I and Gratacos E. (2012). Altered small-world topology of structural brain networks in infants with intrauterine growth restriction and its association with later neurodevelopmental outcome. *NeuroImage*, **60**(2), 1352–1366.

Bazin P and Pham D. (2007). Topology-preserving tissue classiication of magnetic resonance brain images. *IEEE Trans. in Med. Imag.*, **26**, 487–496.

Beckmann M, Johansen-Berg H and Rushworth M. (2009). Connectivity-based parcellation of human cingulate cortex and its relation to functional specialization. *Journal of Neuriscience*, **29(4)**, 1175–1190.

Besag J. (1986). On the statistical analysis of dirty pictures (with discussion). *Journal of the Royal Statistical Society*, **45(3)**, 259–302.

Betzel RF, **Griffa** A, Avena-Koenigsberger A, Goñi J, Thiran JP, Hagmann P and Sporns O. (2013). Multi-scale community organization of the human structural connectome and its relationship with resting-state functional connectivity. *Network Science*, **1**(03), 353–373.

Bhutta AT. (2002). Cognitive and behavioural outcomes following very preterm birth. A meta-analysis. *JAMA.*, **288(6)**, 728–736.

Bischoff S, Pavix D and Kobbelt L. (2005). Automatic Restoration of Polygons Models. *ACM Transactions on Graphics*, **24**(4), 1332–1352.

Blondel V, Guillaume JL, Lamiotte R and Lefebvre E. (2008). Fast unfolding of communities in large networks. *J. Statistical Mechanics:Theory and Experiment.*

Bohland J, Bokil H, Ballen C and Mitre P. (2009). The atlas brain concordance problem: quantitative comparison of anatomical parcellation. *PlosOne*, **4(9)**, 1175–1190.

Borradori-Tolsa C, Lodygensky G, Freschi M, Lazeyras F and Hüppi PS. (2005). Hippocampal Development, Post-Natal Growth and Neurodevelopmental Outcome of Premature Newborns Following Iugr: 51. *Pediatric {R}esearch*, **58(2)**, 363.

Bullmore E and Bassett DS. (2011). Brain graphs: graphical models of the human brain connectome. *Annu. Rev. Clin. Psychol.*, **7**, 113–140.

Bullmore E and Sporns O. (2009). Complex brain networks: graph theoretical analysis of structural and functional systems. *Nat. Rev. Neurosci.*, **10(3)**, 186–198.

Cachia A, Mangin JF, Rivière D, Kherif F, Boddaert N, Andrade A, Papadopoulos-Orfanos D, Poline JB, Bloch I, Zilbovicius M, Sonigo P, Brunelle F and Régis J. (2003). A primal sketch of the cortex mean curvature: A morphogenesis based approach to study the variability of the folding patterns. *IEEE Transactions on Medical Imaging*, **22**(6), 754–765.

Calakli F and Taubin G. (2011). SSD: Smooth Signed Distance Surface Reconstruction. *Computer Graphics Forum*, **30**(7).

Cammoun L, Gigandet X, Meskaldji D, Thiran J, Sporns O, Do K, Maeder P, Meuli R and P H. (2012). Mapping the human connectome at multiple scales with diffusion spectrum MRI. *Journal of Neuroscience Methods*, **203**(2), 386–397.

Cavanna A and Trimble M. (2006). The precuneus: a review of its functional anatomy and behavioural correlates. *Brain*, **129**(Pt 3), 564–583.

Chen CH, Gutierrez E, Thompson W, Panizzon M, Jernigan T, Eyler L, Fennema-Notestine C, Jak A, Neale M, Franz C, Lyons M, Grant M, Fischl B, Seidman L, Tsuang M, Kremen W and Dale A. (2012). Hierarchical genetic organization of human cortical surface area. *Science*, **335**, 1634–1636.

Chung MK. (2004). Heat kernel smoothing and its application to cortical manifolds. *Technical Report, No. 1090: University of Winsconsin*.

Cignoni P, Rocchini C and Scopigno r. (1998). Metro: measuring error on simplified surfaces. *Computer Graphics Forum, Blackwell Publishers*, **17(2)**, 167–174.

Cloutman L and Lambon Ralph M. (2012). Connectivity-based structural and functional parcellation of the human cortex using diffusion imaging and tractography. *Frontiers in Neuroanatomy*.

Collin G and van den Heuvel MP. (2013). The ontogeny of the human connectome: development and dynamic changes of brain connectivity across the life span. *The Neuroscientist: : a review journal bringing neurobiology, neurology and psychiatry*, **19(6)**, 616–628.

Collins DL, Le Goualher G and Evans AC. (1998). Non-linear cerebral registration with sulcal constraints. *MICCAI International Conference on Medical Image Computing and Computer-Assisted Intervention*.

Cook P, Bai Y, Nedjati-Gilani S, Seunarine K, Hall M, Parker G and Alexander D. (2006). Camino: open-source diffusion-MRI reconstruction and processing. *Proc. Int. Soc. Mag. Reson. Med. (ISMRM)*, **14**.

Cummings JL. (1993). Frontal-subcortical circuits and human behavior. *Arch Neurol*, **50(8)**, 873–880.

Cummings JL. (1995). Anatomic and behavioral aspects of frontal-subcortical circuits. *Ann N Y Acad Sci*, **769**, 1–13.

Daducci A, Gerhard S, Griffa A, Lemkaddem A, Cammoun L, Gigandet X, Meuli R, Hagmann P and Thiran JP. (2012). The connectome mapper: An open-source processing pipeline to map connectomes with MRI. *PLos One*, **7**(12), e48121.

Dale A, Fischl B and Sereno M. (1999). Cortical surface-based analysis. i. segmentation and surface reconstruction. *NeuroImage.*, **9(2)**, 179–194.

Dale A and Sereno M. (1993). Improved localization of cortical activity b combining eeg and meg with mri cortical surface reconstruction: A linea approach. *J. Cogn. Neurosci.*, **5(2)**, 162–176.

Danon L, Díaz-Guilera A, Duch J and Arenas A. (2005). Comparing community structure identification. *J. Stat. Mech.*, **2005**(9), P09008.

Desbrun M, Meyer M, Schröder P and Barr A. (1999). Implicit fairing of irregular meshes using diffusion and curvature flow. *Proceedings of the 26th annual conference on Computer graphics and interactive techniques.*, 317–324.

Desikan RS, Segonne F, Fischl B, BT BTQ and Dickerson BC. (2006). An automated labelling system for subdividing the human cerebral cortex on MRI scans into gyral based regions of interest. *Neuroimage*, **31**, 968–980.

Destrieux C, Fischl B, Dale A and Halgren E. (2010). Automatic parcellation of human cortical gyri and sulci using standard anatomical nomenclature. *NeuroImage*, **53**(1), 1–15.

Draganski B, Kherif F, Kloppel S, Cook P, Alexander D, Parker G, Deichmann R, Ashburner J and Frackowiak R. (2008). Evidence for segregated and integrative connectivity patterns in the basal ganglia. *J. Neurosci.*, **28**(28), 7143–7152.

Dubois J, Benders M, Cachia a, Lazeyras F, Ha-Vinh Leuchter R, Sizonenko SV, Borradori-Tolsa C, Mangin JF and Hüppi PS. (2008). Mapping the early cortical folding process in the preterm newborn brain. *Cerebral cortex (New York, N.Y. : 1991)*, **18**(6), 1444–54.

Dubois J, Dehaene-Lambertz G, Kulikova S, Poupon C, Hüppi P and Hertz-Pannier L. (2014). The early development of brian white matter : a review of imaging studies in fetuses, newborns and infants. *Neuroscience*, **12**, 48–71.

Duerden E, Carf D, Lax I, Donner E and Taylor M. (2013). Alterations in frontostriatal pathways in children born very preterm. *Dev. Med. Child Neurol.*, **55(10)**, 952–958.

Felleman D and Van Essen D. (1991). Distribute hierarchical processing in the primate cerebral cortex. *Cerebral Cortex*, **1(1)**, 1–47.

Figueras F and Gardosi J. (2010). Intra uterine growth restriction: new concepts in antenatal surveillance, diagnosis, and management. *American Journal of Obstetrics and Gynecology - Review*, 1–13.

Fischi-Gómez E, Vasung L, Meskaldji DE, Lazeyras F, Borradori-Tolsa C, Hagmann P, Barisnikov K, Thiran JP and Hüppi PS. (2014). Structural Brain Connectivity in School-Age Preterm Infants Provides Evidence for Impaired Networks Relevant for Higher Order Cognitive Skills and Social Cognition. *Cerebral cortex.*

Fischl B, Kouwe AVD, Destrieux C, Halgren E, Segonne E and Others . (2004). Automatically parcellating the human cerebral cortex. *Cerebral Cortex*, **14**, 11–22.

Fischl B, Sereno M and AM D. (1999a). High-resolution intersubject averaging and a coordinate system for the cortical surface. *Neuroimage*, **9(2)**, 195–207.

Fischl B, Sereno M, Tootell R and AM D. (1999b). Cortical surface-based analysis: inflation, flattening and surface-based coordinate system. *Human Brain Mapping*, **8**, 272–284.

Fischl B. (2012). FreeSurfer. *NeuroImage*, **62**(2), 774–81.

Florack L, Salden A, Ter Haar Romeny B, Koenderink J and Viergever M. (1995). Nonlinear scale-space. *Image and Vision Computing*, **13**(4), 279–294.

Fortunato S. (2010). Community detection in graphs. *Physics Reports*, **486**(3), 75–174.

Foster-Cohen S, Edgin J, PR C and Woodward L. (2007). Early delayed language development in very preterm infants: evidence from the MacArthur-Bates CDI. *J. Child Lang.*, **34(3)**, 655–675.

Garel C, Chantrel E, Brisse H, Elmaleh M, Luton D, Oury JF, Sebag G and Hassan M. (2001). Fetal cerebral cortex: normal gestational landmarks identified using prenatal MR imaging. *AJNR. American journal of neuroradiology*, **22**(1), 184–189.

Gaser C, Luders E, Thompson P, Lee A, Dutton R, Geaga J, Hayashi K, Bellugi U, Galaburda A, Korenberg J, Mills D, Toga A and Reiss A. (2006). Increased local gyrification mapped in williams syndrome. *NeuroImage*, **33**.

Geman S and Geman D. (1984). Stocastic relaxation, Gibbs distribution and the Bayesian restoration of images. *Journal of Applied Statistics*, **20(6)**, 721–741.

Gimenez M, Junque C, Vendrell P, Narberhaus A, Bargallo N, Botet F and Mercader J. (2006). Abnormal orbitofrontal development due to prematurity. *Neurology*, **67**, 1818–1822.

Goldman-Rakic P and Selemon L. (1990). New Frontiers in basal ganglia research. Introduction. *Trends in Neurosciences*, **13**, 241–244.

Goodman R. (1997). The strengths and difficulties questionnaire: a research note. *J Child Psychol Psychiatry*, **38**, 581–586.

Gozzo Y, Vohr B, Lacadie C, Hampson M and Katz Kea. (2009). The neural systems sustaining face and proper-name processing. *NeuroImage*, **48**, 458–463.

Griffa A, Baumann P, Ferrari C, Do K and Conus Pea. (2015). Characterizing the connectome in schizophrenia with diffusion spectrum imaging. *Human Brain Mapping*, **36(1)**, 354–366.

Griffa A, Baumann P, Thiran JP and Hagmann P. (2013). Structural connectomics in brain diseases. *NeuroImage*, **80**, 515–26.

Griffa A. (2015). *The topology of structural brain connectivity in disease and spatio-temporal connectomics*. PhD thesis, Signal Processing Institute, Ecole Polytechnique Fédérale de Lausanne [EPFL], Lausanne.

Groenewegen H, Voorn P, HW B, Mulder A and AR C. (2009). The basal ganglia IX. *New York (NY): Springer*.

Guellec I, Lapillonne A, Charlaluk ML, Roze JC, Marret S and Others . (2011). Neurologic outcomes at school age in very preterm infants born with severe or mild growth restriction. *Pediatrics*, **127**(4), 883–891.

Gui L, Lisowski R, Faundez T, H PS, Lazeyras F and Kocher M. (2012). Morphology-driven automatic segmentation of MR images of the neonatal brain. *Med. Image Anal.*, (16(8)), 1565–1579.

Hagmann P, Cammoun L, Gigandet X, Gerhard S, Grant P, Wedeen V, Meuli R, Thiran J, Honey C and Sporns O. (2010a). MR connectomics: Principles and challenges. *Journal of Neuro-Science Methods*.

Hagmann P, Cammoun L, Gigandet X, Meuli R, Honey C, Wedeen V and Sporns O. (2008). Mapping the Structural Core of Human Cerebral Cortex. *PLoS Biol*, **6**(7), e159.

Hagmann P, Cammoun L, Gigandet X, Meuli R and Honey C. (2007). Mapping Human Whole-Brain Structural Networks with Diffusion MRI. *PLoS ONE*, **2(7)**.

Hagmann P, Sporns O, Madan N, Pieenar L, Weeden V, Meuli R, Thiran JP and Grant P. (2010b). White matter maturation reshapes structural connectivity in the late developing human brain. *PNAS*, **107(44)**, 19067–19072.

Hagmann P. (2005). *From diffusion MRI to brain connectomics*. PhD thesis, Lausanne: Ecole Polytechnique F{é}d{é}rale de Lausanne.

Hamann P. (1993). Curvature approximation of triangulated surfaces. *Computing*, **8**, 139–153.

Han X, Xu X, Braga-Neto U and Prince J. (2002). Topology correction in brain cortex segmentation using a multiscale, graph-based algorithm. *IEEE Transactions on medical imaging*, **21(2)**, 109–121.

Hebert M, Ikeuchi K and Delingette H. (1995). A spherical representation for recognition of free-form surfaces. *IEEE Transactions on Pattern Analysis and Machine Intelligence*, **17**(7), 681–690.

Huang H, Xue R, Zhang T, Ren T, Richards L, Yarowsky P nd MillerM and Mori S. (2009). Anatomical charaterization of human fetal brain development with diffusion tensor magnetic resonance imaging. *J. Neurosci.*, **29(13)**, 4263–4273.

Huang H, Zhang J, Wakana S, Zhang W, Ren T, Richards LJ, Yarowsky P, Donohue PK, Graham E, van Zijl PCM and Mori S. (2006). White and gray matter development in human fetal, newborn and pediatric brains. *NeuroImage*, **33**(1), 27–38.

Hüppi PS and Dubois J. (2006). Diffusion tensor imaging of brain development. *Seminars in Fetal and Neonatal Medicine*, **11**, 577–656.

Hüppi PS, Maier S, Peled S, Zientara G, Barnes P, Jolesz F and Volpe J. (1998). Microstructural development of human newborn cerebral white matter assessed in vivo by diffusion tensor magnetic resonance imaging. *Pediatr. Res.*, **44 (4)**, 584–590.

Im K, Jo HJ, Mangin JF, Evans AC, Kim SI and Lee JM. (2010). Spatial distribution of deep sulcal landmarks and hemispherical asymmetry on the cortical surface. *Cerebral cortex (New York, N.Y. : 1991)*, **20**(3), 602–11.

Indeer TE and Hüppi PS. (1999). Early detection of periventricular leukomalacia by diffusion-weighted magnetic resonance imaging techniques. *J. Pediatr.*, **134**(5), 631–634.

Inder TE, Warfield SK, Wang H, Hüppi PS and Volpe JJ. (2005). Abnormal Cerebral Structure Is Present at Term in Premature Infants. *Pediatrics*, **115(2)**, 286–294.

Jaekel J an BaumannN and Wolke D. (2013). Effects of gestational age at birth on cognitive performance: A function of cognitive workload demands. *PLoS One*, **8(5)**.

Judas M, Rados M, Jovanov-Milosevic N, Hrabac P, Stern-Padovan R and Kostovic I. (2005). Structural, immunocytochemical, and mr imaging properties of periventricular crossroads of growing cortical pathways in preterm infants. *AJNR American journal of neuroradiology.*, **26** (10), 2671–2684.

Kanold PO and Shatz CJ. (2006). Subplate neurons regulate maturation of cortical inhibition and outcome of ocular dominance plasticity. *Neuron*, **51**(5), 627–638.

Kaufman A and Kaufman N. (1993). K-abc: batterie pour l'examen psychologique de l'enfant. *Paris (FR): Editions du Centre de Psychologie Appliquée*.

Kaufmann A and Kaufmann N. (1983). Kaufmann assessment battery for children. *Minnesota: Circle Pines*.

Kazhdan M, Bolitho M and Hoppe H. (2006). Poisson surface reconstruction. *In Proc. 4th Eurographics Symposium on Geometry Processing*, 61–70.

Kersbergen KJ, Leemans A, Groenendaal F, van der Aa NE, Viergever MA, de Vries LS and Benders MJNL. (2014). Microstructural brain development between 30 and 40week corrected age in a longitudinal cohort of extremely preterm infants. *NeuroImage*, **103**, 214–224.

Keshavan M, DeBellis M, Dick E, Kotwal R, Rosenberg D, Sweeney J, Minshew N and JW P. (2002). Development of the corpus callosum in childhood, adolescence and early adulthood. *Life Sc.*, **70(16)**, 1909–1922.

Kim DJ, Davis EP, Sandman CA, Sporns O, O'Donnell BF, Buss C and Hetrick WP. (2014). Longer gestation is associated with more efficient brain networks in preadolescent children. *NeuroImage*, **100C**, 619–627.

Klein A, Andersson J, Ardekani B, Ashburner J, Avants B, Chiang M, G.E. C, Collins D, Gee J, Hellier P, Song J, Jenkinson M, Lepage C, Rueckert D, Thompson P, Woods R, J.J. M and Parsey R. (2009). Evaluation of 14 nonlinear deformation algorithms applied to human brain MRI registration. *Neuroimage*, **46**(3), 786–802.

Knupp PM. (2001). Algebraic mesh quality metrics. *SIAM J. Sci. Comput.*, **23**, 193–218.

Kobbelt L, Campagna S, Vorsatz J and Seidel HP. (1998). Interactive multiresolution modeling on arbitrary meshes. *Computer Graphics (SIGGRAPH 1998 Proceedings)*, 105–114.

Koenderink JJ and van Doorn AJ. (1992). Surface shape and curvature scales. *Image and Vision Computing*, **10(8)**, 557–564.

Kostovic I and Jovanov-Milosevic N. (2006). The development of cerebral connections during the first 20–45 weeks' gestation. *Semin Fetal Neonatal Med*, **11(6)**, 415–422.

Kostovic I, Jovanov-Milosevic N, Rados M, Sedmak G, Benjak V, Kostovic-Srzentic M, Vasung L an CuljatM, Rados M and Huppi Pea. (2007). Transient patterns of cortical lamination during prenatal life: do they have implications for treatment? *Neurosci Biobehav Rev*, **31(8)**, 1157–1168.

Kostovic I and Rakic P. (1990). Developmental history of the transient subplate zone in the visual and somatosensory cortex of the macaque monkey and human brain. *J. Comp. Neurol.*, **297(3)**, 441–470.

Kwon S, Vasung L, Ment L and Huppi P. (2014). The role of neuroimaging predicting neurodevelopmental outcomes in preterm neonates. *Clin Perinatol*, **41(1)**, 257–283.

Lambiotte R. (2010). Multi-scale modularity in complex networks. In *2010 Proceedings of the 8th International Symposium on Modeling and Optimization in Mobile, Ad Hoc and Wireless Networks (WiOpt)*, 546 –553.

Lancichinetti A and Fortunato S. (2012). Consensus clustering in complex networks. *Sci. Reports*, **2**(36).

Largo R, Pfister D, Molinari L, Kundu S, Lipp A and Due G. (1989). Significance of prenatal, perinatal and postnatal factors in the development of aga preterm infants at five to seven years. *Dev Med Child Neurol*, **31**, 440–456.

Larroque B, Ancel P, Marret S, Marchand L, Andre M, Arnaud C, Pierrat V, Roze J, Messer J and Thiriez Gea. (2008). Neurodevelopmental disabilities an special care of 5-years-old children born before 33 weeks of gestation (the EPIPAGE study): a longitudinal cohort study. *The Lancet*, **371(2)**, 813–820.

Leergaard TB, Hilgetag CC and Sporns O. (2012). Mapping the connectome: Multi-level analysis of brain connectivity. *Front Neuroinform*, **6**.

Lemkaddem A, Daducci A, Kunz N, Lazeyras F and Seeck Mea. (2014). Connectivity and tissue microstructural alterations in right and left temporal lobe epilepsy revealed by diffusion spectrum imaging. *NeuroImage: Clinical*, **5**, 349–358.

Levine T, Grunau R, McAuliffe F, Pinnamaneni R, Foran A and alderdice F. Early childhood neurodevelopment after intrauterine growth restriction: a systematic review, 2015.

Limperopoulos C, Soul JS, Gauvreau K, Hüppi PS, Warfield SK, Bassan H, Robertson RL, Volpe JJ and du Plessis AJ. (2005). Late Gestation Cerebellar Growth Is Rapid and Impeded by Premature Birth. *Pediatrics*, **115**, 688–695.

Lo CY, Wang P, Chou K, Wang J, He Y and CP. L. (2010). Diffusion tensor tractography reveals abnormal topological organization in structural cortical networks in Alzheimer's disease. *J. Neurosci.*, **30**(50).

Lodygensky GA, Seghier ML, Warfield SK, Borradori-Tolsa C, Sizonenko S, Lazeyras F and Hüppi PS. (2008). Intrauterine Growth Restriction Affects the Preterm Infant's Hippocampus. *Pediatric {R}esearch*, **63(4)**, 438–443.

Lorenson W and Cline H. (1987). Marching cubes: a high resolution 3D surface reconstruction algorithm. *Computer Graphics: Proceedings of SISGRAPH*, 163–169.

MacDonald D, Kabani N, Avis D and Evans A. (2000). Automated 3-D Extraction of Inner and Outer Surfaces of Cerebral Cortex from MRI. *NeuroImage*, **12**, 340–356.

Marlow N, Hennessy EM, Bracewell MA and Wolke D. (2007). Motor and Executive Function at 6 Years of Age After Extremely Preterm Birth. *Pediatrics*, **120(4)**, 793–804.

Marston L, Peacock J, Calvert S, Greenough A and Marlow N. (2007). Factors affecting vocabulary acquisition at age 2 in children born between 23 and 28 weeks' gestation. *Dev Med Child Neurol*, **49**(8), 591–596.

Mega MS and Cummings JL. (1994). Frontal-subcortical circuits and neuropsychiatric disorders. *J Neuropsychiatry Clin Neurosci*, **6(4)**, 358–370.

Meilă M. (2007). Comparing clusterings—an information based distance. *Journal of Multivariate Analysis*, **98**(5), 873–895.

Ment LR, Hirtz D and Hüppi PS. (2009). Imaging biomarkers of outcome in the developing preterm brain. *Lancet neurology*, **8**(11), 1042–55.

Meskaldji DE, Ottet MC, Cammoun L, Hagmann P, Meuli R, Eliez S, Thiran JP and Morgenthaler S. (2011). Adaptive Strategy for the Statistical Analysis of Connectomes. *PLOSone*, **6(8)**.

Meskaldji DE, Fischi-Gómez E, Griffa A, Hagmann P, Morgenthaler S and Thiran JP. (2013). Comparing connectomes across subjects and populations at different scales. *NeuroImage*, **80**, 416–25.

Meunier D, Lambiotte R, Fornito A, Ersche KD and Bullmore ET. (2009). Hierarchical modularity in human brain functional networks. *Front Neuroinformatics*, **3**.

Mewes A, Huppi P, Als H, Rybicki F, Inder T, McAnulty G, Milkern R, Robertson R, Rivkin M and Warlfield S. (2006). Regional brain development in serial magnetic resonance imaging of low-risk preterm infants. *Pediatrics*, **118(1)**, 23–33.

Meyer M, Desbrun M, Schroder P and Barr AH. Discrete Differential-Geometry Operators for Triangulated 2-Manifolds, 2002.

Monti S, Tamayo P, Mesirov J and Golub T. (2003). Consensus clustering: A resampling-based method for class discovery and visualization of gene expression microarray data. *J Machine Learning*, **52**(1-2), 91–118.

Narayanan R, Fessler J, Park H and Meyer C. (2005). Diffeomorphic nonlinear transformations: A local parametricapproach for image registration. *Information processing in medical imaging.*, 174–185.

Newman MEJ. (2006). Modularity and community structure in networks. *Proceedings of the National Academy of Sciences of the United States of America*, **103**(23), 8577–82.

Newman MEJ and Girvan M. (2004). Finding and evaluating community structure in networks. *Phys. Rev. E*, **69**(2), 026113.

Newman M. (2010). *Networks: An Introduction.* Oxford University Press. ISBN 9780191500701.

Nishida M, Makris N, Kennedy D, Vangel M, Fischl B, Krishnamoorthy K, Caviness V and PE G. (2009). Detailed semiautomated MRI based morphometry of the neonatal brain: preliminary results. *Neuroimage*, **32(3)**.

Nosarti C, Murray R and Hack M. (2010). Neurodevelopmental outcomes of preterm birth: From childhood to adult life. *Cambridge (GB): Cambridge University Press.*

Ohtake Y, Belyaev A and Bogaevski I. (2000). Polyhedral surface smoothing with simultaneous mesh regularization. *GMP'00: Proceedings of the Geometric Modeling and Processing.*

Ongur D and Price JL. (2000). The organization of networks within the orbital and medial prefrontal cortex of rats, monkeys and humans. *Cerebral Cortex*, **10(3)**, 206–219.

Ou Y and C. D. (2009). DRAMMS: deformable registration via attribute matching and mutual-saliency weighting . *Inf. Process Med. Imaging*, **21**, 50–62.

Padilla N, Falcón C, Sanz-Cortés M an FiguerasF, Bargallo N an CrispiF, Eixarch E, Arranz A, Botet F and Gratacós E. (2011). Differential effects of intrauterine growth restriction on brain strutcure and development in preterm infants: A magnetic resonance study. *Brain Res*, **1382**, 98–108.

Pandit A, Robison E, Aljabar P, Ball G, Gousias I, Wang Z, Hajnal J, Rueckert D, Counsell S, Montana G and Edwards A. (2014). Whole-brain mapping of structural connectivity in infants reveals altered connection strength associated with growth and preterm birth. *Cerebral Cortex*, **24**, 2324–2333.

Pannek K, Scheck SM, Colditz PB, Boyd RN and Rose SE. (2014). Magnetic resonance diffusion tractography of the preterm infant brain: a systematic review. *Developmental medicine and child neurology*, **56**(2), 113–24.

Pantazis D, Joshi A, Jiang J, Shattuck D, Bernstein L, Damasio H and Leahy R. (2010). Comparison of landmark-based an automatic methods for cortical surface registration. *NeuroImage*, **49(3)**.

Parent A and Hazrati LN. (1995). Functional anatomy of the basal ganglia. I. The cortico-basal ganglia-thalamo-cortical loop. *Brain Res Brain Res Rev*, **20(1)**, 91–127.

Pastrawa M, JH G, Lin W and Gerig G. (2005). Automatic segmentation of MR images of the developing newborn brain. *Med. Image Anal.*, **9(5)**, 457–466.

Paus T. (2010). Growth of white matter in the adolescent brain: Myeline or axon? *Brain and cognition*, **72**, 26–35.

Pébay PP and Baker TJ. (2003). Analysis of triangle quality measures. *Mathematics of Computation*, **72**(244), 1817–1840.

Pennec X, Cachier P and Ayache N. (1999). Understanding the "Demon's Algorithm": 3D non-rigid registration by gradient descent. *MICCAI International Conference on Medical Image Computing and Computer-Assisted Intervention*, 597–605.

Perona P and Malik J. Scale-space and edge detection using anisotropic diffusion, 1990.

Petanjek Z and Kostovic I. (2012). Epigenetic regulation of fetal brain development and neurocognitive outcome. *Proc Natl Acad Sci U S A*, **109(28)**, 11062–11063.

Peterson B, Vohr B, Staib L, Cannistraci C, Dolberg A, Schneider K, Katz K, Westerveld M, Sparrow S, AW A, Duncan C, Makuch R, Gore J and Ment L. (2000). Regional brain volumes abnormalities and long-term cognitive outcome in preterm infants. *J. Am. Med. Assoc.*, **284(15)**, 1939–1947.

Pienaar R, Fischl B, Caviness V, Makris N and Grant PE. (2008). A methodology for analyzing curvature in the developing brain from preterm to adult. *International journal of imaging systems and technology*, **18**(1), 42–68.

Pierson CR and Others . (2007). Gray matter injury associated with periventricular leukomalacia in the premature infant. *Acta neuropathologica*, **114**(6), 619–631.

Pletikos M, Sousa A, Sedmak G, Meyer K, Zhu Y, Cheng F, Li M, Kawasawa Y and Sestan N. (2014). Temporal specification and bilaterality of human neocortical topographic gene expression. *Neuron*, **81**, 321–332.

Rakic P. (1988). Specification of cerebral cortical areas. *Science*, **241(4862)**, 170–176.

Rakic P. (1991). Experimental manipulation of cerebral cortical areas in primates. *Philos. Trans. R. Soc. Lond. B. Biol. Sci.*, **331(1261)**, 291–294.

Rakic P, Suner I and Williams RW. (1991). A novel cytoarchitectonic area induced experimentally within the primate visual cortex. *Proc. Natl. Acad Sci. USA*, **88(6)**, 2083–2087.

Ramon-Casas M, Bosch L, Iriondo M and X K. (2012). Word recognition and phonological representation in very low birth weight preterms. *Early Hum Dev*.

Ratnarajah N, Rifkin-Graboi A, Fortier MV, Chong YS, Kwek K, Saw SM, Godfrey KM, Gluckman PD, Meaney MJ and Qiu A. (2013). Structural connectivity asymmetry in the neonatal brain. *NeuroImage*, **75**, 187–94.

Riviere D, Mangin JF, Papadopoulos-Orfanos D, Martinez JM, Frouin V and Regis J. (2002). Automatic recognition of cortical sulci of the human brain using a congregation of neural networks. *Medical Image Analysis*, **6(2)**, 77–92.

Rogelj P and Kovacic S. (2006). Symmetric image registration. *Medical Image Analysis*, **10(3)**, 484–439.

Ronan L, Pienaar R, Williams G, Bullmore E, Crow TJ, Roberts N, Jones PB, Suckling J and Fletcher PC. (2011). Intrinsic Curvature: a Marker of Millimeter-Scale Tangential Cortico-Cortical Connectivity? *International Journal of Neural Systems*, **21**(5), 351–366.

Ross G, Lipper E and PA. A. (1990). Social competence and behavior problems in premature children at school age. *Pediatrics*, **86**, 391–397.

Rubinov M and Sporns O. (2010a). Complex network measures of brain connectivity: uses and interpretations. *Neuroimage*, **52**(3), 1059–1069.

Rubinov M and Sporns O. (2010b). Complex network measures of brain connectivity: uses and interpretations. *Neuroimage*, **52**(3), 1059–1069.

Rubinov M and Sporns O. (2011a). Weight-conserving characterization of complex functional brain networks. *Neuroimage*, **56**, 2068–2079.

Rubinov M and Sporns O. (2011b). Weight-conserving characterization of complex functional brain networks. *NeuroImage*, **56**(4), 2068–79.

Rueckert D, LI S, Hayes C, Hill D, Leach M and Hawkes D. (1999). Nonrigid registration using free-form deformations application to breast mr images. *IEEE Trans. on Medical Imaging*, **18(8)**, 712–721.

Sattler J. (1992). Assessment of children. *3rd Edition, San Diego (CA): Jerome Sattler, Publisher Inc.*

Schall O and Samozino M. (2005). Surface from scattered points. A brief survey of recent developments. *1st Int. Workshop on Semantic Virtual Environments. Faldicieno B., Magnenat-Thalman N,. (Eds), MIRALAB*, **21(5)**, 138–147.

Schaub MT, Delvenne JC, Yaliraki SN and Barahona M. (2012). Markov dynamics as a zooming lens for multiscale community detection: Non clique-like communities and the field-of-view limit. *PLoS ONE*, **7**(2), e32210.

Schmahmann J and Pandya D. (2006). *Fiber pathways of the brain.*

Schnider A. (2008). The confabulating mind. How the brain creates reality. *British Journal of Psychiatry*, **194(1)**.

Ségonne F, Grimson E and Fischl B. (2005). A genetic algorithm for the topology correction of cortical surfaces. *Information processing in medical imaging*, **19**, 393–405.

Smyser CD, Indeer TE, Shimony JS, Hill JE, Degnan AJ, Snyder AZ and Neil JJ. (2010). Longitudinal analysis of neural network development in preterm infants. *Cerebral Cortex*, **20(12)**, 2852–2862.

Sochen N, Kimmel R and Malladi R. A General Framework For Low Level Vision, 1998.

Sporns O, Tononi G and Kötter R. (2005). The human connectome: a structural description of the human brain. *PLoS Computional Biology*, **1(4)**, 245–251.

Sporns O. (2013). Network attributes for segregation and integration in the human brain. *Current opinion in neurobiology*, **23**(2), 162–71.

Stam C, Hillebrand A and VanMieghem P. (2013). Emergence of modular structure in a large-scale brain network with interactions between dynamics and connectivity. *Front. Comput. Nuerosci.*, **4**.

Supekar K and Others . (2010). Development of functional and structural connectivity within the default mode network in young children. *Neuroimage*, **52(1)**, 290–301.

Sur M and Rubenstein JL. (2005). Patterning and plasticity of the cerebral cortex. *Science*, **310(5749)**, 805–810.

Takada M, Tokuno H, Nambu A and Inase M. (1998). Corticostriatal projections from the somatic motor areas of the frontal cortex in the macaque monkey: segregation versus overlap of input zones from the primary motor cortex, the supplementary motor area, and the premotor cortex. *Experimental brain research Experimentelle Hirnforschung Experimentation cerebrale*, **120(1)**, 114–128.

Tao X, Prince J and Davatzikos C. (2002). Using a statistical shape model to extract sulcal curves on the outer cortex of the human brain. *IEEE Trans. on medical imaging*, **21(5)**, 513–524.

Taubin G. (1995a). A signal processing approach to surface fairing. *SIGGRAPH'95 Proceedings*, **18(3)**, 351–358.

Taubin G. (1995b). Curve and surface smoothing without shrinkage. In *iccv95*.

Taubin G. (2000). Geometric Signal Processing on Polygonal Meshes. *Eurographics'2000. STAR: State of the Art Report*.

Thirion JP. (1998). Image matching as a diffusion process: an analogy with maxwell's demons. *Medical image analysis*, **2(3)**.

Thompson P and Toga A. (1996). A surface-based technique for warping 3-dimensional images of the brain. *IEEE Trans. in Med. Imaging*, **15(4)**, 402–417.

Toews M, Wells WM and Zöllei L. (2012). A feature-based developmental model of the infant brain in structural MRI. *MICCAI International Conference on Medical Image Computing and Computer-Assisted Intervention*, **15**(Pt 2), 204–11.

Tolsa CB, Zimine S, Warfield SK, Freschi M, Rossignol AS, Lazeyras F, Hanquinet S, Pfizenmaier M and Hüppi PS. (2004). Early alteration of structural and functional brain development in premature infants born with intrauterine growth restriction. *Pediatric {R}esearch*, **56(1)**, 132–138.

Treyvaud K, Ure A, Doyle L, Lee K, Rogers C, Kidokoro H, Inder T and Anderson P. (2013). Psychiatric outcomes at age seven for very preterm children: rates and predictors. *J Child Psychol Psychiatry*, **54**, 772–779.

Tu Z, Zhen S, Yuille AL an ReissA, Dutton R, Lee A, Galaburda A, Dinov I, Thompson P and Toga A. (2007). Automated extraction of the cortical sulci based on a supervised learning approach. *IEEE Trans. in medical imaging*, **26(4)**, 514–552.

Turner AM and Greenough WT. (1985). Differential rearing effects on rat visual cortex synapses. I. Synaptic and neuronal density and synapses per neuron. *Brain Research*, **329**, 195–203.

Tymofiyeva O, Hess CP, Xu D and Barkovich aJ. (2014). Structural MRI connectome in development: challenges of the changing brain. *The British journal of radiology*, **87**(1039), 20140086.

Tymofiyeva O, Ziv E, Tian N, Sl B, McQuillen P, Ferriero D, Barkhovich A and Duan X. (2012). Towards the "baby connectome": mapping the structural connectivity of the newborn brain. *Plos One*, **7**(**2**).

Tzourio-Mazoyer N, Landeau B, Papathanassiou D, Crivello F, Etard O, Delcroix N and Mazoyer B an JoliotM. (2002). Automated anatomical labeling of activations in SPM using a macroscopic anatomical parcellation of the MNI MRI single-subject brain. *Neuroimage*, **15**(**1**), 273–289.

Vaillant M and Davatzikos C. (1997). Finding parametric representations of the cortical sulci using an active contour model. *Med. Image Analysis*, **1**(**4**), 295–315.

van den Heuvel MP and Sporns O. (2011). Rich-club organization of the human connectome. *The Journal of neuroscience : the official journal of the Society for Neuroscience*, **31**(44), 15775–86.

Van Essen DC. (1997). A tension-based theory of morphogenesis and compact wiring in the central nervous system. *Nature*, **385**, 313–318.

Van Essen DC, Drury HA, Joshi S and Miller MI. (2000). Functional and structural mapping of human cerebral cortex. *Ad. Neurol.*, **84**, 23–34.

Vasung L, Huang H, Jovanov-Milosevic N, Pletikos M, Mori S and Kostovic I. (2010). Development of axonal pathways in the human fetal fronto-limbic brain: histochemical characterization and diffusion tensor imaging. *J. Anat.*, **217**(**4**), 400–417.

Vasung L, Jovanov-Milosevic N, Pletikos M, Mori S, Judas M and Kostovic I. (2011). Prominent periventricular fiber system related to ganglionic eminence and striatum in the human fetal cerebrum. *Brain Struct Funct.*, **215**(3-4), 237–253.

Vercauteren T, Pennek X, Perchant A and Ayache N. (2007). Non-parametric diffeomorphic image registrationw ith the demons algorithm. *MICCAI International Conference on Medical Image Computing and Computer-Assisted Intervention.*, **4792**, 319–326.

Vercauteren T, Pennek X, Perchant A and Ayache N. (2009). Diffeomorphic Demons: Efficient non-parametric image registration. *Neuroimage*, S61–S72.

Vértes PE and Bullmore ET. (2014). Annual Research Review: Growth connectomics - the organization and reorganization of brain networks during normal and abnormal development. *Journal of child psychology and psychiatry, and allied disciplines*.

Volkmar F and Greenough W. (1972). Rearing complexity affects branching of dendrites in the visual cortex of the rat. *Science*, **172**(4042), 1445–1447.

Volpe JJ. (2009). The encephalopathy of prematurity–brain injury and impaired brain development inextricably intertwined. *Semin. Pediatric Neurology*, **16**(4), 167–178.

Wang J and Yu Z. (2011). Quality Mesh Smoothing via Local Surface Fitting and Optimum Projection. *Graphical models*, **73**(4), 127–139.

Wang J, Zhang X and Yu Z. (2012). A cascaded approach for feature-preserving surface mesh denoising. *Computer-Aided Design*, **44**(7), 597–610.

Weisenfeld N and Warfield S. (2009). Segmentation of newborn brain MRI. *Neuroimage*, **32**, 1041–1049.

Welker W. (1990). Why does cerebral cortex fissure and fold? a review of determinants of gyri and sulci . *Comparative Structure and evolution of cerebral cortex*, **(Jones, E.G and Peters, A. ed.)**, 3–136.

Wells III M, Viola P, Atsumi P, Nakajima S and Kikinis R. (1996). Multi-modal volume registration by maximization of mutual information. *Medical Image Analysis*, **1(1)**, 35–51.

Wolke D, Samara M, Bracewell M, Marlow N and Group E. (2008). Specific language difficulties and school achievement in children born at 25 weeks of gestation or less. *J. Pediatr.*, **152**(2), 256–262.

Wood Z, Hoppe H nad DesbrunM and Schroder M. (2004). Removing excess topology from isosurfaces. *ACM Transactions on Graphics*, **23(2)**, 190–208.

Woodward LJ, Anderson P, Austin N, Howard K and Inder T. (2006). Neonatal MRI to predict neurodevelopmental outcomes in preterm infants. *New England Journal of Medicine*, **355**, 685–694.

World Health Organisation WHO. (2012). Born Too Soon: The Global Action Report on Preterm Birth. Technical report.

Xia M, Wang J and He Y. (2013). Brainnet viewer: A network visualization tool for human brain connectomics. *Plos One*, **8(7)**, e68910. doi:10.1371/journal.pone.0068910.

Xue H, Srinivasan L, Jiang S, Rutherford M, Edwards aD, Rueckert D and Hajnal JV. (2007). Automatic segmentation and reconstruction of the cortex from neonatal MRI. *Neuroimage*, **38**, 461–477.

Yanney M and Marlow N. (2004). Paediatric consequences of fetal growth restriction. *Seminars in fetal and neonatal medicine*, **9**(5), 411–8.

Yeo BTT, Sabuncu MR, Vercauteren T, Holt DJ, Amunts K, Zilles K, Golland P and Fischl B. (2010). Learning task-optimal registration cost functions for localizing cytoarchitecture and function in the cerebral cortex. *IEEE transactions on medical imaging*, **29**(7), 1424–41.

Yotter RA, Dahnke R and Gaser C. (2009). Topological corection of brain surface meshes using spherical harmonics. *MICCAI International Conference on Medical Image Computing and Computer-Assisted Intervention*, **Part II, LNCS 5762**, 125–132.

Zacharia A, Ziminea S, Lovblada KO, Warfield S, Thoenyd H, Ozdobab C, Bossie E, Kreisf R, Boeschf C, Schrothb G and Hüppi PS. (2006). Early Assessment of Brain Maturation by MR Imaging Segmentation in Neonates and Premature Infants. *American Journal of Neuroradiology*, **27**, 972–977.

Zhao W, Shuming G and Hongwei L. (2007). A robust hole-filling algorithm for triangular mesh. *Visual Comput.*

Zilles K, Palomero-Gallagher N and Amunts K. (2013). Development of cortical folding during evolution and ontogenesis. *Trends in Neurosci.*, **970**, 1–10.

Zöllei L, Stevens A and Fischl B. (2010). Non-linear Registration of Intra-subject Ex-vivo and In-vivo Brain Acquisitions . *Human Brain Mapping*.

Zosso D, Bresson X and Thiran JP. (2011). Fast Geodesic Active Fields - A Splitting Scheme for Geometric Image Registration.

Curriculum Vitae - Elda Fischi Gómez

Personal Information

Address	Ch. De Tout-Vent, 1023 Crissier (VD), Switzerland
Telephone	+41 76 235 71 96
E-mail	elda.fischi@gmail.com
Date of birth	15 March 1979 in Sabadell, Barcelona, Spain
Nationality	Spanish and Italian

Research Experience

Jul 2010-Jul 2015	***PhD Candidate*** **École polytechnique fédérale de Lausanne (EPFL)** and **Hopitaux Universitaires de Geneve (HUG)** Research focus: diffusion MRI, brain connectivity, graph theory, surface registration surface parcellation, growth connectome, extreme prematurity, prenatal restriction.
Sep 2007-Jul 2010	***Research Associate*** **Signal Procesing Laboratories 5 (LTS5)** - **École polytechnique fédérale de Lausanne (EPFL)** Train users to image processing and analysis techniques; discuss projects strategy; develop personalized image analysis tools; teaching (doctoral schools and master level); management of platform's software.
Jan 2001-Dec 2002	***Research Assistant*** **- Universitat Politècnica de Catalunya (UPC)** Support development for the Applied Math Department.

Supervision and Teaching

Jul 2013 – Aug 2013	**Master project co-supervision** *Student's dissertation:* "On the optimization of the geodesic active fields (GAF) for image registration: application to multi-scale registration of cortical maps on the sphere."
Fall 2014	**Teaching Assistant** Digital Signal Processing course: Bachelor level School of Engineering, Electrical and Electronics Engineering.
Spring 2009 and 2010	**Laboratory teaching assistant** Image Processing II course: Master level School of Engineering, Electrical and Electronics Engineering.
Fall 2008 and 2009	**Laboratory teaching assistant** Image Processing I course: Master level School of Engineering, Electrical and Electronics Engineering.

Education

Sep 2007-Jul 2008	***Master Thesis*** École polytechnique fédérale de Lausanne (EPFL). Visiting master student *Dissertation:* "Inhomogeneity correction in high field magnetic resonance images: Human brain imaging at 7 Tesla".
Jun 2009	***MSc in Telecommunications Engineering*** Universitat Politècnica de Catalunya (UPC)
Jul 2006	***MBC Telecommunications Engineering*** Universitat Politècnica de Catalunya (UPC)

Additional Information

Languages:	Spanish	native speaker
	Italian	native speaker
	English	C1 good oral and written
	French	C1 good oral and written

IT Competence: - Programming languages: Matlab, Python, C, PHP, shell scripting
- OS: Unix, MS Windows, MAC

Personal Information: B driving license
Swiss C permit

Publications

Journal Papers

E. Fischi-Gomez, L. Vasung, D. E. Meskadji, F. Lazeyras, C. Borradori-Tolsa, P. Hagmann, K. Barisnikov, J.-P. Thiran and P. S. Hüppi "Structural Brain Connectivity in School-Age Preterm Infants Provides Evidence for Impaired Networks Relevant for Higher Order Cognitive Skills and Social Cognition.", *Cerebral Cortex*, doi:10.1093/cercor/bhu073, 2015.

D. E. Meskadji, E. Fischi-Gomez, A. Griffa, P. Hagmann, S. Morgenthaler and J.-P. Thiran, "Comparing connectomes across subjects and populations at different scales.", *Neuroimage*, vol. 80, pp. 416–425, 2013.

E. Fischi-Gomez, E. Muñoz-Moreno, A. Griffa, C. Borradori-Tolsa, F. Lazeyras, E. Gratacos, J.-P. Thiran and P.S. Hüppi, "Brain network characterization of high-risk preterm-born school-age children", *Submitted to Neuroimage*.

Reviews

I. Isgum, M J.N.L. Benders, B. Avants, M.J. Cardosa, S. Counsell,et al., "Evaluation of automatic neonatal brain segmentation algorithms: The NeoBrainS12 challenge.", *Medial Imaging Analysis*, 2014.

L. Vasung, E. Fischi-Gomez, and P. S. Hüppi "Multimodal evaluation of the pediatric brain: DTI and its competitors.", *Pedriatric radiology*, vol. 43, pp. 60–68, 2013.

In preparation

E. Muñoz-Moreno, E. Fischi-Gomez, E. Gratacos, J.-P. Thiran and P.S. Hüppi, "Longitudinal analysis of brain network organization and social cognition from infancy to early adolescence associated to IUGR in a moderately preterm cohort", *To be submitted to Human Brain Mapping*.

Conference Abstracts

E. Fischi-Gomez, A. Griffa, E. Muñoz-Moreno, L. Vasung, C. Borradori-Tolsa, F. Lazeyras, J.-P. Thiran and P. S. Hüppi. "Brain network modular fingerprint of premature born children", *23rd International Symposium on Magnetic Resonance in Medicine (ISMRM)*, Toronto, Canada, 2015

E. Muñoz-Moreno, E. Fischi-Gomez, D. Batallé, L. Vasung, M. Reveillon, C. Borradori-Tolsa, E. Eixarch, J.-P. Thiran, E. Gratacos, and P.S. Hüppi, "Brain connectomics and social cognition from infancy to early adolescence: effects of IUGR." *23rd International Symposium on Magnetic Resonance in Medicine (ISMRM)*, Toronto, Canada, 2015.

L. Vasung, E. Fischi-Gomez, D. E. Meskaldji, F. Lazeyras, C. Borradori-Tolsa and P. S. Hüppi. "Brain connections associated with socio-cognitive skills in preterm and low birth weight school age children", *Pediatric Academic Societies and Asian Society for Pediatric Research Joint Meeting*, Vancouver, Canada, 2014

E. Muñoz-Moreno, E. Fischi-Gomez, D. Batallé, L. Vasung, M. Reveillon, C. Borradori-Tolsa, E. Eixarch, J.-P. Thiran, E. Gratacos, and P.S. Hüppi, "Longitudinal analysis of brain network reorganization in preterm IUGR children at 1, 6 and 9 years-old." *22nd International Symposium on Magnetic Resonance in Medicine (ISMRM)*, Milano, Italy, 2014.

E. Fischi-Gomez, E. Muñoz-Moreno, L. Vasung, D. E. Meskaldji, S. Urben, M. Monnier, K. Barisnikov, C. Borradori-Tolsa, F. Lazeyras, J.-P. Thiran and P. S. Hüppi. "Graph network measures of brain connectivity and its relations with cognitive performance in high-risk children" *22nd International Symposium on Magnetic Resonance in Medicine (ISMRM)*, Milano, Italy, 2014.

A. Pauli, J. Schneider, M. Bach Cuadra, A. Griffa, E. Fischi-Gomez, R. Meuli, J.-P. Thiran, A. Truttman and P. Hagmann, "Towards a connectome mapping pipeline for neonates using high-resolution MP2RAGE and DTI", *21st Annual Meeting International Society for Magnetic Resonance in Medicine*, Salt Lake City, UT, USA, 2013

L. Vasung, L. Gui, E. Fischi-Gomez, C. Borradori-Tolsa, F. Lazeyras, J.-P- Thiran and P.S. Hüppi. "Regional changes of cortical thickness and cortical surface in children born prematurely and children born with intrauterine growth restriction at school age." *21st Annual Meeting International Society for Magnetic Resonance in Medicine*, Salt Lake City, UT, USA, 2013

E. Fischi-Gomez, D.E. Meskaldji, L. Vasung, F. Lazeyras, J.-P. Thiran and P.S. Hüppi. "Extreme prematurity and intra uterine growth restriction effects in brain network topology at school age." *21st Annual Meeting International Society for Magnetic Resonance in Medicine*, Salt Lake City, UT, USA, 2013

E. Fischi-Gomez, D. E. Meskaldji, F. Lazeyras, C. Borradori-Tolsa, J.-P. Thiran and P.S. Hüppi. "Human brain connectome in children born preterm". *Pediatric Academic Societies Annual Meeting*, Boston, Massachusetts, USA, 2012.

E. Fischi-Gomez, A. Griffa, A. Daducci, F. Lazeyras, J.-P. Thrian and P. S. Hüppi. "Graph theory to analyze developmental plasticity in connectivity of preterm children". *20st Annual Meeting International Society for Magnetic Resonance in Medicine (ISMRM)*, Melbourne, Australia, 2012.

E. Fischi-Gomez, L. Cammoun, D. E. Meskaldji, P. Hagmann, R. Meuli, F. Lazeyras, J.-P. Thiran and P.S. Hüppi. "Prematurity and prenatal growth restriction differently affects brain connectivity at age 6 years." *16th Annual Meeting of the Organization for Human Brain Mapping,* Barcelona, Spain, 2010.

A mi familia y amigos...
a los que estan, a los que se fueron y a los que vendran